Review

Nanxi Li*, Chong Pei Ho, Shiyang Zhu, Yuan Hsing Fu, Yao Zhu and Lennon Yao Ting Lee

Aluminium nitride integrated photonics: a review

https://doi.org/10.1515/nanoph-2021-0130
Received March 25, 2021; accepted May 26, 2021;
published online June 18, 2021

Abstract: Integrated photonics based on silicon has drawn a lot of interests, since it is able to provide compact solution for functional devices, and its fabrication process is compatible with the mature complementary metal-oxide-semiconductor (CMOS) fabrication technology. In the meanwhile, silicon material itself has a few limitations, including an indirect bandgap of 1.1 eV, transparency wavelength of >1.1 μm, and insignificant second-order nonlinear optical property. Aluminum nitride (AlN), as a CMOS-compatible material, can overcome these limitations. It has a wide bandgap of 6.2 eV, a broad transparency window covering from ultraviolet to mid-infrared, and a significant second-order nonlinear optical effect. Furthermore, it also exhibits piezoelectric and pyroelectric effects, which enable it to be utilized for optomechanical devices and pyroelectric photodetectors, respectively. In this review, the recent research works on integrated AlN photonics in the past decade have been summarized. The related material properties of AlN have been covered. After that, the demonstrated functional devices, including linear optical devices, optomechanical devices, emitters, photodetectors, metasurfaces, and nonlinear optical devices, are presented. Last but not the least, the summary and future outlook for the AlN-based integrated photonics are provided.

Keywords: aluminum nitride; device; integrated photonics; nanophotonics.

***Corresponding author: Nanxi Li,** Institute of Microelectronics, A*STAR (Agency for Science, Technology and Research), 2 Fusionopolis Way, Singapore, 138634, Singapore, E-mail: linx1@ime.a-star.edu.sg. https://orcid.org/0000-0002-0524-0949

Chong Pei Ho, Shiyang Zhu, Yuan Hsing Fu, Yao Zhu and Lennon Yao Ting Lee, Institute of Microelectronics, A*STAR (Agency for Science, Technology and Research), 2 Fusionopolis Way, Singapore, 138634, Singapore. https://orcid.org/0000-0002-7691-0196 (Y.H. Fu)

1 Introduction

Integrated photonics, based on microelectronics fabrication technology, has been developed mainly for communication purpose [1–4]. Recently, it also demonstrates the potential to be applied in many other areas including optical ranging [5–7], bio/chemical sensing [8–12], computing [13–16], and quantum information processing [17–19]. The integrated photonics based on silicon (Si) has attracted a lot of interests due to the following advantages: Firstly, the high index contrast with its oxide material enables high optical mode confinement factor within the waveguide [20–22]. Secondly, its fabrication is compatible with the mature complementary metal–oxide–semiconductor (CMOS) fabrication process currently used in electronics industry. This enables the fabrication of photonics devices in large scale and with low optical propagation loss [23–27]. Thirdly, its electro-optical and thermal-optical effects enable the modulation and tuning of the optical signal propagating through the devices [28–31]. Silicon photonics platform, including Si, silicon dioxide (SiO_2), silicon nitride (Si_3N_4), and germanium (Ge), have been used to demonstrate optical devices such as optical phased array [32–35], nonlinear optical generator [36–39], optical frequency synthesizer [40–42], light source [43–45] and photodetector [46–48]. Further, the photonics devices can be integrated with electronic control circuits [49, 50]. However, Si is known as a relatively small indirect bandgap material, with bandgap reported to be 1.1 eV [51], which limits the working wavelength of Si-based integrated photonics only above around 1.1 μm. Also, Si has centrosymmetric crystal structure, which limits its application for optical devices relying on second-order nonlinear optical effects, such as optical modulator based on Pockels effect, and second harmonic generator.

Among semiconductor materials, aluminum nitride (AlN) has large bandgap of 6.2 eV [52, 53], and wide transparency window covering from ultraviolet (UV) to mid-infrared (MIR). This enables the AlN-based photonics devices to work in UV, visible, near-infrared (NIR) and up to MIR wavelength regime. Its fabrication process is compatible with CMOS fabrication line, which enables the wafer-level fabrication of AlN-based integrated photonics devices with low cost and high reliability. Also, AlN has

second-order nonlinear optical property ($\chi^{(2)}$ = 4.7 pm/V [54]), contributed by its noncentrosymmetric crystal structure. Furthermore, the piezoelectric effect of AlN enables it to be utilized not only for electro-mechanical devices [55–60], but also for optomechanical devices [61–63]. In addition, AlN exhibits the pyroelectric property, which enables it to be utilized for pyroelectric-based photodetector [64–66]. There are comprehensive reviews on AlN for integrated optomechanics and nonlinear optics [67, 68]. In the meanwhile, to the best of our knowledge, the review article for integrated AlN photonics, covering both passive and active devices demonstrated in recent years, is lacking.

In this review, we summarize the most recent research works on AlN-based integrated photonics, including both passive and active devices demonstrated in the past decade. A summary of related AlN material properties is presented in Section 2. The functional devices, including linear and nonlinear photonics devices, optomechanical devices, emitters, photodetectors, and metasurface-based devices, are presented in Section 3. At last, in Section 4, the summary of this review work, together with the future outlooks for AlN-based integrated photonics are presented. The overall content of this review can be illustrated in Figure 1, where the blue, orange, and green colored tags represent the material, physical properties, and functional devices, respectively.

2 Material properties

In this section, the material properties of AlN are covered. These properties are related to the functional devices to be discussed in later Section 3. Table 1 summarizes these properties based on category, including optical, thermal, electrical, and mechanical properties, with values and references provided.

2.1 Optical property

The refractive index of AlN is around 2.1 at 1550 nm [74], which enables enough index contrast with SiO_2 for mode

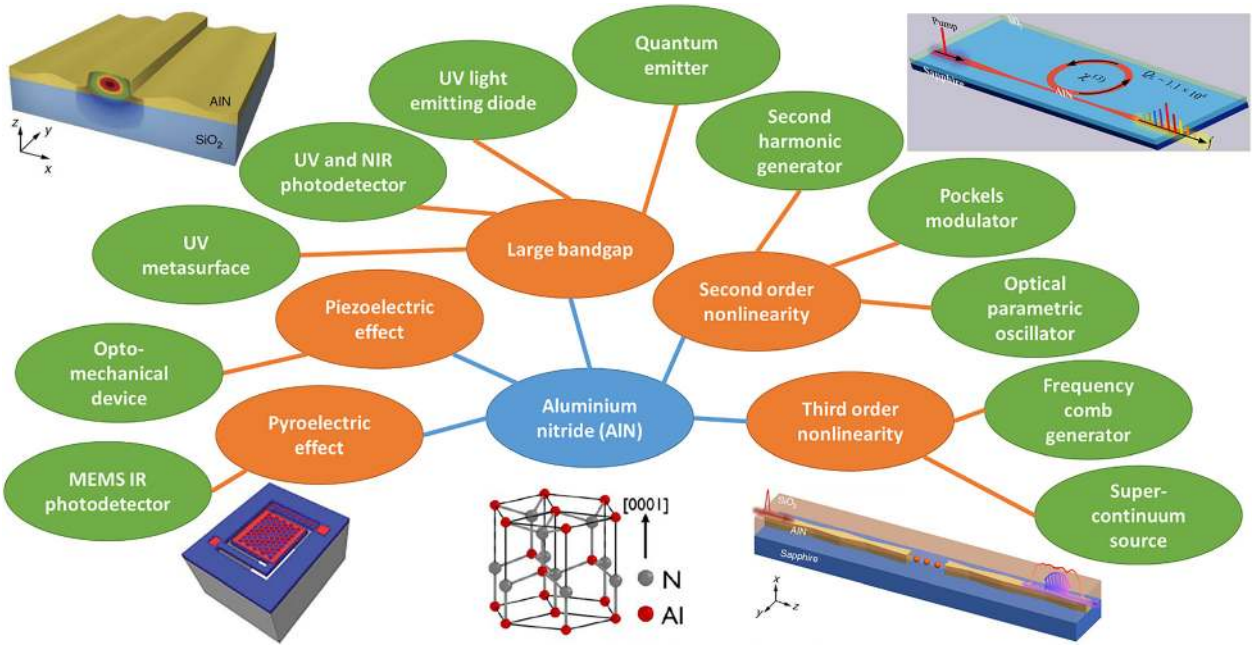

Figure 1: Overview of AlN-based integrated photonics.
Blue, orange and green tags indicate material, key properties, and functional devices, respectively. Inset images: (Top left) Schematic of AlN waveguide illustrating the coupling between the surface acoustic wave (SAW) and optical mode, adapted with permission from Springer Nature, Nature Communications [69]. Suboptical wavelength acoustic wave modulation of integrated photonic resonators at microwave frequencies, S. A. Tadesse, et al. Copyright 2014. (Top right) Schematic of single-crystalline AlN microring on sapphire substrate for Raman-assisted Kerr comb generation, adapted with permission from [70]. Copyright (2018) American Chemical Society. (Bottom left) Schematic of the wavelength-selective pyroelectric sensor, adapted from [71], with the permission of AIP Publishing. (Bottom middle) AlN crystal structure, adapted with permission from [72], https://pubs.acs.org/doi/10.1021/acsphotonics.0c00528, further permissions related to the material excerpted should be directed to the ACS. (Bottom right) Schematic of chirp-modulated taper waveguide, formed by cascading eight linear-tapered segments, adapted with permission from [73]. Licensed under a Creative Commons Attribution.

Table 1: Material property of AlN for integrated photonics.

Property category	Material property	Typical values/Characteristics	Reference/year
Optical	Refractive index	$n = 2.12$ (@1550 nm)	[74]/2019
Optical	Waveguide loss	0.42 dB/cm (@1550 nm)	[75]/2019
Optical	Bandgap	6.2 eV @ room temperature	[52]/1979
Electrical & optical	Nonlinear index	$n_2 = 2.3 \times 10^{-15}$ cm^2/W (@1550 nm)	[74]/2019
Electrical & optical	Electro-optic coefficient	$r_{13} = 0.67$ pm/V, $r_{33} = -0.59$ pm/V (measured using He-Ne laser @ 633 nm)	[76]/1992
Electrical & optical	Second-order nonlinear susceptibility	$\chi^{(2)} = 4.7$ pm/V (pump @ 1550 nm, second harmonic @ 775 nm)	[54]/2012
Electrical & mechanical	Piezoelectric coefficient	$d_{33} = 5.53$ pm/V, $d_{31} = -2.65$ pm/V	[77]/1985
Mechanical	Poisson's ratio	0.287	[78]/2008
Mechanical & optical	Photo-elastic constant	$p_{13} = -0.019$, $p_{33} = -0.107$	[79]/2002
Thermal	Thermal conductivity	$\mathcal{K} = 285$ W/(m·K)	[67]/2012
Thermal & optical	Thermal-optic coefficient	$dn_{AlN}/dT = 4.26 \times 10^{-5}$/K (@1000 nm)	[78]/2008
Thermal & electrical	Pyroelectric coefficient	0.0033 μC/(cm^2·K)	[80]/2014
Thermal & mechanical	Thermal expansion coefficient	4.2×10^{-6}/K (for a axis) 5.3×10^{-6}/K (for c axis)	[78]/2008
Structural	Crystal structure	Wurtzite	[81]/2018
Fabrication	CMOS-compatibility	Yes	[68]/2016

confinement in optical waveguide. After annealing process, the AlN-based photonic waveguide achieves low loss of ~0.4 dB/cm at around 1550 nm [75]. Also, AlN is one of the largest bandgap semiconductor materials, whose bandgap is reported to be 6.2 eV at room temperature [52]. The wide transparency window of AlN, covering from UV, visible, and up to MIR [74, 82, 83], makes AlN an attractive material for photonics integrated circuits. Integrated photonics functional devices working in UV and MIR have been demonstrated. For UV wavelength regime, these devices include microring resonator [84], emitter [85–87], and metasurface [88]. For MIR wavelength regime, the devices include waveguide and beam splitter (as reported in the study by Lin et al. [89]), directional coupler, interferometer, and microring resonator (as reported in the study by Dong et al. [90]). More details of these functional devices will be discussed later in Section 3.

Furthermore, compared with other CMOS-compatible materials, e.g. Si, Si_3N_4, and SiO_2, AlN exhibits both second-order $\chi^{(2)}$ and third-order $\chi^{(3)}$ optical nonlinearities. Its second-order nonlinear optical property is due to the noncentrosymmetric crystal structure. The Pockels effect of AlN, with electro-optic coefficient of $r_{13} = 0.67$ pm/V, $r_{33} = -0.59$ pm/V (measured at 633 nm) [76], enables the demonstration of phase shifter and optical modulator [75, 91, 92]. The significant second-order nonlinear susceptibility (e.g. $\chi^{(2)} = 4.7$ pm/V, obtained with pump at 1550 nm, and second harmonic at 775 nm [54]) enables second harmonic generation (SHG) [54, 93–96], sum/difference frequency generation (SFG, DFG) [68, 97] and parametric down-conversion [98]. The coexistence of second- and third-order nonlinearity (nonlinear index reported to be $n_2 = 2.3 \times 10^{-15}$ cm^2/W at 1550 nm [74]) together with the wide optical transparency window of AlN enable the cascading of different nonlinear effects including SHG, third harmonic generation (THG) and four wave mixing (FWM) [99]. Also, for nonlinear process at telecom wavelength, AlN is free of two photon absorption and related free carrier refraction, while it happens in Si. In addition, the Raman effect of AlN has also been utilized to extend the optical frequency comb wavelength spanning [70, 100], and to demonstrate the Raman-based laser [101].

2.2 Piezoelectric property

The crystal structure of AlN is wurtzite [81], with schematic shown in Figure 1 inset (bottom middle). The structure is noncentrosymmetric, which contributes to the properties of piezoelectricity and pyroelectricity. The piezoelectric coefficient of AlN thin film has been reported to be $d_{33} = 5.53$ pm/V, $d_{31} = -2.65$ pm/V [77, 102]. Such piezoelectric property enables the wide utilization of AlN in microelectromechanical systems (MEMS) [55–57]. The piezoelectric property together with optical properties and CMOS-compatibility of AlN discussed earlier, make AlN a suitable material for optomechanical devices. A number of MEMS-based optomechanical devices have been demonstrated [62, 69, 103, 104]. Also, contributed by the

piezoelectric property [77, 102] and photo-elastic constant (p_{13} = −0.019, p_{33} = −0.107 [79, 105]), AlN has become a platform to investigate the photon–phonon interaction within solids [106, 107]. In addition, by doping with Scandium (Sc), the noncentrosymmetry of the crystal structure can be increased, and hence enables larger piezoelectric coefficient [108, 109]. More details about Sc-doped AlN will be discussed in later Summary and outlook section.

2.3 Thermal property

Compared with other semiconductor materials (e.g. Si, $\mathcal{K}$ = 145 W/(m·K) [110]), AlN has significantly higher thermal conductivity ($\mathcal{K}$ = 285 W/(m·K) [67]). Also, AlN has small thermo-optic coefficient ($dn_{\mathrm{AlN}}/dT = 4.26 \times 10^{-5}$/K at 1000 nm [78]). These thermal properties make AlN-based devices able to handle high optical power since it is more tolerable to temperature fluctuations. One example for such functional device is metasurface [88], which could be utilized to handle high optical power. Furthermore, as mentioned earlier, AlN exhibits pyroelectric property due to its noncentrosymmetric crystal structure, with pyroelectric coefficient reported to be 0.0033 μC/(cm^2·K) [80]. Therefore, AlN can be utilized as pyroelectric photodetector, as reported in [64, 65, 71, 111, 112]. Also, ScAlN has been demonstrated to improve the performance of AlN-based pyroelectric photodetector [66]. The enhanced pyroelectric coefficient of ScAlN is also attributed to the increase of noncentrosymmetry of the crystal structure.

3 Functional devices

Contributed by the piezoelectric [102] and photo-elastic properties [79] of AlN, AlN-based integrated photonics devices have drawn a lot of interests in research, to enable multi-functions for integrated photonics and optomechanics. Although, in earlier time, AlN has been widely used for sensors, actuators [55, 56, 113], and also demonstrated for UV LEDs [114], to the best of our knowledge, there is very limited investigation for AlN-based integrated photonics before the year of 2012. In this section, the AlN-based functional devices demonstrated in the past decade have been summarized and presented. It covers linear optical devices (coupler, waveguide, resonator, etc.), optomechanical devices, emitters, photodetectors, metasurface, and nonlinear optical devices. The linear optical devices and optomechanical devices are summarized in Table 2. Emitters, photodetectors and metasurfaces are summarized in Table 3. χ(2) and χ(3) nonlinear optical devices are summarized in Table 4 and Table 5, respectively.

As mentioned in the earlier Optical property section, one of the key advantages of AlN-based photonics platform is the large bandgap, which enables the functional devices to work in UV and visible wavelength range. Such key advantage enables AlN-based photonics platform to overcome the challenges of current Si-based photonics integrated circuits. The photonics integrated functional devices working in UV and visible spectrum can find applications in various areas, including integrated spectrometers for biochemical sensing, UV Raman spectroscopy, beam steering by optical phased array, and visible light communication [53]. Also, since many atomic transitions are in UV and visible wavelength regime, such as Ytterbium ions (369.5 nm) and Strontium ions (422 nm) [115], these functional devices can also find application in integrated quantum optics. Furthermore, the CMOS-compatibility of AlN material shows the potential for manufacturable UV and visible photonics integrated circuit in large scale and with low cost. For UV wavelength, the AlN-based functional devices covered in this section include light emitters [85–87, 116–118], waveguide-based microring resonators [84, 115], photodetectors [119–122], and nonlinear optical generators [73, 93, 123], which enable the integrated UV photonic circuit. For visible wavelength, the functional devices covered in this section include adiabatic coupler [124], waveguides [82, 125], quantum emitters [72, 126, 127], optical modulator [91], as well as nonlinear optical generators based on both second-order nonlinearity [54, 94–98, 128–130] and third-order nonlinearity of AlN [99, 131–134].

3.1 Integrated linear optics devices

In order to couple light onto chip, the key optical device is integrated coupler. In 2012, grating-based vertical coupler has been demonstrated using a single-step lithography without partial etch in the study by Ghosh et al. [135]. The coupler works at 1550 nm communication wavelength, with coupling efficiency of −6.6 dB and a 1 dB bandwidth of 60 nm. Furthermore, the coupling efficiency has been significantly improved to −0.97 dB at 1550 nm recently in the study by Zhao et al. [124], through a suspended adiabatic coupler. The coupler also works for 780 nm, with coupling efficiency of −2.6 dB.

Also, in 2012, AlN has been proposed as a new material system for integrated optics in the study by Pernice et al. [82]. Wafer-scale sputtering process of AlN enables large-scale photonics device fabrication. The optical images of fabricated microring resonators for NIR and visible wavelength are illustrated in Figure 2(a) and Figure 2(b)

Table 2: Summary of AlN-based linear optical and optomechanical devices.

Wavelength	Device structure	AlN fabrication technique	Cavity *Q*	Optical loss	Reference/ year
1550 nm	Grating coupler	Magnetron reactive sputtering	N.A.	6.6 dB	[135]/2012
1550 nm, 780 nm	Adiabatic coupler	Magnetron reactive sputtering	N.A.	TM/TE: 0.97 dB/1.55 dB @ 1550 nm 2.6 dB/2.6 dB @ 780 nm	[124]/2020
C-band (1520–1580 nm), around 770 nm	Waveguide, microring resonator	Magnetron reactive sputtering	4.4×10^5 @ C-band, 3×10^4 around 770 nm,	0.8 dB/cm @ C-band	[82]/2012
2500 nm	Straight/bent waveguides, Y-junction beam splitters	Magnetron reactive sputtering	N.A.	0.83 dB/cm	[89]/2014
2500–3000 nm	Si-on-AlN waveguide	Magnetron reactive sputtering	N.A.	2.21 dB/cm @ 2750 nm	[136]/2017
3660–3900 nm	Waveguide, directional coupler, interferometer, microring resonator	Magnetron reactive sputtering	3.0×10^3 @ 3.67 μm (microring)	0.8 dB/mm (waveguide)	[90]/2019
450–1553 nm	Waveguide	Metal-organic chemical vapor deposition (MOCVD) AlN on sapphire	N.A.	0.7 dB/cm @1553 nm	[125]/2014
Telecom band	Microring resonator and edge coupler	Epitaxial AlN on sapphire substrate via MOCVD	2.5×10^6 for TE_{00}, 1.9×10^6 for TM_{00}, (microring)	0.14 dB/cm for TE_{00}, 0.2 dB/cm for TM_{00} @ telecom band	[137]/2017
1550 nm	Microring resonator (with thermal tuning)	Epitaxial AlN on sapphire substrate via MOCVD	3.2×10^6	N.A.	[138]/2016
UV (~210 nm) to IR	Microring resonator	Crystalline AlN on sapphire via magnetron reactive sputtering	1.4×10^5 @ 638 nm, 2.4×10^4@ 369.5 nm	5.3 dB/cm @ 638 nm 75 dB/cm @ 369.5 nm	[115]/2018
390 nm	Microring resonator	Epitaxial AlN on sapphire substrate via MOCVD	2.1×10^5	~8 dB/cm @ 390 nm	[84]/2018
1545 nm	Suspended ring optomechanical resonator	Magnetron reactive sputtering	1.25×10^5	N.A.	[103]/2012
1531 nm	Suspended photonic crystal (PhC) optomechanical resonator	Magnetron reactive sputtering	1.46×10^5	N.A.	[139]/2012
1547 nm	Suspended PhC optomechanical resonator	Patterning on AlN-on-insulator wafers	1.2×10^5	N.A.	[104]/2013
1550 nm	Racetrack ring optomechanical resonator	Magnetron reactive sputtering	4×10^4	N.A.	[69]/2014
1530 nm	PhC optomechanical resonator	Magnetron reactive sputtering	5×10^4	N.A.	[107]/2015
1626 nm	Racetrack ring optomechanical resonator	Magnetron reactive sputtering	7.67×10^3	N.A.	[106]/2016
Around 1540 nm	Racetrack ring optomechanical resonator	Magnetron reactive sputtering	1.71×10^5 (TE_{00}) 9.5×10^4 (TE_{10})	N.A.	[62]/2018
1531.5 nm	PhC optomechanical resonator	N.A.	1.3×10^5	N.A.	[61]/2013
1523 nm	Si ridge waveguide with AlN layer on top	Magnetron reactive sputtering	N.A.	<0.15 dB/cm (Si waveguide)	[63]/2020

respectively. The simulated fundamental transverse electric (TE) mode confined by the waveguide at 1550 and 770 nm are illustrated in Figure 2(c) left and right panel, respectively. The waveguide width is designed to be 1 μm and 350 nm respectively, with fixed height of 330 nm for both. At NIR and visible wavelengths, the zoom-in spectrum of the microring resonator are presented in Figure 2(d) left and right panel, respectively. Low-loss waveguide (0.8 dB/cm at *C*-band) and high-*Q* broadband ring resonator (4.4×10^5 at 1549 nm, 3×10^4 at 770 nm) have been demonstrated, illustrating the potential of AlN as a low-loss material for wide applications.

By using the same sputtering deposition process, in 2014, the working wavelength of AlN waveguide has been extended to MIR wavelength regime (λ = 2500 nm), with 0.83 dB/cm loss [89]. In the same work, *Y*-junction 50:50 beam splitter with over 200 nm spectral bandwidth has also been demonstrated working in the same wavelength regime. Furthermore, Si-on-AlN MIR photonic chips have been demonstrated in 2017 in the study by Jin et al. [136]. In the same work, the photonic waveguide has been applied for label-free chemical sensing within the wavelength range of 2500–3000 nm. Also, by leveraging on the sputtered AlN on SiO_2 platform, in 2019, the working wavelength of the photonics devices has been further extended beyond 3 μm [140]. The scanning electron microscopy (SEM) image of the patterned AlN microring resonator before upper cladding deposition is shown in Figure 2(e) left panel. The transmission electron microscopy (TEM) image of the waveguide cross-section after the upper cladding deposition is illustrated in Figure 2(e) right panel. A constant propagation loss is measured to be around 1.74 dB/mm in the wavelength range of 3.66–3.9 μm, and the microring resonator cavity *Q* is obtained to be 1.9×10^3 within the same wavelength range. The waveguide loss and the cavity *Q* can be significantly improved by thermal annealing for the chip [90]. The waveguide loss under different thermal annealing conditions have been shown in Figure 2(f) left panel. It can be found that the annealing process at 400 °C for 4 h gives the lowest loss result. After such annealing process, the loss can be reduced by half, which is around 0.8 dB/mm, and the cavity *Q* can be improved to 3.0×10^3, with spectrum shown in Figure 2(f) right panel. The power extinction ratio (ER) of 18 dB is achieved at the drop port of the microring resonator. For AlN-based photonics in MIR, one more point worth mentioning is that although AlN material has wide transparency window, the waveguide working wavelength in MIR will be limited by the transparency window of cladding layer material, typically either sapphire or SiO_2, up to 4–5 or 3–4 μm, respectively [141].

Besides using sputtering process for AlN thin film deposition, in 2014, a low loss photonic waveguide using epitaxial AlN on sapphire substrate deposited through metal-organic chemical vapor deposition (MOCVD) has been demonstrated in the study by Soltani et al. [125]. The single-crystal AlN waveguide optical loss is reported to be 0.7 dB/cm at 1553 nm. The dispersion property and the low optical loss further prove the effectiveness of wide bandgap integrated photonics platform using AlN. Leveraging on the same AlN-on-sapphire platform, AlN waveguide with remarkably low loss has been demonstrated in the study by Liu et al. [137]. The waveguide loss has been reported to be 0.14 and 0.2 dB/cm for TE_{00} and TM_{00} mode, respectively, at telecom wavelength. The microring cavity intrinsic *Q* value has been obtained as 2.5×10^6 and 1.9×10^6, respectively.

Taking the advantage of wide transparency window of AlN, and the low-loss of AlN-on-sapphire platform, waveguide and microring resonator cavity at UV wavelength have been demonstrated in the study by Liu et al. [84]. Figure 2(g) shows the simulated optical mode confined within AlN microring resonator at 390 nm wavelength, with waveguide width variation from 0.4 to 0.8 μm. The false-colored SEM image of one fabricated device (patterned AlN without top cladding) is provided in Figure 2(h). The zoom-in view of the coupling area between waveguide and microring is shown in Figure 2(i) top panel. The cleaved facet of the waveguide with SiO_2 top cladding is illustrated in Figure 2(i) bottom panel. The spectrum response (TE mode) of two cascaded microrings with slightly different diameters has been measured, as illustrated in Figure 2(j). The zoom-in view of TE_{00} resonances I and II are presented in Figure 2(k) left and right panel, respectively. The highest intrinsic *Q* of the cavity can be obtained as 2.1×10^5, which is a significant improvement compared with the earlier reported result [115]. Based on the cavity *Q*, the waveguide loss can be derived as ~8.0 dB/cm, which is also a significant improvement compared with the earlier reported value of 75 dB/cm at 369.5 nm [115]. Such low loss and high cavity *Q* are due to the good thin film quality of single-crystalline AlN, engineered waveguide dimensions and the optimized fabrication process.

Besides the passive waveguide, the active tuning of the AlN-based microring resonator has also been demonstrated in the study by Liu et al. [138] for microwave photonics (MWP) application. The platform is still AlN-on-sapphire for integrated optics. The reported MWP phase shifter is able to tune the phase for broadband radio frequency (RF) signal from 4 to 25 GHz using thermal-optic effect. The thermal shift of AlN microring is achieved by controlling the optical power in waveguide.

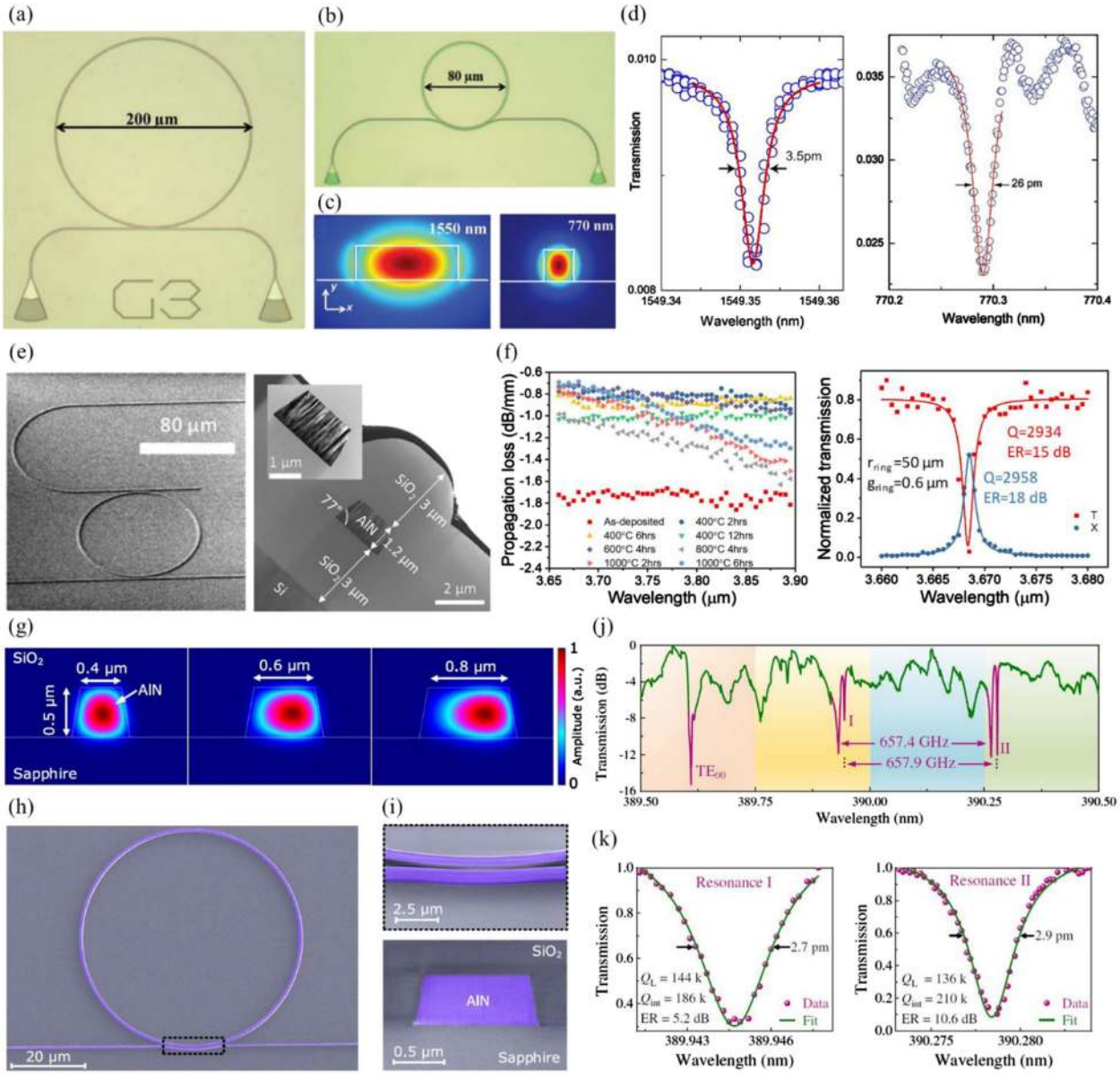

Figure 2: AlN-based integrated linear optical devices.
(a) Microscopic image of fabricated microring resonator working at NIR. (b) Microscopic image of fabricated microring resonator working at visible. (c) Simulated fundamental TE mode within AlN waveguide cross section at 1550 nm (left panel) and 770 nm (right panel). (d) Zoom-in spectrum response of the microring resonator around wavelength of 1550 nm (left panel) and 770 nm (right panel). The corresponding cavity Q are measured to be 4.4×10^5 at 1549 nm, 3×10^4 at 770 nm. (a)–(d) Adapted with permission from [82] © The Optical Society. (e) Left panel: SEM image of patterned AlN microring resonator (without top cladding) designed for MIR wavelength range. Right panel: TEM image of fabricated AlN waveguide for MIR working wavelength. Inset: zoom-in view of the AlN waveguide. (e) is adapted with permission from [140] © The Optical Society. (f) Left panel: waveguide propagation loss under different annealing conditions within the wavelength range of 3.66–3.9 μm. Annealing process at 400 °C for 4 h gives the lowest loss: 0.8 dB/mm, which is about half of the original loss. Right panel: spectrum response of the microring resonator after annealing process, showing Q value of 3.0×10^3 and extinction ratio (ER) of 18 dB. (f) is adapted with permission from [90] © The Optical Society. (g) Simulated optical mode confined by AlN microring resonator, with waveguide width variation from 0.4 to 0.8 μm. (h) False-colored SEM image of patterned AlN waveguide on sapphire substrate without top cladding. (i) Top panel: zoom-in view of waveguide to microring coupling region. Bottom panel: waveguide facet with top SiO_2 cladding. (j) Spectrum response of two cascaded microrings with slightly different diameters. (k) Zoom-in view of spectrum response of resonance I (left panel) and resonance II (right panel). The highest intrinsic cavity Q can be obtained as 2.1×10^5. (g)–(k) Adapted with permission from [84] © The Optical Society.

3.2 Integrated optomechanical devices

Contributed by the piezoelectric effect and excellent electro-mechanical properties, AlN has been widely used as material platform for microelectromechanical resonators. Good optical properties mentioned earlier make AlN a very suitable material for optomechanical devices. In 2012, an integrated AlN-based suspended mechanical microring resonator has been demonstrated with high optical Q factor in the study by Xiong et al. [103]. The false-color SEM image of the fabricated microring is illustrated in Figure 3(a). One of the optical resonances at 1544.85 nm is shown in Figure 3(b), demonstrating optical Q factor of 1.25×10^5. The optically transduced RF spectrum of the mechanical modes of the ring cavity has also been captured, with zoom-in view shown in Figure 3(c). Top, middle and bottom panel show the resonance at 30.6 MHz, 47.3 MHz, and 1041.5 MHz respectively. At 30.6 MHz, the simulated displacement profile for the wine-glass mode has also been included as inset. The device can be used as an optical cavity for sensitive displacement readout, to resolve the thermomechanical motions of the ring contour modes with frequency over GHz.

Besides the microring cavity, photonic crystal (PhC) optomechanical nanocavities have also been reported by the same group [104, 139]. In the work reported in 2013 in the study by Fan et al. [104], the piezoelectrically actuated one-dimensional (1D) acoustic and PhC nanocavity has been demonstrated. The false-color SEM image of the fabricated suspended PhC nanocavity is shown in Figure 3(d). The red, green and blue color represent the PhC nanocavity, optical waveguide, and stress release structure, respectively. The simulated optical and mechanical mode profiles are presented in Figure 3(e) top and bottom panel, respectively. Two modes have significant overlap at the central area of PhC. Figure 3(f) illustrates the optical spectrum response of the PhC nanocavity. At the resonance wavelength of 1547.1 nm, the intrinsic cavity Q is reported to be 1.2×10^5. The S_{21} coefficient of the piezo-acousto-photonic crystal nanocavity is measured by network analyzer. The obtained results including the magnitude and phase are shown in Figure 3(g), in which the inset shows the magnitude from 2.0 to 4.0 GHz. The piezoelectric actuation of mechanical mode at 3.18 GHz has been demonstrated with mechanical cavity Q of $>1 \times 10^4$.

Since the optomechanical resonance cavities discussed above can be simultaneously used as optical and mechanical cavity, they provide a platform for photon–phonon interaction, which can be used as acoustic-optic modulator [69, 107]. A schematic showing the interaction between the surface acoustic wave (SAW) and the optical wave is illustrated in Figure 4(a), in which the optical mode is confined by the ridge waveguide formed by AlN on SiO_2 layer. The simulated optical mode, acoustic mode (under two acoustic wavelengths of 2W and W/2), and their

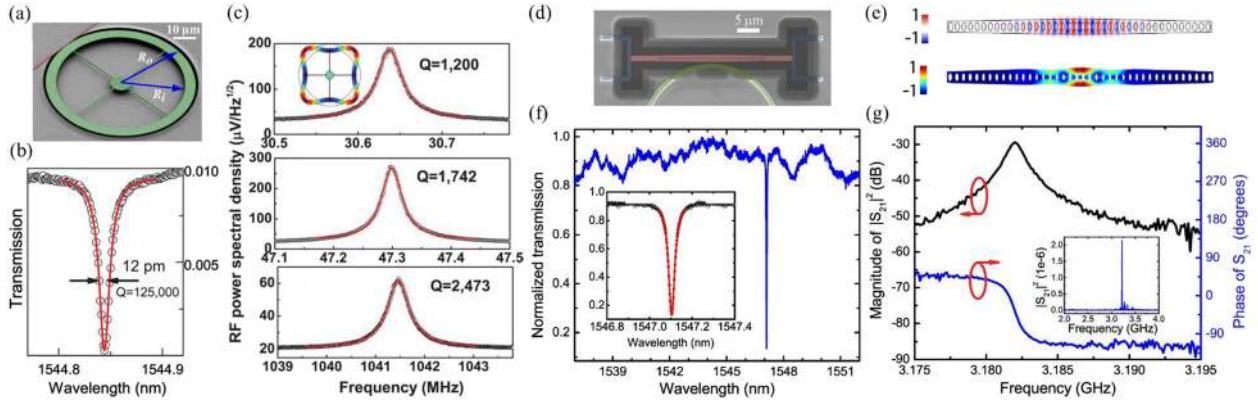

Figure 3: AlN-based integrated optomechanical devices.
(a) False-color SEM image of microring-shaped optomechanical resonator. Suspended microring resonator is marked in green. Photonic coupling waveguide is marked in red. (b) One of the optical resonance spectral, showing optical cavity Q of 1.25×10^5 at resonance wavelength of 1544.85 nm. (c) Top, middle and bottom panel: zoom-in spectra of mechanical modes at 30.6, 47.3 and 1041.5 MHz, respectively. The fitted curves give the mechanical cavity Q of 1200, 1742, and 2473, respectively. Inset in top panel shows the simulated displacement profile for wine-glass mode at 30.6 MHz. (a)–(c) Adapted from [103], with the permission of AIP Publishing. (d) False-color SEM image of piezo-acousto-photonic crystal nanocavity. Piezo-acousto-photonic nanocavity, photonic coupling waveguide, and stress release structure are marked in red, green and blue color, respectively. (e) Top and bottom panel: simulated optical and mechanical mode profile within the piezo-acousto-photonic crystal nanocavity. (f) Optical spectrum of PhC cavity. Intrinsic cavity Q can be obtained as 1.2×10^5 at 1547.1 nm. Inset shows the zoom-in view near the optical resonance. (g) S_{21} magnitude and phase of the piezo-acousto-photonic crystal nanocavity. Inset shows S_{21} magnitude at the frequency between 2.0 and 4.0 GHz. (d)–(g) Adapted from [104], with the permission of AIP Publishing.

overlap are presented in Figure 4(b). The optical mode is launched by coupling light into the racetrack resonator. The acoustic mode is excited by inter-digital transducer (IDT) placed nearby the racetrack. The microscopic image is shown in Figure 4(c), together with the SEM image showing zoom-in view of IDT electrode fingers having a period D of 400 nm. The optical characterization result of the racetrack resonator is shown in Figure 4(d), achieving intrinsic Q value of 8×10^4. The acoustic modulation of the optical resonator is illustrated in Figure 4(e). The left panel shows the spectra of S_{21} transmission coefficient of the acousto-optic device, with peaks labeled with Rayleigh mode orders. The right panel shows the modulation response with respect to the laser detuning relative to the optical resonance wavelength for R6 mode under acoustic wavelength of 0.9 μm. The dip at the center indicates that the acoustic wave adds modulation on optical phase.

Besides the racetrack/ring resonator discussed above, the PhC nanocavity has also been used as optomechanical system for phonon–photon coupling, through SAW [107] or suspended optomechanical system [61], achieving RF modulation with frequency up to 12 and 4.2 GHz, respectively. The schematic of SAW generated by IDT propagating towards the PhC nanocavity is illustrated in Figure 4(f) top panel. The microscopic image of the fabricated device is provided in Figure 4(f) middle panel. Two grating-based vertical couplers are used to couple light into and out of the waveguide, which is side-coupled to the PhC nanocavity. The Figure 4(f) bottom panel shows the false-colored SEM image of PhC nanocavity side-coupled to a straight waveguide (marked in green). The IDT (marked in yellow) for SAW generation can also be clearly observed. The spectra of fundamental mode resonance (around 1530 nm) of the PhC nanocavity is presented in Figure 4(g), showing a narrow linewidth of 3.88 GHz. The system transmission coefficient S_{21} and reflection coefficient S_{11} are measured by vector network analyzer (VNA), with obtained spectrum shown in Figure 4(h). Different Rayleigh modes (R1–R15) can be observed from the spectrum of transmission coefficient S_{21}. The right panel of Figure 4(h) shows the zoom-in view of the transmission and reflection spectra for R14 mode. At such R14 mode, the peak value of S_{21} under various laser detuning relative to the cavity resonance is recorded and shown in Figure 4(i), in which the measured data (red dots) are fitted with theoretical model (blue line).

Through phonon–photon coupling, the SAW not only can modulate the optical signal, but also can be used to achieve optical isolation on chip [62, 63]. Under the condition that the SAW propagation direction is perpendicular to the optical wave propagation direction, the device functions as an acousto-optic phase modulator. There will be two side-bands evenly located on both sides of the optical signal in frequency domain. While under the condition that the SAW direction has an angle rather than 90° with respect to the waveguide direction, the device will function as an optical isolator or nonreciprocal modulator, due to the breaking of geometric symmetry. Such optical isolator provides a solution to make monolithically integrated optical isolation using CMOS-compatible fabrication process, rather than using magneto-optical material [142, 143], or PhC structure which requires patterning with small critical dimension (CD) [144]. An additional note is that the optical waveguide in the study by Kittlaus et al. [63] is Si ridge waveguide embedded in SiO_2 with an AlN layer on top, while in the study by Sohn et al. [62], both optical mode and acoustic mode are confined in AlN ridge waveguide. Furthermore, the earlier case of building AlN electromechanical transducer on Si (AlN-on-Si platform [145]) to achieve optomechanical functionality has also been used to make the quantum optomechanical devices, as reported in [146, 147].

3.3 Optical emitters and photodetectors

Contributed by the large bandgap and wide transparency window down to UV range, AlN has also been used in combination with Gallium Nitride (GaN) as light emitting material for UV light generation [85–87, 116–118, 148]. The study by Mexis et al. [148] reports high Q factor microdisk cavity with GaN quantum dots grown on AlN and AlGaN barriers. The GaN/AlN microdisk shows a Q value of more than 7×10^3. In the study by Sam-Giao et al. [116], a high Q factor AlN nanocavity has been demonstrated, which is based on PhC membrane. The AlN thin film is grown on Si through ammonia molecular beam epitaxy (MBE), and contains the GaN quantum dots. The SEM image of the patterned PhC nanocavity is shown in Figure 5(a), including a waveguide structure in the middle. The room-temperature photoluminescence results of the nanocavities with different PhC designs are illustrated in Figure 5(b). The Q factor of 4.4×10^3 and 2.3×10^3 have been obtained at wavelengths of 395 and 358 nm, respectively. In order to reduce the lattice mismatch on Si substrate, in the study by Sergent et al. [117], the GaN/AlN quantum dots are first grown on SiC substrate, and then transferred to Si substrate using a bonding process. The PhC structure is then patterned using electron-beam lithography, followed by hydrofluoric acid etching to remove the bonding material beneath to form suspended membrane. The SEM images of the fabricated PhC suspended nanocavity are presented in Figure 5(c). At the wavelength of 399 nm, the

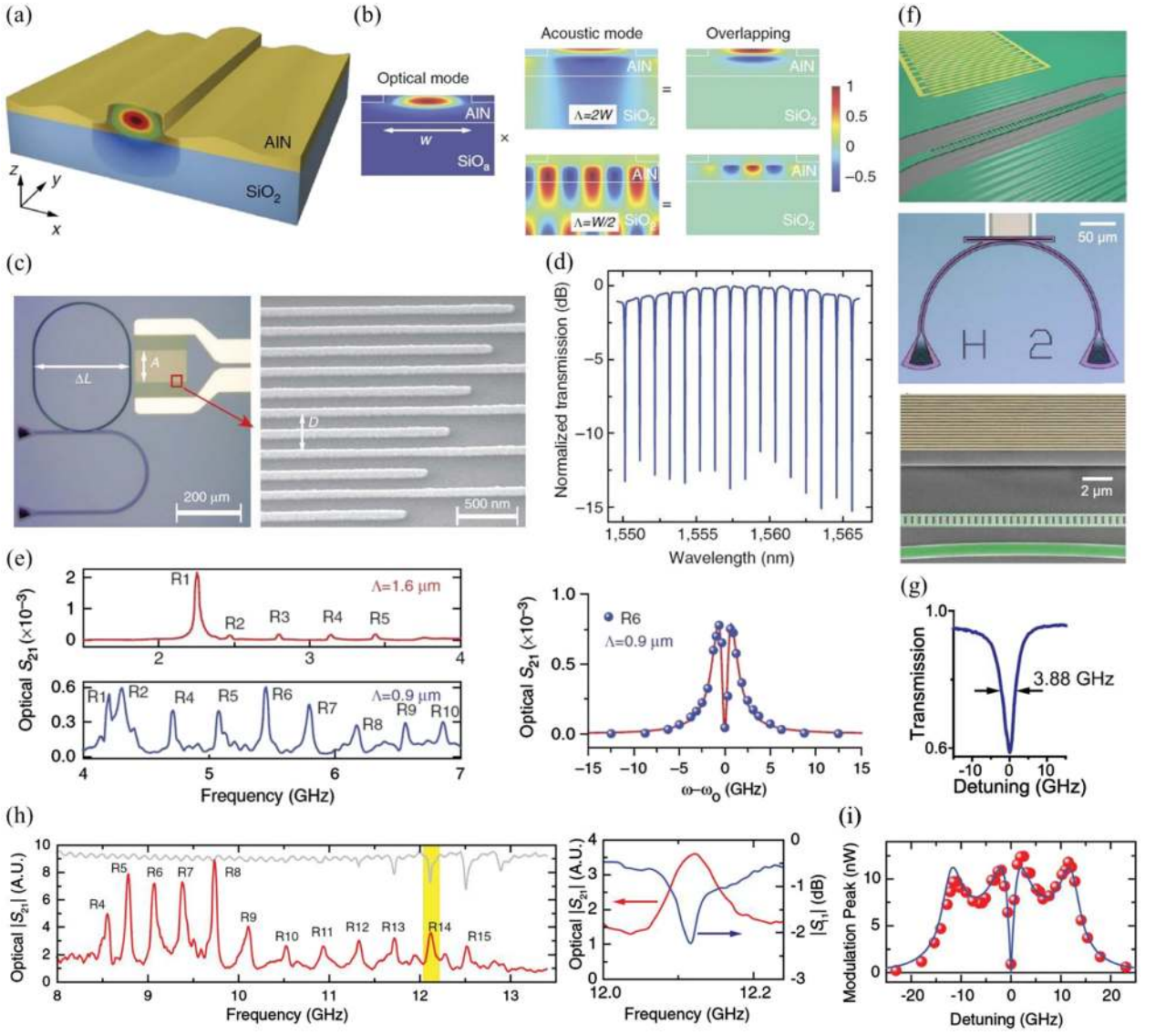

Figure 4: AlN-based integrated devices with SAW induced photon–phonon coupling.
(a) Schematic of AlN waveguide illustrating the coupling between the SAW and optical mode. (b) Simulated optical mode, acoustic mode (under two acoustic wavelengths of 2W and W/2), and their intensity overlap within the AlN-based waveguide. (c) Left panel: optical microscopic image of fabricated system, showing IDT placed beside the racetrack ring resonator for SAW coupling. Two vertical couplers are used for optical mode coupling. Right panel: SEM image of IDT electrode fingers with a period D of 400 nm. (d) Optical transmission spectrum of the racetrack resonator, showing loaded Q of 4×10^4, corresponding to an intrinsic Q of 8×10^4. (e) Left panel: measured system spectra of S_{21} transmission coefficient with peaks labeled with Rayleigh mode orders. Right panel: R6 mode modulation response with respect to the laser detuning relative to the optical resonance wavelength under acoustic wavelength of 0.9 μm. (a)–(e) Adapted with permission from Springer Nature, Nature Communications [69]. Suboptical wavelength acoustic wave modulation of integrated photonic resonators at microwave frequencies, S. A. Tadesse, et al. Copyright 2014. (f) Top panel: schematic of SAW generated by IDT propagating towards the PhC nanocavity. Middle panel: microscopic image of the fabricated device, with two grating-based vertical couplers to couple light into and out of the waveguide, and metallic IDT for SAW coupling. Bottom panel: false-colored SEM image of PhC nanocavity side-coupled to a straight waveguide (marked in green), and IDT (marked in yellow) for SAW generation. (g) Spectra of fundamental mode resonance (around 1530 nm) of the PhC nanocavity, showing a narrow linewidth of 3.88 GHz. (h) Left panel: spectra of system transmission coefficient S_{21} and reflection coefficient S_{11}. Right panel: zoom-in view of the transmission and reflection spectra for R14 mode. (i) Peak value of S_{21} under various laser detuning relative to the cavity resonance for R14 mode. Measured data (red dots) are fitted with theoretical model (blue line). (f)–(i) Adapted with permission from [107] © The Optical Society.

Table 3: Summary of AlN-based emitters, photodetectors and metasurfaces.

Wavelength	Functional device	Device structure	AlN fabrication technique	Reference/ year
410 nm ($Q > 7.0 \times 10^3$)	Emitter	Microdisk with embedded GaN/Al(Ga)N quantum dots	Quantum dot samples grown by ammonia molecular beam epitaxy (MBE)	[148]/2011
358 nm, 395 nm	Emitter	AlN (containing GaN quantum dots) PhC membrane	AlN grown on Si by ammonia MBE	[116]/2012
399 nm ($Q > 6.3 \times 10^3$)	Emitter	1D PhC nanobeam cavity embedding GaN/AlN quantum dots	AlN epilayer with GaN quantum dot plane grown by MOCVD on SiC substrate, then transfer to Si substrate	[117]/2012
210 nm	Light emitting diode (LED)	Nitrogen (N) polar Al(Ga)N nanowires grown on Si substrate	Radio-frequency plasma-assisted MBE under nitrogen-rich condition	[118]/2015
360 nm	LED	GaN/AlN double-barrier heterostructure on GaN substrate	Plasma-assisted MBE	[85]/2018
221–258 nm	Emitter	AlGaN/AlN multiple quantum wells on bulk AlN substrate	Metalorganic vapor phase epitaxy (MOVPE)	[86]/2019
225 nm (5.5 eV), 248 nm (5 eV)	Emitter	1 or 2 monolayer GaN/AlN quantum well	MOVPE	[87]/2019
550–1000 nm	Single photon quantum emitter at room temperature	2 μm thick AlN layer on sapphire	MOCVD AlN on sapphire	[126]/2020
Around 590 nm (~2.1 eV)	Single photon quantum emitter at room temperature	1 μm thick AlN layer on sapphire	Epitaxial deposition of AlN on sapphire substrate	[72]/2020
580–650 nm	Quantum emitter at room temperature	200 nm thick AlN layer on sapphire	*C*-axis crystalline AlN grown on sapphire by plasma vapor deposition of nanocolumns, with He ion implementation	[127]/2020
193 nm	Photodetector (optoelectric)	AlN micro/nanowire	AlN micro/nanowires grown by physical vapor transport at a tungsten crucible in nitrogen environment	[119]/2015
280–330 nm and 330–360 nm	Photodetector (optoelectric)	GaN nanowire with embedded GaN/AlN superlattice	Plasma-assisted MBE	[120]/2017
1550 nm	Photodetector (optoelectric)	GaN nanowire with embedded GaN/AlN superlattice	Plasma-assisted MBE	[149]/2017
325 nm, 193 nm	Photodetector (optoelectric)	ZnO/AlN core/shell nanowire arrays aligned vertically	Vapor phase transport for ZnO nanowire array and radio frequency magnetron sputtering for AlN	[121]/2019
200–500 nm	Photodetector (optoelectric)	Monolayer of organic molecules on AlN-based metal-semiconductor-metal structure	Epitaxial AlN film on sapphire by physical vapor deposition with nanocolumns	[122]/2020
5–6 μm (MIR)	Photodetector (pyroelectric)	AlN membrane with patterned metal layer on top for wavelength selectivity	Magnetron reactive sputtering	[71]/2014
4.17 μm (MIR)	Photodetector (pyroelectric)	AlN thin film on Si_3N_4/SiO_2 membrane	Magnetron reactive sputtering	[64]/2019
Medium to long wave IR	Photodetector (pyroelectric)	AlN thin film on SiO_2 membrane	Magnetron reactive sputtering	[111]/2019
660–2000 nm	Photodetector (pyroelectric)	AlN layer embedded between Au and Si contact layers	Magnetron reactive sputtering	[65]/2020
5–14 μm (MIR)	Photodetector (pyroelectric)	AlN thin film on SiO_2 membrane	Magnetron reactive sputtering	[112]/2020
IR	Photodetector (pyroelectric)	Scandium-doped AlN thin film on SiO_2 membrane	Magnetron reactive sputtering	[66]/2020
375 nm	Lens, three-dimensional (3D) router	Metasurface	Magnetron reactive sputtering on sapphire substrate	[88]/2020

Q factor of nanocavity is reported to be 6.3×10^3 with Lorentzian fitting, and 1.1×10^4 with Voigt fitting. The measured Q factors of PhC with varied hole radius at different wavelengths are presented in Figure 5(d).

To overcome the limitation on the internal quantum efficiency in UV wavelength, in the study by Zhao et al. [118], nitrogen (N)-polar AlN nanowires grown directly on Si substrate have been demonstrated with a record high internal quantum efficiency of 80% at room temperature. The schematic of AlN nanowire grown on GaN nanowire and Si substrate is illustrated in Figure 5(e). The SEM image of the fabricated nanowire is presented in Figure 5(f), in which the highly uniform and vertically aligned nanowires can be clearly observed. The photoluminescence spectra of the nanowires are captured with 1 mW excitation power and under 20 and 300 K, as shown in Figure 5(g). By taking

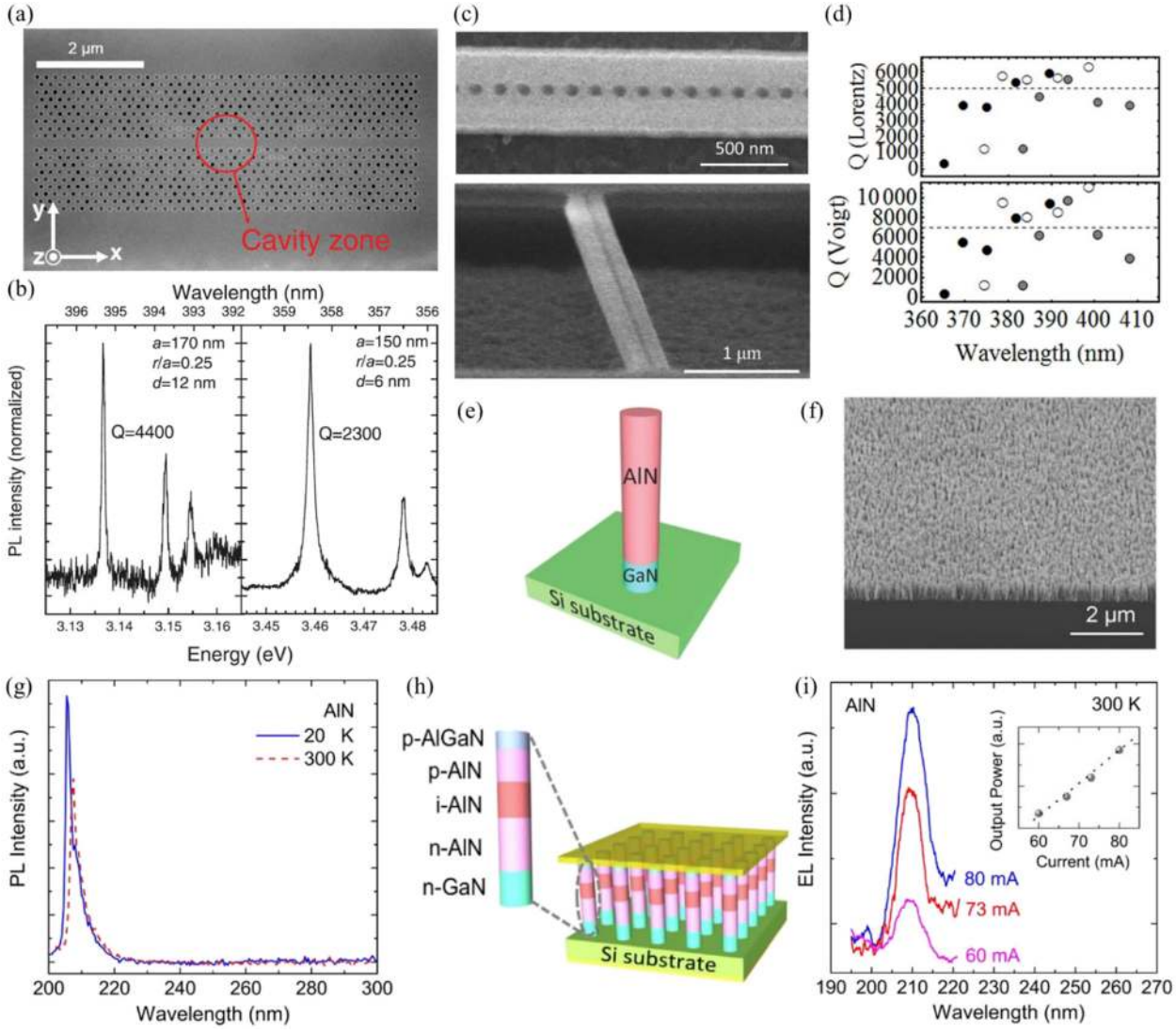

Figure 5: Al(Ga)N-based semiconductor UV emission light sources.
(a) SEM image of AlN suspended structure with PhC and waveguide formed in the middle. (b) Photoluminescence spectra of PhC nanocavity obtained at room temperature, showing high Q factor. (a)–(b) Adapted from [116], with the permission of AIP Publishing. (c) Top and Bottom: top and tilted view SEM images of transferred suspended PhC nanocavity from SiC to Si substrate. (d) Q factors obtained from photoluminescence spectra with varied PhC design at different wavelengths. Top: Lorentz fitting. Bottom: Voigt fitting. (c)–(d) Adapted from [117], with the permission of AIP Publishing. (e) Schematic of AlN nanowire on GaN nanowire and Si substrate. (f) SEM image of fabricated AlN/GaN nanowires on Si, showing uniform distribution and vertical alignment. (g) Photoluminescence spectra of AlN nanowires under 1 mW excitation power at the temperature of 20 and 300 K. (h) Schematic of AlN-nanowire-based LED. (i) Electroluminescence spectra of AlN-nanowire-based LED under different injection levels at room temperature, showing strong emission at 210 nm. Inset: linear relation between output power and injection current. (e)–(i) Adapted with permission from [118]. Licensed under a Creative Commons Attribution.

the ratio of intensity at 300 and 20 K, the internal quantum efficiency can be estimated to be 80% assuming a near-unity internal quantum efficiency at 20 K. In the same work, the first nanowire-based 210 nm LED has also been demonstrated, whose schematic is shown in Figure 5(h). The electroluminescence under different injection levels are obtained at room temperature, as shown in Figure 5(i). The emission peak at 210 nm can be clearly observed. Also, the linear relation between the output power and injection current can be found from inset of Figure 5(i).

Furthermore, GaN/AlN quantum wells with improved performances are recently reported [85–87]. In the study by Growden et al. [85], a unipolar n-doped GaN/AlN heterostructure has been reported, with electroluminescence spectra peak located at near-UV wavelength (360 nm). The light emitter overcomes the challenge of the p-type doping and contact, with holes created through Zener tunneling from valence band to conduction band. In the meanwhile, the study by Haughn et al. [86] reports the highly radiative nature of ultra-thin AlGaN/AlN quantum wells for deep UV emission. Also, in the study by Kobayashi et al. [87], GaN monolayer quantum wells with emission wavelength below 250 nm have been demonstrated. The internal quantum efficiency of GaN/AlN is reported to be 5% for a 1 monolayer GaN/AlN quantum well and 50% for a 2 monolayer GaN/AlN quantum well.

AlN has been used not only as one of the key semiconductor optoelectric materials for light emitters in UV, but also as host material of point detects for quantum emitters in visible and IR wavelength regime [72, 126, 127]. In the study by Xue et al. [126], the single photon emitter in single-crystalline AlN film that can emit in visible and NIR at room temperature has been reported for the first time. Figure 6(a) shows the photoluminescence spectra measured at 300 and 10 K. Two single photon emitters (SPE1, SPE2) are selected for autocorrelation measurement. The histogram of 74 emitters at 10 K in Figure 6(b) shows the emission wavelength coverage from 550 to 1000 nm. The autocorrelation results of SPE1 and SPE2 are presented in Figure 6(c). $g^{(2)}(0)$ of 0.10 ± 0.05 and 0.34 ± 0.05 are obtained for SPE1 at 10 K and SPE2 at 300 K, respectively. Also, based on AlN thin film on sapphire substrate, in the study by Bishop et al. [72], bright (>10^5 counts/s) and pure ($g^{(2)}(0) < 0.2$) quantum emission has been demonstrated at room temperature from color centers of AlN located around 2.1 eV. While the two works mentioned earlier ([72, 126]) are based on AlN thin films, the work reported in the study by Lu et al. [127] has moved one step further. It demonstrates the direct integration of quantum emitter within an AlN-based photonic integrated circuit. The schematic of the system is illustrated in Figure 6(d). The inset on the left shows the wurtzite crystal structure of AlN, and the inset on the right shows the microscopic image of the fabricated AlN waveguides and grating couplers. The cross-section of single-mode AlN-on-sapphire waveguide is shown in Figure 6(e), with quantum emitter embedded within AlN waveguide. The autocorrelation measurement result of the emitter via waveguide collection is presented in Figure 6(f), with $g^{(2)}(0) = 0.21 \pm 0.08$ reported. The photoluminescence intensity saturation response has also been plotted in Figure 6(g). The saturation rate of > 8.6×10^4 counts per second is obtained. Further, in the same work, for unpatterned AlN thin film, high photon counting rate of >8×10^5 counts per second and $g^{(2)}(0) \sim 0.08$ have been reported at room temperature. An additional note worth mentioning is that, besides the quantum emitters discussed earlier, AlN has also been used as waveguide for single-photon transmission [150] and quantum optics system [151].

Besides the emitters mentioned earlier, AlN has also been used as a key semiconductor material for photodetectors [119–122, 149]. In the study by Zheng et al. [119], an AlN nanowire structured photodetector working at 193 nm wavelength with short response time (<0.2 s) has been demonstrated. The method to prepare the defect-free, high-quality AlN nanowire has been reported in the same work. Also, GaN nanowire photodetectors with GaN/AlN superlattice embedded have been demonstrated, with working wavelength in UV [120] and NIR [149]. The NIR (1.55 μm) photodetection reported in the study by Lähnemann et al. [149] is claimed to be the first nanowire-based inter-subband photodetector. Furthermore, in the study by You et al. [121], ZnO/AlN core/shell nanowires for UV emission and detection have been demonstrated. Compared with the bare ZnO nanowires, the core/shell nanowires achieve 24 times enhancement of UV emission, higher photoresponsivity (from 3.8×10^3 to 2.05×10^4 A/W), and shorter response time (from 397 to 28 ms) for photodetection. These performance enhancements are mainly contributed by the higher crystal quality of core–shell nanowires and passivation of surface states of ZnO nanowires by crystal AlN shell. The photodetector performance reported in [121] has also been benchmarked with the earlier discussed work in [119], showing superior performance in terms of response speed and responsivity. Moreover, a recent work reported in the study by Kaushik et al. [122] makes use of a monolayer of organic molecules to passivate the surface states of AlN, and hence, to improve the performance of AlN-based UV photodetector. The surface modification

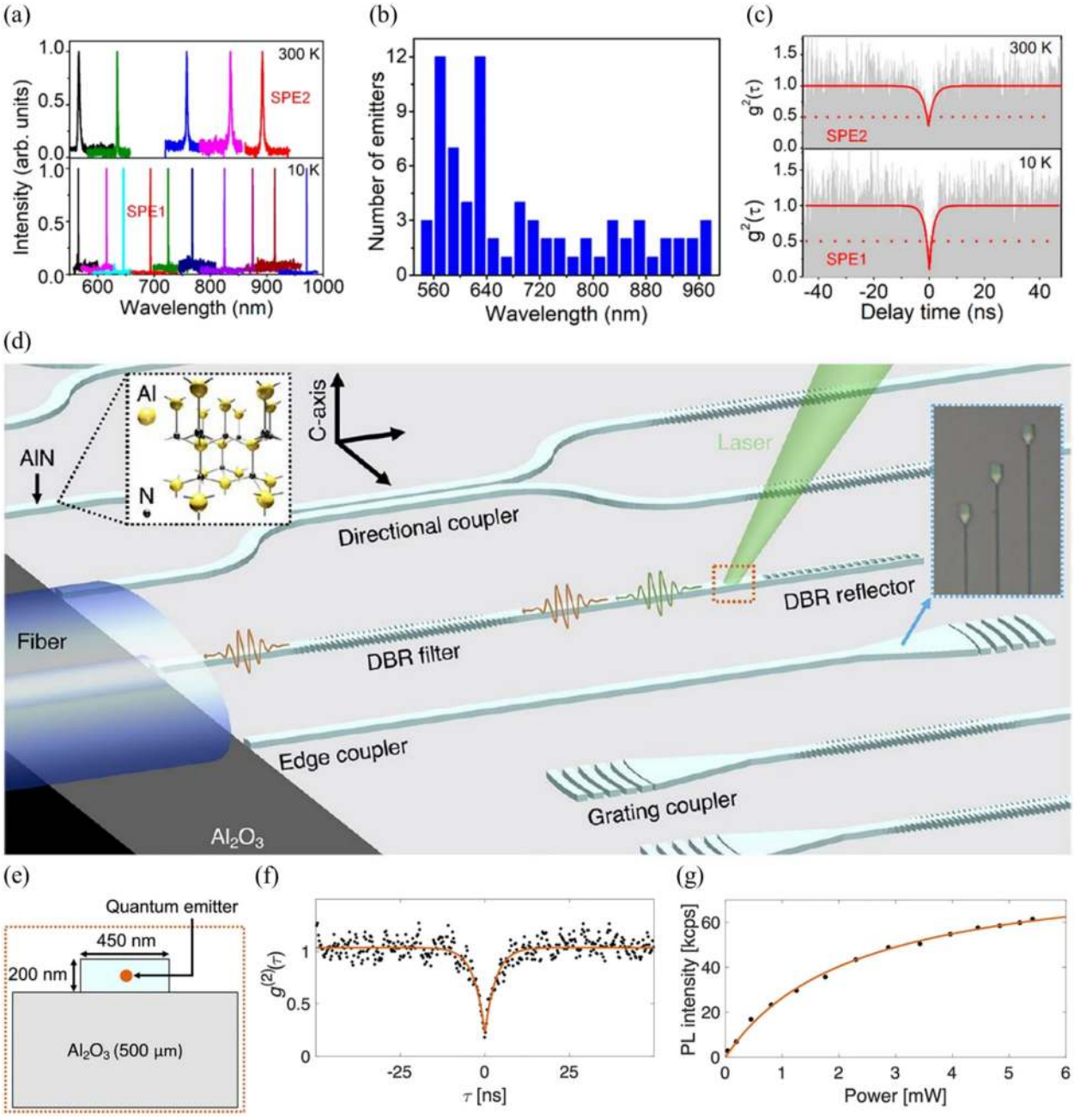

Figure 6: AlN-based quantum emitters.
(a) Photoluminescence spectra measured at 300 K (top panel) and 10 K (bottom panel). (b) Histogram showing the emission wavelength distribution of 74 emitters. (c) Normalized autocorrelation data for selected single-photon emitters (SPE1 and SPE2). $g^{(2)}(0)$ of 0.10 ± 0.05 and 0.34 ± 0.05 are obtained for SPE1 at 10 K and SPE2 at 300 K, respectively. Red dotted lines indicate the classical threshold of 0.5. (a)–(c) Adapted with permission from [126], copyright (2020) American Chemical Society. (d) Schematic of quantum emitter integrated within the photonic integrated circuits. Inset on the left: wurtzite crystal structure of AlN. Inset on the right: microscopic image of the fabricated AlN waveguides and grating couplers. (e) Cross-section of single-mode AlN-on-sapphire waveguide, with quantum emitter embedded within AlN waveguide (not necessarily to be right in the center). (f) Autocorrelation measurement of the emitter via waveguide collection, showing $g^{(2)}(0) = 0.21 \pm 0.08$. (g) Photoluminescence intensity saturation response of the emitter, with saturation rate of $>8.6 \times 10^4$ counts per second. (d)–(g) Adapted with permission from [127], copyright (2020) American Chemical Society.

enables the reduction of photodetector dark current by 10 times, and doubling of the responsivity from 0.3 to 0.6 mA/W.

The pyroelectric property of AlN also makes it a suitable material for MEMS-based thermal detector for sensing in IR wavelength [64, 65, 71, 111, 112]. Differentiating from

the above mentioned photodetector based on bandgap of semiconductor material, the mechanism of pyroelectric thermal detector is based on electrical voltage or current induced by the heat from electromagnetic radiation. In the study by Yamamoto et al. [71], a wavelength-selective pyroelectric sensor has been demonstrated, with schematics shown in Figure 7(a) (projected view) and Figure 7(b) (cross-sectional view). The wavelength selectivity is realized by periodic holes patterned on top molybdenum (Mo) metal layer. The patterned Mo layer forms the optical resonance within MIR wavelength. At the same time, the Mo layer is used for the collection of pyroelectric charge signal. The SEM images of the fabricated sensor and the patterned top Mo layer are shown in Figure 7(c) and Figure 7(d), respectively. The pitch and diameter of these holes determine the resonance wavelength for the sensor. The comparison between the measured absorption spectra of detectors with top Mo layer patterned and unpatterned are shown Figure 7(e) top panel. The patterned detector, with hole pitch size of 2 μm and hole diameter of 1.5 μm, has significant absorption near 4.5 and 5.5 μm wavelengths. The detector with unpatterned top Mo layer has close to 0 absorption due to the high reflectivity of the Mo metal at IR wavelength. The inset of Figure 7(e) top panel shows the result from finite difference time domain (FDTD) simulation, for the absorption of TE and TM polarized light. The pitch and diameter of hole array are fixed at 2 and 1.5 μm, respectively. The absorption under incident angles of 0° and 25° are investigated. For TM polarized light, the absorption spectra are similar for both 0° and 25° incident angles. While for TE polarized light, the main peak splits when the angle changes from 0° to 25°. Considering the light in measurement is continuously distributed within 25(±10)°, the measured broadening of the peaks may be contributed by the splitting of the TE absorption lines, as stated in the analysis of [71]. The absorption peak wavelength can be engineered by adjusting the etched hole array dimensions, as supported by the simulation results provided in Figure 7(e) bottom panel. The pitch is increasing from 1.75 μm to 2.0 μm and 2.25 μm, with hole array pitch and radius ratio fixed at 0.75. The red shift of the peak absorption can be observed with the increase of hole array dimension. Also, one more work related to wavelength/spectral selectivity worth mentioning is that in the study by Stewart et al. [65], AlN pyroelectric thin film has been integrated with a plasmonic metasurface to demonstrate spectrally selective (660–2000 nm), ultrafast (700 ps rise time) pyroelectric photodetector working at room temperature.

The CMOS-compatible pyroelectric photodetectors have also been explored and demonstrated in [64, 112]. The study by Ng et al. [112] reports the demonstration of AlN-based MEMS pyroelectric detectors fabricated on an 8-inch Si wafer. Hence, the detector devices have the potential to be integrated with the MEMS-based thermal emitter [10], and to realize miniaturized optical gas sensor for chemical gas sensing application. Furthermore, by doping Sc into AlN thin film, the pyroelectric coefficient of AlN can be enhanced [152]. As a result, the performance of the pyroelectric photodetector can be improved [66]. The schematic of ScAlN-based pyroelectric photodetector is shown in Figure 7(f), including the thicknesses of different layers. The SiO_2 rib array, as magnified in the figure, is designed to increase the mechanical stiffness of the device. The microscopic image of the fabricated device wire bonded on a Transistor Outline (TO)-39 header is illustrated in Figure 7(g). The detector die dimension is 3×1.8 mm. The membrane sensing area with ScAlN has a dimension of 536×536 μm, as marked out in the figure. The functionality of the detector can be visualized in Figure 7(h). A commercial MEMS thermal emitter has been used, driven by 1 Hz square wave modulated voltage. Figure 7(h) shows the time domain response from the detector. The positive and negative current peak corresponds to "on" and "off" of the thermal emitter, respectively. When the emitter is switched on, the pyroelectric photodetector senses the increase of temperature, and gives a positive current peak. When the emitter is switched off under square wave modulation, the pyroelectric photodetector senses the decrease of temperature, and hence gives a negative current peak. The current amplitude is measured to be around 2 nA. The performance of the ScAlN pyroelectric detector is compared with the AlN-based pyroelectric detector, showing improved performance in terms of specific detectivity ($\sim 6.08 \times 10^7$ cm$\sqrt{\text{Hz}}$/W) and noise equivalent power ($\sim 8.85 \times 10^{-10}$ W/$\sqrt{\text{Hz}}$).

3.4 Flat optics/metasurfaces

Flat optics/metasurface has attracted a lot of interests from both academic research and industry in the past decade. It is a thin layer of nanostructures patterned on a substrate, and has the potential to replace the bulky optical components. Differentiating from the traditional in-plane integrated photonics, metasurface-based devices are patterned to manipulate light that is incident on it. Similar to surface LED and earlier mentioned pyroelectric photodetectors, metasurfaces manipulate light under out-of-plane scheme. In the meanwhile, the optical phase profile after the metasurface can be engineered to achieve designed functionality. Optical devices with various functionalities have

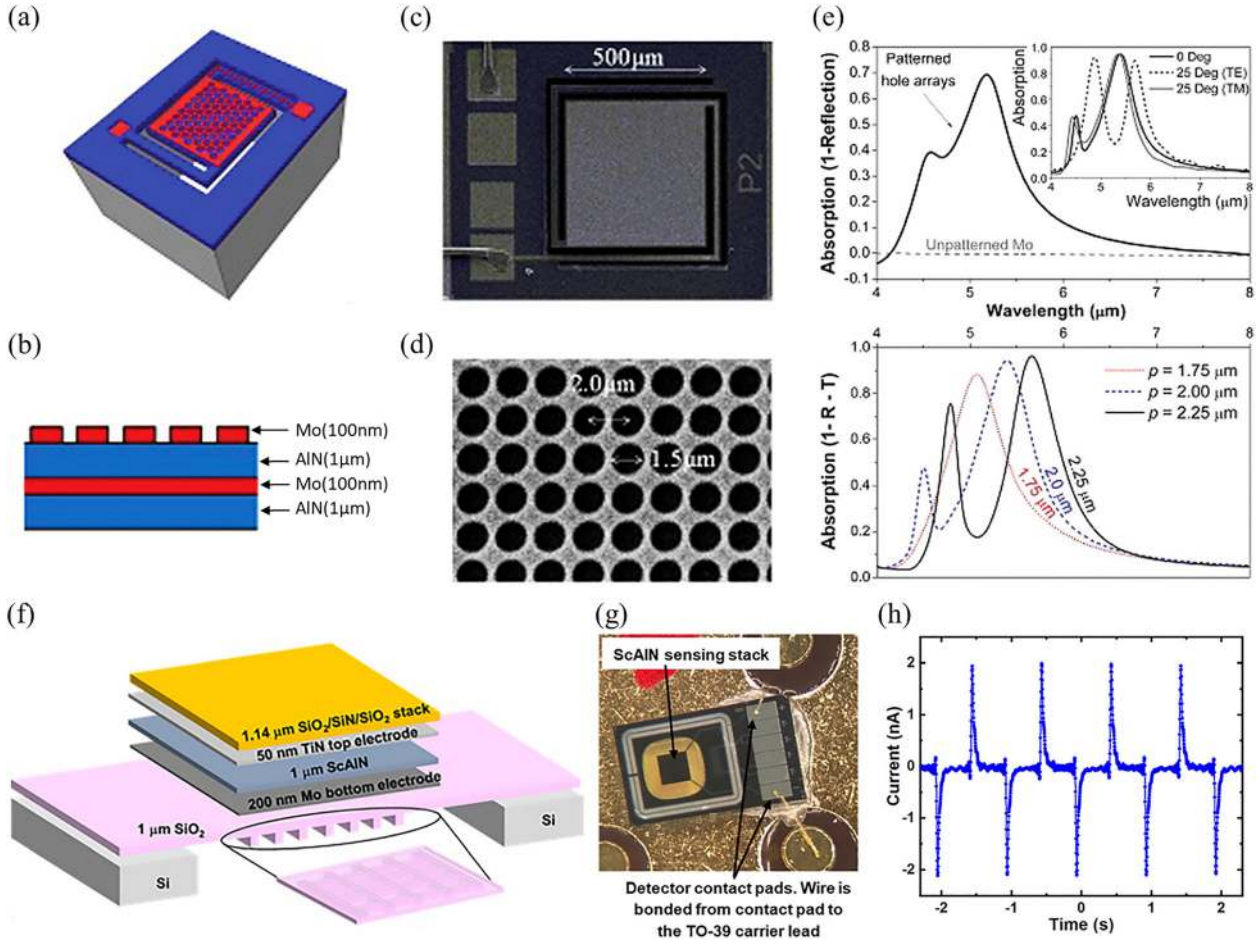

Figure 7: AlN-based pyroelectric photodetector.
(a) and (b): Schematic and cross-section of the wavelength-selective pyroelectric sensor. (c) and (d): SEM images of the fabricated sensor and the patterned top Mo layer with hole array. (e) Top panel: measured absorption spectra of detectors with top Mo layer patterned (black solid line) and unpatterned (gray dashed line). Inset: FDTD simulated absorption spectra for TE and TM polarizations at 0° incident angle (black solid line) and 25° incident angle (TE: gray dashed line; TM: gray solid line). Bottom panel: simulated absorption spectra with hole dimension variation, indicating the absorption peak can be engineered by adjusting the hole array dimension. (a)–(e) Adapted from [71], with the permission of AIP Publishing. (f) Schematic of ScAlN-based pyroelectric photodetector, showing each layer and the respective layer thickness. Magnified schematic of SiO_2 rib array is included. It is designed to increase the mechanical stiffness of the device. (g) Microscopic image of the fabricated device wire bonded on a TO-39 header, with membrane sensing area and contact pads marked out. (h) Time domain response from the pyroelectric photodetector illuminated by commercial MEMS thermal emitter under 1 Hz square wave driving voltage. The response amplitude is measured to be around 2 nA. (f)–(h) Adapted from [66], with the permission of AIP Publishing.

been demonstrated including metalens [153–155], color filters [156–158], beam deflectors [159–161], waveplates [162–164], and holograms [165–167]. Also, metasurface can be patterned in large-area, and mass-produced on CMOS-compatible fabrication facilities [168–170], which brings down the manufacturing cost. The fabrication process is also compatible with the one used for traditional in-plane photonics platform. As mentioned earlier, among the materials available in CMOS-compatible fabrication line, AlN has advantage of large bandgap (6.2 eV at room temperature [52, 53]) and relatively high refractive index (2.2 @ 375 nm [171]) compared with SiO_2 cladding. Furthermore, the low thermo-optic coefficient of AlN (4.26×10^{-5}/K at the wavelength of 1000 nm [78]) contributes to high power handling capability. Hence, AlN is a very suitable material for metasurface, especially in UV wavelength regime where most semiconductor materials have absorption. Recently, the designs of AlN-based metasurface, including metalens and holography, have been reported in the studies by Gao et al. and Guo et al. [171, 172]. The experimental demonstration of AlN metalens working at UV wavelength has also been reported in the study by Hu et al. [88]. The schematic of 3D on-axis focusing by metasurface in transmission mode is illustrated in Figure 8(a). The working

wavelength (λ) of the device is 375 nm. Figure 8(b) shows the simulation model, with scale bar length of 1.6 μm. The metalens has ripple-like patterns, with designed numerical aperture (NA) of 0.88 and focus length (f) of 2 μm. The phase distribution of scattered light follows the hyperboloidal profile. Laser writing is used to pattern the resist after AlN deposition with a sputtering system. The fabricated AlN metasurface on sapphire substrate is illustrated in Figure 8(c), with scale bar length of 60 μm. The device has an NA of 0.08 and f of 2 mm. The simulated and measured beam intensity profile at the focal plane are shown in Figure 8(d) and Figure 8(e), respectively. At the focal plane, the simulated beam intensity along the x-axis is illustrated in Figure 8(f), showing full-width-half-maximum (FWHM) of 232 nm, which is close to diffraction limit of 212 nm (λ/2NA ~ 212 nm). While the measured FWHM along x-axis is 6.7 μm, as shown in Figure 8(g). This is wider than diffraction limit of 2.3 μm (λ/2NA ~ 2.3 μm), contributed by the fabrication inaccuracy and also the low NA of the fabricated device. Furthermore, the 3D routing of UV light has been demonstrated by focusing the light in two different planes, with schematic shown in Figure 8(h). For simulation, the location of plane I and plane II are at z = 3 and 7 μm, respectively. While for real fabricated device, these locations are at z = 2 and 5 mm. The designed and fabricated metasurface devices are illustrated in Figure 8(i) and Figure 8(j), respectively. The simulated intensity profile at plane I (z = 3 μm) and II (z = 7 μm) are shown in Figure 8(k) and Figure 8(m), with FWHM of 336 and 266 nm, respectively. The experimental intensity distribution measured at plane I (z = 2 mm) and II (z = 5 mm) are illustrated in Figure 8(l) and Figure 8(n), with FWHM of 20 and 36 μm, respectively.

3.5 Optical modulator based on Pockels effect

Optical modulator is an essential building block in photonic integrated circuit. The phase shifting requires

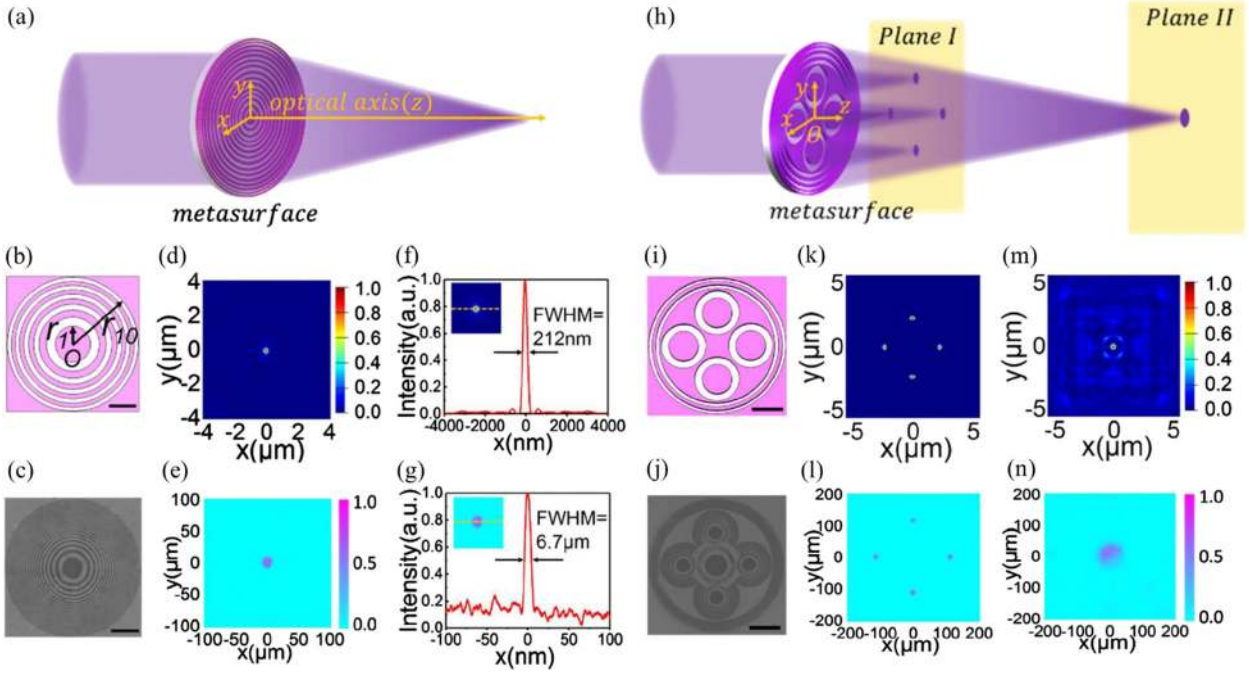

Figure 8: AlN-based metasurface devices working at UV wavelength (λ = 375 nm).
(a) Schematic of AlN-based metalens focusing in transmission mode. (b) Metalens simulation model, with ripple-like AlN pattern on sapphire substrate, and scale bar length of 1.6 μm. (c) Optical image of fabricated metalens sample, with scale bar length of 60 μm. (d) Simulated intensity distribution at the focal plane. (e) Measured intensity distribution at the focal plane. (f) Simulated intensity profile at focal place along x-axis, with FWHM of 212 nm. (g) Measured intensity profile at focal place along x-axis, with FWHM of 6.7 μm. (h) Schematic of AlN-based 3D routing in transmission mode, which is able to focus incident light into two different focal planes. (i) Simulation model of 3D router, with scale bar length of 1.7 μm. (j) Fabricated metasurface for 3D routing, with scale bar length of 90 μm. (k) and (m): Simulated light intensity distribution after normalization at focal plane I (z = 3 μm) and focal plane II (z = 7 μm), with FWHM of 336 and 266 nm at focal spot, respectively. (l) and (n): Measured light intensity distribution after normalization at focal plane I (z = 2 mm) and focal plane II (z = 5 mm), with FWHM of 20 and 36 μm at focal spot, respectively. (a)–(n) Adapted with permission from [88] © The Optical Society.

Table 4: Summary of AlN-based $\chi^{(2)}$ nonlinear optical devices.

Wavelength	Structure	AlN fabrication technique	Cavity *Q*	Mechanism	On-chip pump power	Reference/ year
1550 and 700 nm	Microring resonator	Magnetron reactive sputtering	6×10^5 @ 1555 nm	Electro-optic (Pockels) effect	N.A.	[91]/2012
1550 nm	Mach–Zehnder interferometer (MZI) and microring resonator	Magnetron reactive sputtering	1.1×10^4 (for ring)	Electro-optic (Pockels) effect	N.A.	[92]/2016
1550 nm	MZI and microring resonator	Magnetron reactive sputtering	~8×10^4 (for ring) limited by electrode-induced loss	Electro-optic (Pockels) effect	N.A.	[75]/2019
1550 → 775 nm	Waveguide and microring resonator	Magnetron reactive sputtering	2.0×10^5@ 1550 nm (microring)	SHG	22 mW	[54]/2012
1544 → 772 nm	Microring resonator	Magnetron reactive sputtering	2.3×10^5@ 1544 nm 1.16×10^5@ 772 nm	SHG	0.1–27 mW	[94]/2016
612 → 306 nm 662 → 331 nm 712 → 356 nm	Waveguide	MOCVD grown on sapphire substrate	N.A.	SHG	43 μW	[93]/2016
1556 → 778 nm	Microring resonator	Magnetron reactive sputtering	3.0×10^5@ IR	SHG	180 μW	[95]/2018
1550 → 775 nm	Microring resonator	Single crystalline AlN grown by epitaxy on sapphire substrate	5.9×10^5@ 1550 nm 2.5×10^5@ 775 nm	SHG	3.5 mW	[96]/2018
1556, 1538, 774 nm	Microring resonator	N.A.	1.8×10^5@ 1556 nm 2.6×10^5@ 1538 nm 1.1×10^5@ 774 nm	Three wave mixing (TWM)	Up to 83.7 mW drive power at telecom wavelength	[128]/2016
775 → 1544, 1556 nm	Microring resonator	Magnetron reactive sputtering	1.1×10^5@ visible 2×10^5@ IR	Parametric down-conversion	1.9 mW	[98]/2017
Pump 779 nm Signal: 1460–1550 nm; Idler: 1560–1650 nm	Microring resonator	Single crystalline AlN grown by epitaxy on sapphire	2×10^5@ visible 6×10^5@ IR	OPO	12–70 mW	[129]/2019
Comb lines around 1550 nm → comb lines around 775 nm	Microring resonator	Magnetron reactive sputtering	N.A.	SHG, SFG	N.A. (100 mW comb line power after amplification)	[97]/2016
765–795 nm 1480–1680 nm	Microring resonator	Single crystalline AlN grown by epitaxy on sapphire	2×10^5@ visible 6×10^5@ IR	SHG, OPO	80 mW for pump @ visible	[130]/2020

electrical tuning of waveguide refractive index. Contributed by low optical loss, wide transparency window, and noncentrosymmetric crystalline structure, AlN-based optical modulators have been designed and demonstrated [91, 92, 173]. Compared with the phase shifting using thermal-optic effect, the electro-optic (Pockels) effect has the advantage of low power consumption and fast tuning speed. A recently demonstrated AlN-based optical modulator design is illustrated in Figure 9(a) [91]. The top and bottom panel shows the optical and electrical field distribution at the cross-section, respectively. The plasma-enhanced chemical vapor deposition (PECVD) SiO_2 thickness (t_{ox}) has been optimized to be 0.8 μm to balance the trade-off between the electro-optic overlap integral and optical absorption due to electrodes (<1 dB/cm). The microscopic image of the fabricated AlN microring with metal contacts is shown in Figure 9(b) left panel. Two vertical couplers at the bottom are used to couple light in and out of the device. The wavelength shifts of 8 pm due to the Pockels effect is shown in Figure 9(b) right panel. The functionality of the modulator in a communication system has been demonstrated. The modulation speed of 4.5 Gbps at 1550 nm has been achieved, through the clear eye pattern as shown in Figure 9(c). In order to increase the electro-optic overlap, in the study by Zhu et al. [92], the electrodes are placed at the top and the bottom of the AlN waveguide, as shown in Figure 9(d). In this way, the maximum electric field created by the voltages applied on electrodes can go through the AlN waveguide. Compared with the earlier modulator design shown in Figure 9(a), the design in Figure 9(d) not only provides increased electro-optic overlap, but also can be fabricated by the standard planar CMOS-compatible fabrication process, and hence enables the integration of multiple layers on Si. The numerically calculated optical mode (TE) within the fabricated waveguide and the microscopic images of the fabricated microring and Mach–Zehnder interferometer (MZI)-based modulator are illustrated in Figure 9(e). The TE resonance shift of the microring and MZI modulator are shown in Figure 9(f) left and right panel, respectively. The MHz-level modulation frequency of the MZI is illustrated through the time-domain response of the signal shown in Figure 9(g). The modulation speed is limited by the speed of the voltage supplier. Much higher modulation speed is expected to be demonstrated, contributed by the high-speed of the electro-optic effect. Furthermore, in a follow-up work by the same group, a push-pull structure is implemented to reduce the V_π of the MZI modulator by half [75]. The schematic cross section and the cross-sectional TEM image of the push-pull modulator are illustrated in Figure 9(h) left and right panel, respectively. The optical spectra and the phase shift with respect to applied voltage are shown in Figure 9(i) left and right panel, respectively. V_π of 21 V has been achieved by the modulator working at the wavelength of 1550 nm.

3.6 Second harmonic generation

As mentioned in Optical property subsection, for nonlinear process at telecom wavelength, AlN is free of two photon absorption and related free carrier refraction, while it happens in Si. Also, AlN thin film has been reported for significant second order nonlinear effect on either sapphire or Si substrate [174–176]. After the patterning of the thin film to form the waveguide, the phase matched AlN waveguides and microring resonators have been demonstrated for efficient SHG [54, 93]. In a waveguide, the phase matching condition for SHG requires the following:

$$\Delta k = k(\omega_2) - 2k(\omega_1) = \omega_2 n_{\text{neff}\,2} - 2\omega_1 n_{\text{neff}\,1} = 0 \qquad (1)$$

where $n_{\text{neff}\,1}$ and $n_{\text{neff}\,2}$ represent the effective refractive index of the pump mode and SH mode within the waveguide, respectively. Considering SHG case, $\omega_2 = 2\omega_1$, which implies that $n_{\text{neff}\,2} = n_{\text{neff}\,1}$. Figure 10(a) shows the calculated dispersion relations of waveguides. For a fixed waveguide height, as the waveguide width increases, the effective index of the fundamental mode at 1550 nm increases slower than the higher-order modes at SH wavelength 775 nm. By making use of this property, the phase matching condition can be fulfilled at the cross-over point of dispersion curves at pump and SH wavelengths. Figure 10(a) bottom part illustrates the phase-matched optical modes, which are fundamental mode at 1550 nm, and fifth-order mode at 775 nm. Based on the phase matching condition mentioned earlier, sputtered polycrystal AlN waveguide has been fabricated, with optical image shown in Figure 10(b). The SHG output port is connected to an optical spectrum analyzer (OSA) working at visible wavelength range. Figure 10(c) shows the captured SHG spectra with different waveguide width, in which the increase of phase-matched wavelength can be observed as the waveguide width becomes larger.

In a follow-up work published in 2016, an optimized polycrystalline AlN microring cavity has been demonstrated with SHG efficiency of 2500%/W in the study by Guo et al. [94]. Perfect phase-matching condition is fulfilled through thermal tuning of the cavity. The SHG experimental setup is illustrated in Figure 10(d). Off-chip wavelength division multiplexers (WDM) are used to split/combine the pump signal at IR and SHG signal at visible wavelengths. On the chip, two sets of waveguides are used

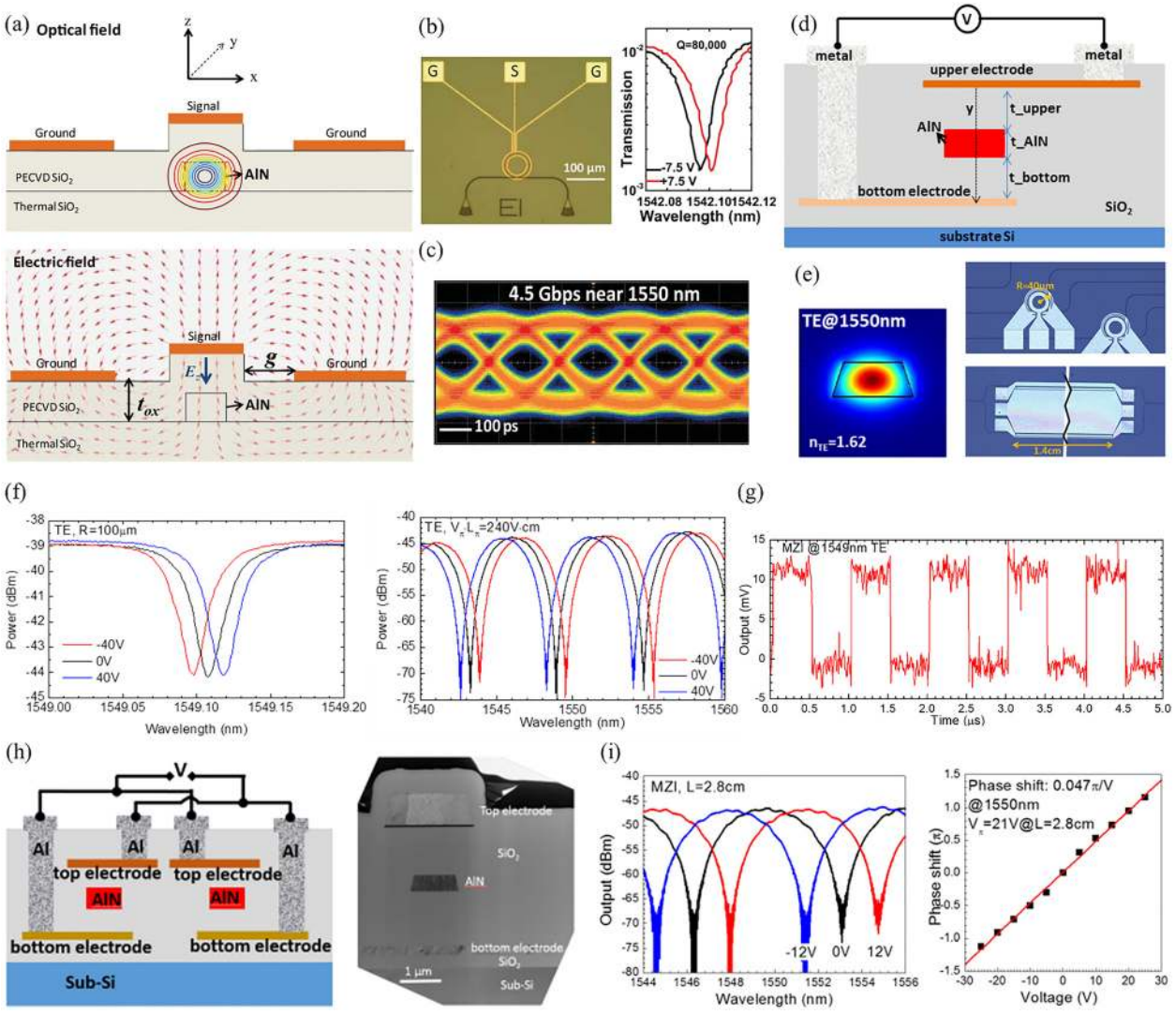

Figure 9: AlN-based integrated optical modulator using Pockels effect.
(a) Top panel: simulated optical field intensity distribution (TE mode) in designed AlN waveguide at telecom wavelength. Bottom panel: simulated electrical field distribution at the cross section of designed modulator. (b) Left panel: microscopic image of the fabricated AlN microring with metal contacts and vertical couplers for light coupling onto and out of the device. Right panel: optical resonance around 1542 nm with Q value of 8×10^4, showing wavelength shifts by 8 pm induced by applying bias voltage from −7.5 V to +7.5 V. (c) Clear eye pattern generated using the optical modulator under modulation speed of 4.5 Gbps at 1550 nm. (a)–(c) Adapted with permission from [91], copyright (2012) American Chemical Society. (d) Schematic of AlN-based phase shifter cross section for optical modulator. (e) Left panel: simulated TE mode profile at 1550 nm. Right top and bottom panel: optical images of fabricated modulator with microring and MZI structure, respectively. (f) Left and right panel: transmission spectra of microring-based and MZI-based modulator (TE mode), respectively. (g) MZI modulator output waveform at 1549 nm TE mode. (d)–(g) Adapted with permission from [92] © The Optical Society. (h) Left panel: schematic of AlN-based phase shifter cross section with push-pull structure. Right panel: cross-sectional TEM image of one arm in MZI optical modulator. (i) Left panel: optical spectra under different bias voltages on MZI modulator. Right panel: phase shift with respect to voltage at 1550 nm. (h) and (i) Adapted with permission from [75] © The Optical Society.

to couple light into and out of the microring cavity separately. The cavity transmission spectrum for the pump wavelength and SHG wavelength are shown in Figure 10(e) left and right panel, respectively. In order to optimize the cavity to achieve efficient SHG, different approaches have been implemented. Firstly, to achieve high nonlinear coupling strength, fundamental transverse magnetic (TM_0) mode has been chosen at pump wavelength, and TM_2 mode has been chosen for SHG signal. The phase-matched mode intensity profiles are provided in Figure 10(e) inset. The

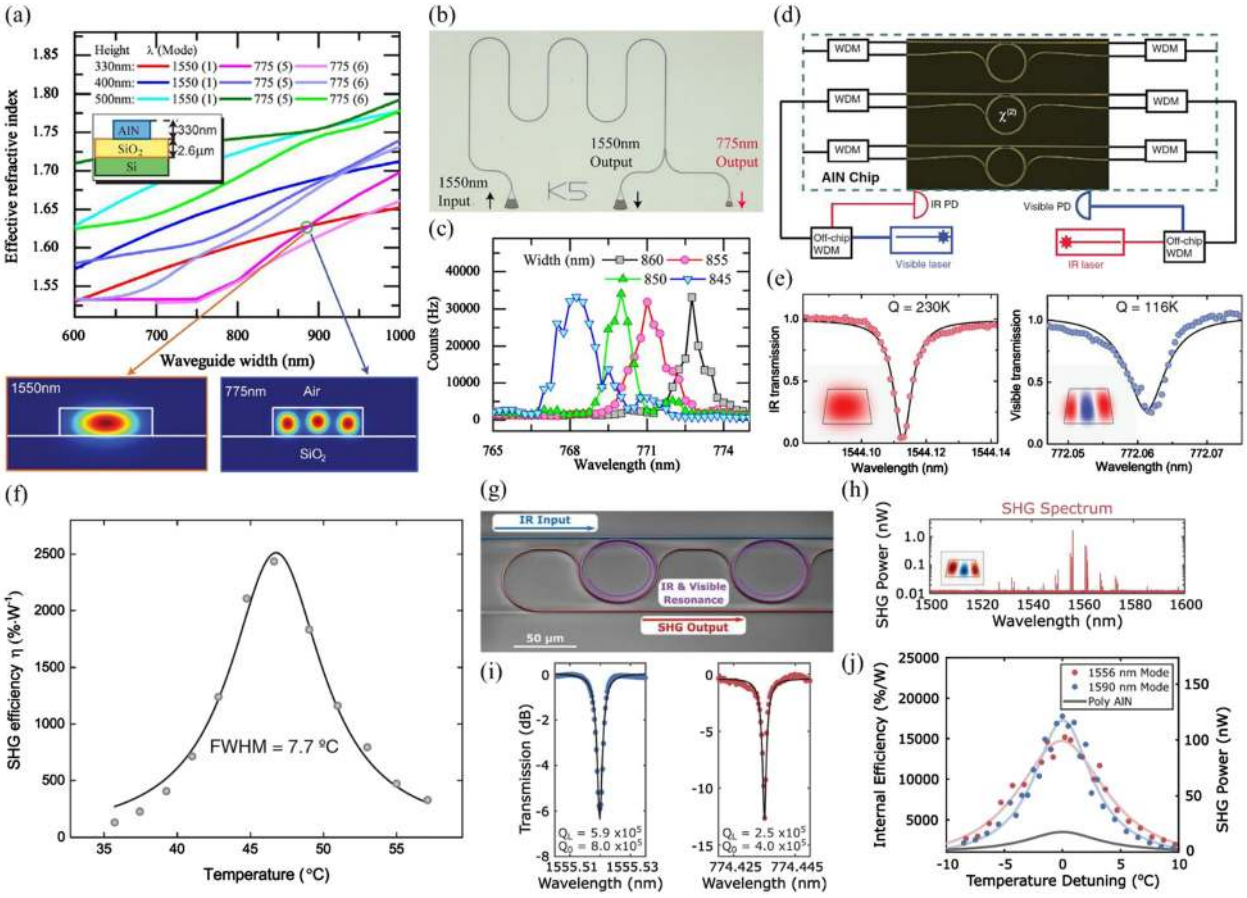

Figure 10: AlN-based integrated devices for second harmonic generation (SHG).
(a) Calculated waveguide dispersion relation between the fundamental mode at 1550 nm and higher order modes at 775 nm. Phase matched condition can be fulfilled at the cross-over point between the dispersion curves at pump (1550 nm) and SHG wavelengths (775 nm), with mode profiles included at the bottom. (b) Optical image of fabricated waveguide for SHG. (c) Optical spectra of SHG signal under different waveguide width. (a)–(c) Adapted from [54], with the permission of AIP Publishing. (d) SHG experimental setup: off-chip wavelength division multiplexers (WDM) are used to split/combine the pump signal at IR wavelength and SHG signal at visible wavelength. Two sets of waveguides are used to couple light into and out of the microring cavity separately, so that the critical coupling can be achieved for both wavelengths simultaneously. (e) Left and right panel: cavity transmission spectrum for the pump wavelength and SHG wavelength, with loaded Q of 2.3×10^5 and 1.16×10^5, respectively. TM_0 mode for pump and TM_2 mode for SHG signal are included as insets. (f) SHG efficiency with respect to device temperature, with optimized efficiency of 2500%/W achieved around 46 °C. (d)–(f) Adapted with permission from [94] © The Optical Society. (g) SEM image of fabricated AlN SHG device without top cladding layer. Pump light is coupled into the cascaded microring cavities through straight bus waveguide at top marked in blue. Within the microring cavity marked in purple, the phase-matching condition is achieved between the $TM_{0,0}$ mode at pump wavelength in IR, and $TM_{2,0}$ mode at SHG signal in near-visible wavelength. The wrap around waveguide marked in red couples the SHG signal in near-visible wavelength out from the microring and is connected to the on-chip WDM. (h) SHG spectrum captured at the output port after cascaded microrings. (i) Resonance spectra at pump (left panel) and SHG signal (right panel). The loaded Q factor for pump and SHG mode can be obtained as 5.9×10^5 and 2.5×10^5, respectively. (j) SHG efficiency and power with respect to chip temperature detuning for pump mode at 1590 nm (blue) and 1560 nm (red). Maximum SHG efficiency can reach 17,000%/W for 1590 nm pump mode. The simulated data for polycrystalline-based AlN SHG device has also been plotted for comparison. (g)–(j) are from [96], with the permission of AIP Publishing.

microring diameter has also been optimized to balance the trade-off between the high nonlinear coupling strength and cavity Q. Secondly, the intrinsic Q factor of the microring has been improved by using relatively thick AlN film (1 μm). Also, thermal annealing process has been applied to reduce the loss in AlN and SiO_2 cladding. Extracted from the loaded Q factor from Figure 10(e), the intrinsic Q are obtained as 4.6×10^5 for pump, and 1.5×10^5 for SHG signal. Thirdly, the coupling condition has been optimized to simultaneously achieve critical coupling by using two separate bus waveguides for pump and SHG signal. This is required to maximize the SHG generation

efficiency. Lastly, thermal tuning has been applied to fine tune the microring resonator so that the perfect phase matching condition ($\omega_2 = 2\omega_1$) can be reached for the resonance modes at pump and SHG wavelengths. The maximum SHG efficiency with respect to temperature is shown in Figure 10(f), with optimized efficiency reported to be 2500%/W. Such temperature-dependent SHG efficiency is contributed by the fact that the resonance modes of pump and SHG signal have different thermal shifting speed. The optimized SHG efficiency occurs at ~46 °C when wavelength mismatch is offset to 0. Furthermore, on the same polycrystalline AlN nonlinear photonics platform, highly efficient SHG can be achieved at a specific working wavelength, after systematic optimization of the waveguide geometry and chip temperature [95].

Although polycrystalline AlN-based SHG microring cavity has been optimized as discussed earlier, the SHG efficiency is ultimately limited by the intrinsic cavity Q and waveguide loss. Single-crystalline high quality AlN epitaxial grown on sapphire substrate has demonstrated ring cavity with Q factor on the order of 10^6 in the study by Liu et al. [137], which is higher than the ones observed in polycrystalline AlN-based cavity [82, 94]. In 2018, single-crystalline AlN-based SHG device has been demonstrated with a remarkably high efficiency up to 17,000%/W in the study by Bruch et al. [96]. Figure 10(g) shows SEM image of the fabricated AlN SHG device without top cladding layer. The pump light is coupled into the cascaded microring cavities through straight bus waveguide at top marked in blue. Within the microring cavity marked in purple, the phase-matching condition is achieved between the $TM_{0,0}$ mode at pump wavelength in IR, and $TM_{2,0}$ mode at SHG signal in near-visible wavelength range. The wrap around waveguide marked in red couples the SHG signal in near-visible wavelength out from the microring and is connected to the on-chip WDM. The SHG spectrum captured at the output port after cascaded microrings is presented in Figure 10(h), with inset showing the $TM_{2,0}$ mode at SHG signal wavelength. The resonance spectra at pump and SHG signal is illustrated in Figure 10(i) left and right panel, respectively. The loaded Q factor for pump and SHG mode can be obtained as 5.9×10^5 and 2.5×10^5, respectively. This is more than two times as the Q factors obtained from Figure 10(e) based on polycrystalline AlN. Similar to the chip temperature optimization reported in the study by Guo et al. [94] and illustrated in Figure 10(f), the chip temperature has been optimized to achieve perfect phase matching, with results shown in Figure 10(j). The maximum SHG efficiency is reported to be 17,000%/W for 1590 nm pump mode, which is around 7-fold as earlier report based on polycrystalline AlN.

3.7 $\chi^{(2)}$-based optical parametric generation, amplification and oscillation

Beyond SHG, other three wave mixing (TWM) processes generated through $\chi^{(2)}$ nonlinear effect have also been demonstrated on the same AlN platform in the study by Guo et al. [128]. The fabricated microring with bus waveguides for coupling (without cladding) is illustrated in Figure 11(a). Similar to the SHG work discussed earlier [94], the TM_0 mode in telecom band and TM_2 mode in visible band are chosen for phase-matching condition, with mode profile included in the inset of the figures. Two bus waveguides at two sides of the microring are used to couple telecom and visible light separately. The measured transmission spectra of three waves together with schematic of three frequencies are illustrated in Figure 11(b). The loaded Q of three resonance modes are marked at the top of each corresponding spectrum. The experimental setup for the strong coupling due to $\chi^{(2)}$ nonlinear effect is illustrated in Figure 11(c). The telecom drive signal at 1556 nm (ω_a) is coupled onto the chip after erbium-doped-fiber amplifier (EDFA) to excite the microring cavity mode in counter-clockwise (CCW) direction. At the same time, a visible laser at 773 nm (ω_b) probes the mode in either clock-wise (CW) or CCW direction, through a switch. A spectrum analyzer is placed after visible photodetector. Figure 11(d) shows the captured spectrum of visible mode in CW and CCW direction. Mode splitting can be observed when the visible signal is propagating in CCW, which is the same direction as telecom drive laser signal. Such mode splitting is contributed by the destructive interference between original probe signal and the one converted back from telecom wavelength, which are generated through the scattering of visible photons by drive signal photons. In comparison, there is no mode splitting when the visible signal is propagating in CW direction, which is the opposite direction as the drive signal. The insets in Figure 11(d) clearly illustrate the nonreciprocal property of this nonlinear optical process within the microring cavity.

Furthermore, by using similar AlN-based microring configuration and phase matching condition, parametric down-conversion photon-pair source has been demonstrated in the study by Guo et al. [98]. The optical spectra of DFG under different IR pump wavelengths are illustrated in Figure 11(e) top panel. Superconducting single-photon detectors are used to characterize the statistical properties of photons generated by the microring cavity, with results shown in Figure 11(e) bottom panel. The photon flux at different microring resonances are obtained and plotted,

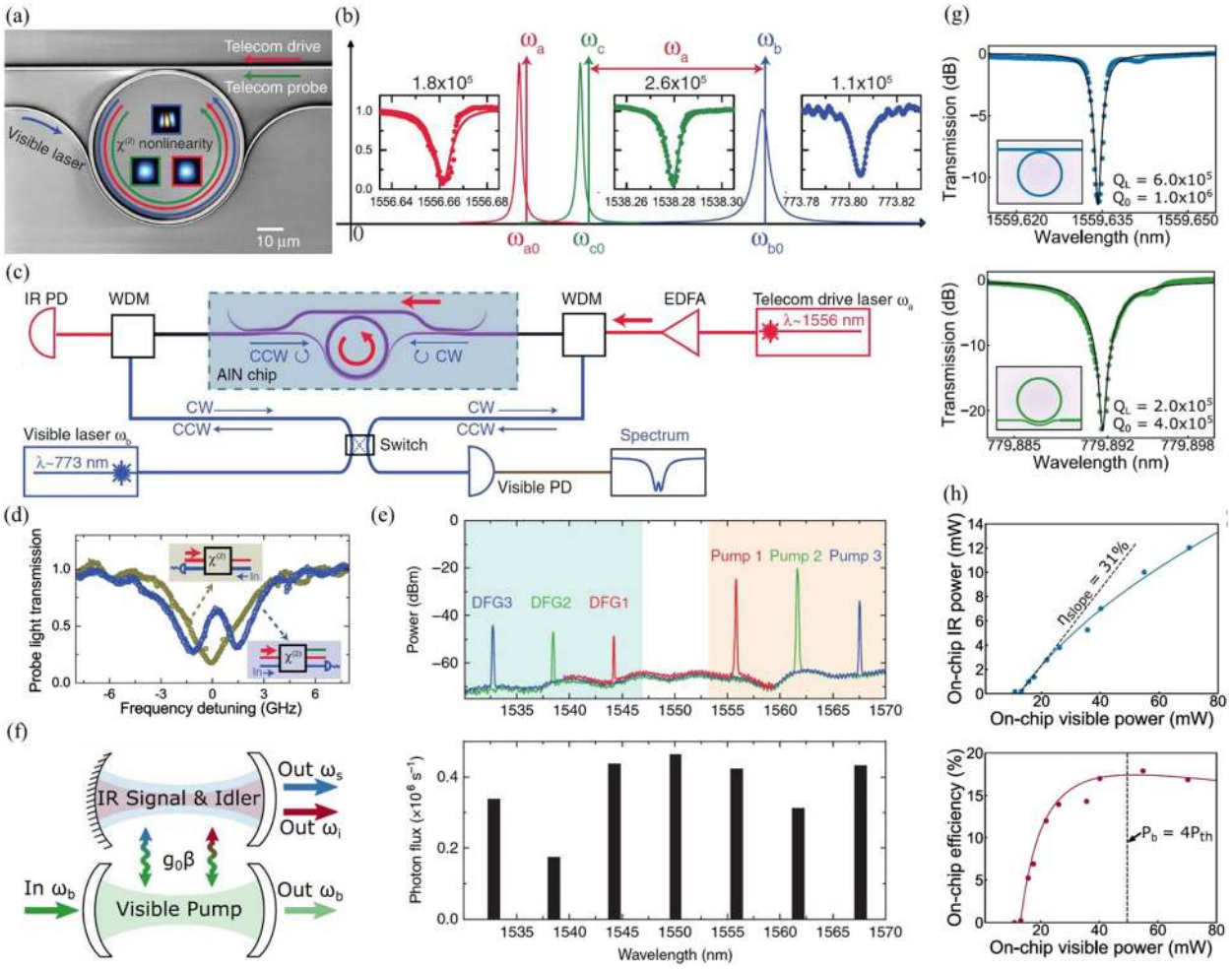

Figure 11: AlN-based integrated devices for three wave mixing (TWM), parametric down conversion, and optical parametric oscillator (OPO). (a) SEM image of AlN microring resonator (without top cladding) for TWM. (b) Schematic of optical resonance modes with transmission spectra. Loaded Q of each mode is marked at top. (c) TWM experimental setup: telecom drive signal at 1556 nm (ω_a) cascaded with EDFA to excite cavity mode in CCW direction. A visible laser at 773 nm (ω_b) probes the mode in either CW or CCW direction, through a switch. Spectrum analyzer is placed after visible photodetector (PD). (d) Captured spectrum of visible mode in CW and CCW direction. Mode splitting can be observed when the visible signal is propagating in CCW, which is the same direction as telecom drive laser signal. Insets illustrate the nonreciprocal property of this nonlinear optical process within the cavity. (a)–(d) Adapted with permission from [128], copyright (2016) by the American Physical Society. (e) Top: optical spectra of DFG under different IR pump wavelengths. Bottom: photon flux at different microring resonances, including both nondegenerate and degenerate down conversion. The variation of photon flux at different modes is contributed by the difference in cavity Q. The photon counts are calibrated by the wavelength-dependent detection efficiency of PD. (e) is adapted with permission from [98]. Licensed under a Creative Commons Attribution. (f) Schematic showing mechanism of OPO process. It consists two coupled cavities, one for pump (ω_b) at visible, the other for signal (ω_s) and idler (ω_i) at IR, which are coupled through $\chi^{(2)}$ nonlinear effect with strength $g_0\beta$. (g) Top and bottom: measured transmission spectra at IR and visible wavelengths, respectively. Loaded Q and intrinsic Q of the cavity for IR and visible wavelength are also included. (h) Power (top panel) and efficiency (bottom panel) with respect to on-chip visible power for degenerate OPO process. A high slope efficiency of 31% has been obtained after linear fitting of on-chip IR power with respect to on-chip visible power. A maximum OPO efficiency of 17% is achieved in bottom panel, which is close to half of slope efficiency of 31% obtained in top panel. Dashed line in bottom panel indicates the on-chip visible power for maximum on-chip efficiency theoretically. (f)–(h) Adapted with permission from [129] © The Optical Society.

including both nondegenerate and degenerate down conversion. The variation of photon flux at different modes is contributed by the difference in cavity Q within the microring. The further characterization on heralded signal-signal correlation function shows the potential of the integrated down-conversion source for quantum information processing.

Optical parametric oscillator (OPO), which is based on $\chi^{(2)}$ nonlinear effect, has been widely applied as a tunable, coherent and narrow linewidth light source, to further

extend the optical wavelength to longer range. In 2019, AlN-based microring working as an OPO light source has also been demonstrated in the study by Bruch et al. [129]. The mechanism of the OPO system is illustrated in Figure 11(f). The OPO process can be considered as two coupled cavities, one for pump (ω_b) at visible wavelength, the other for signal (ω_s) and idler (ω_i) at IR wavelength. They are coupled through $\chi^{(2)}$ nonlinear effect. For the degenerate OPO process ($\omega_s = \omega_i = \omega_b/2$), a single frequency will be generated at IR wavelength, which is the reverse process of SHG. Under nondegenerate OPO condition ($\omega_s \neq \omega_i$), signal and idler will be located at two different resonance wavelengths. Single-crystalline AlN has been used for high optical Q factor. The loaded Q of the cavity for IR and visible are measured to be 6.0×10^5 and 2.0×10^5, respectively. The transmission spectra at these two wavelengths are shown in Figure 11(g) top and bottom panel, respectively. The power and efficiency of degenerate OPO process have been characterized, with results shown in Figure 11(h). The top panel shows the on-chip IR power with respect to on-chip visible pump power. A high slope efficiency of 31% has been obtained after linear fitting. The bottom panel shows the on-chip OPO process conversion efficiency with respect to on-chip visible power, with theoretical fitting plotted as solid line. A maximum efficiency of 17% is achieved, which is close to half of slope efficiency of 31% obtained in top panel.

Additionally, one more point worth mentioning is that the $\chi^{(2)}$ nonlinear effect within the AlN-based microring structure has been used for optical frequency comb generation [97, 130]. In the study by Jung et al. [97], the frequency doubling of external comb source has been achieved through the combination of SHG and SFG processes. The phase coherence is also confirmed by the interference between the generated frequency comb lines. In the meanwhile, in the study by Bruch et al. [130], the Pockels soliton microcomb driven by TWM in AlN microring has been reported. The degenerate OPO, pumped at 780 nm, is used to generate quadratic solitons in IR around 1560 nm. Compared with the Kerr soliton, the Pockels soliton has the advantages of lower generation threshold and higher pump-to-soliton conversion efficiency.

3.8 Third harmonic generation and optical Kerr parametric oscillation

In the earlier three Subsections 3.5–3.7, the discussions are focused on the $\chi^{(2)}$ nonlinear effect-based AlN devices. Actually, AlN does not only have significant $\chi^{(2)}$ nonlinear effect, but also has $\chi^{(3)}$ nonlinear effects, such as Kerr effect and Raman effect. Hence, in this subsection, we will present a review on the THG and optical Kerr parametric oscillation using AlN-based optical devices.

In the study by Surya et al. [131], an efficient THG device has been realized in AlN/Si_3N_4 composite microring resonator. The schematic of waveguide cross section is illustrated in Figure 12(a). Si_3N_4 is deposited via low pressure chemical vapor deposition (LPCVD), and AlN layer is deposited on Si_3N_4 via sputtering process. The co-integration of AlN and Si_3N_4 produces a degree of freedom for tuning to achieve the phase matching and mode overlap, and hence enables more efficient THG process. The calculated effective index with respect to microring width for phase matching are illustrated in Figure 12(b), in which the solid line represents the fundamental TE mode at pump wavelength around 1550 nm, and dotted lines represent the higher-order TM modes at THG wavelength. The crossing points represent phase-matching condition. The mode overlap at each crossing point, from i to viii, are also calculated. The maximum mode overlap is found under microring width between 1.68 and 1.86 μm. The optical image of the microring under THG operation is shown in Figure 12(c) top panel, where the green color THG signal can be clearly observed. The SEM image of the waveguide without cladding is illustrated in Figure 12(c) bottom panel. Considering the couplings between the bus waveguide and microring have significant difference at pump and THG wavelength, a wrap-around waveguide at the bottom is used for the coupling of THG signal, and the straight bus waveguide at the top is used for pump coupling. Figure 12(d) shows the characterization setup: a tunable laser around 1550 nm is used as pump, WDMs are used to split the pump and THG signal, and an Andor Spectrograph is used to capture the scattered light above the device. The captured spectrograph illustrated in Figure 12(e) shows that there is signal at THG wavelength, but no signal at SHG wavelength. This spectrograph verifies that the green color is actually generated from THG rather than SHG cascaded by SFG process.

Further, in a very recent study by Tang et al. [177], Kerr-based OPO has been demonstrated in AlN microring resonator. A 1-μm-thick AlN layer is grown on sapphire substrate via MOCVD, and patterned by electron beam lithography. The SEM image of microring resonator (R = 50 μm) without top cladding is illustrated in Figure 12(f). The waveguide dimension is engineered to achieve phase-matching among pump, signal and idler mode, which are located within wavelength range from 1600 nm up to 2600 nm. The schematic of $\chi^{(3)}$-based OPO to generate signal and idler is shown in Figure 12(g). The captured spectra from experiment for waveguide width of 3.2 and

Table 5: Summary of AlN-based $\chi^{(3)}$ nonlinear optical devices.

Wavelength range	Structure	AlN fabrication technique	Cavity Q	Mechanism	On-chip pump power	Reference/ year
1543 → 514 nm	Microring resonator	Magnetron reactive sputtering	4×10^5 @ IR	THG	60 mW	[131]/2018
Pump: 1974 nm Signal: 1637 nm Idler: 2484 nm	Microring resonator	Epitaxial AlN on sapphire substrate via MOCVD	5.7×10^5 @ pump	$\chi^{(3)}$-based OPO	375 mW	[177]/2020
IR region (1450–1650 nm)	Microring resonator	Magnetron reactive sputtering, chip is annealed at 1000 °C for 30 h for high Q	8×10^5 (waveguide width: 3.5 μm); 6×10^5 (waveguide width: 2.5 μm)	Cascaded FWM	500 mW	[178]/2013
IR region (1450–1650 nm)	Microring resonator	Magnetron reactive sputtering	5×10^5	Cascaded FWM, Pockels effect for tuning	600 mW	[179]/2014
Green, red, IR region	Microring resonator	Magnetron reactive sputtering	5×10^5	Cascaded FWM, SFG, THG	600 mW in bus waveguide	[99]/2014
Pump: 1560 nm First Stokes: 1700–1800 nm Second Stokes: 1800–2000 nm	Microring resonator	Epitaxial AlN on sapphire substrate via MOCVD	1.2×10^6 @ pump	Lasing based on stimulated Raman scattering (SRS)	~790 mW for second Stokes, ~120 mW for first Stokes	[101]/2017
IR region (1075–2075 nm)	Microring resonator	Epitaxial AlN on sapphire substrate via MOCVD	1.1×10^6	Cascaded FWM, SRS	126–1000 mW	[70]/2018
1400–1700 nm	Microring resonator	Epitaxial AlN on sapphire substrate via MOCVD	6.5×10^5	Kerr soliton generation, cascaded FWM	620 mW	[180]/2018
1400–1700 nm 720–840 nm	Microring resonator	Epitaxial AlN on sapphire substrate via MOCVD	1.1×10^6 @ pump	Cascaded FWM, SHG, SFG	50–1000 mW	[132]/2018
IR region (1200–2000 nm)	Microring resonator	Magnetron reactive sputtering	5×10^5–1.0×10^6	Cascaded FWM, Stokes SRS, Anti-Stokes SRS	N.A.	[100]/2019
500–4000 nm	Straight waveguide	N.A. (polycrystalline AlN)	N.A.	Supercontinuum generation (SCG), SHG, THG, DFG	80 mW	[133]/2017
Near-visible (660–900 nm), UV (360–425 nm)	Straight waveguide	Epitaxial AlN on sapphire substrate via MOCVD	N.A.	SCG, SHG, SFG	19 mW	[73]/2019
490–1100 nm	Straight waveguide	Epitaxial AlN on sapphire substrate via MOCVD	N.A.	SCG [self-phase modulation (SPM), soliton fission, etc.], SHG	30 mW	[134]/2019
390–4200 nm	Straight waveguide	Epitaxial AlN on sapphire substrate via MOCVD	N.A.	SCG (SPM, soliton fission, etc.), SHG, THG	56 mW	[123]/2020

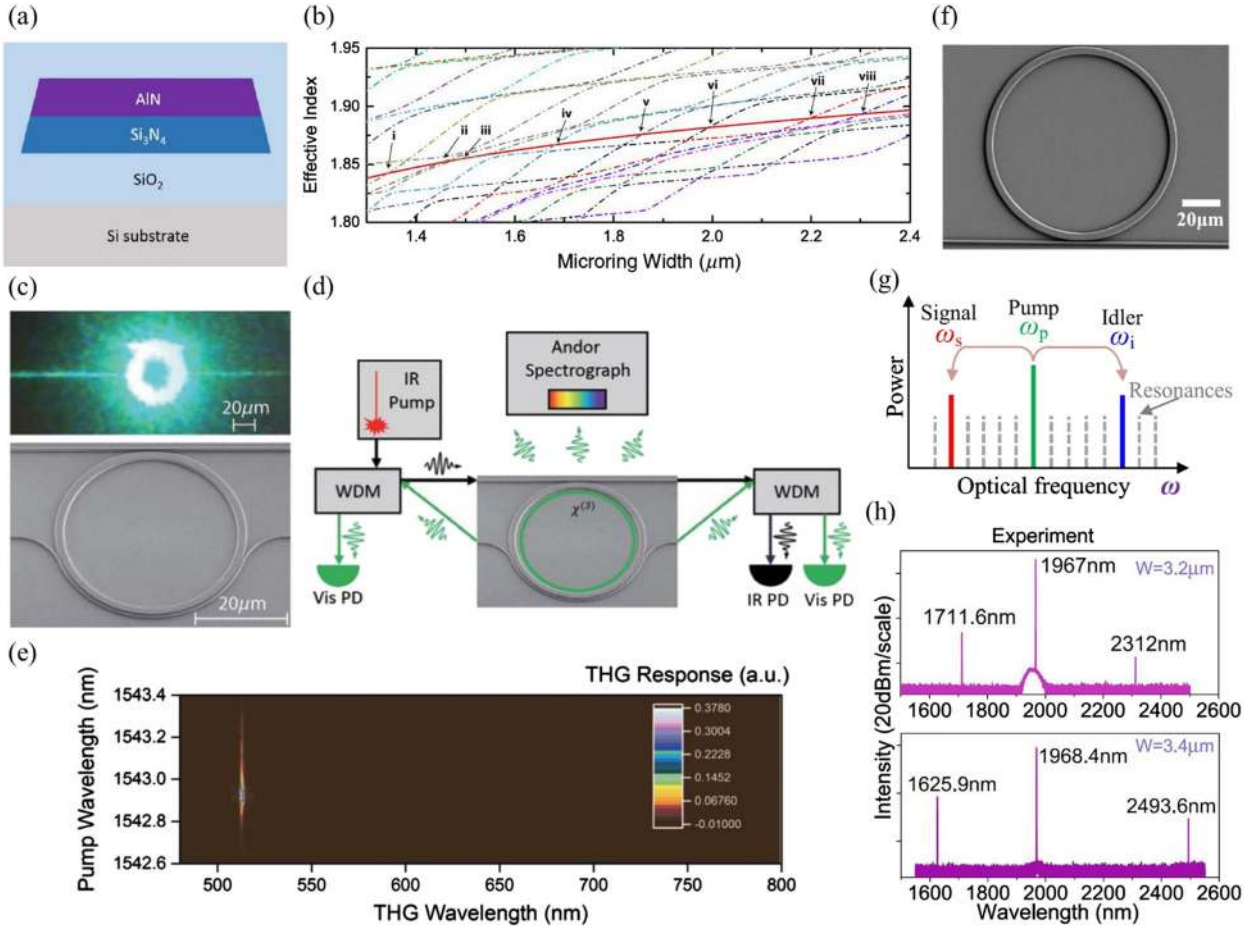

Figure 12: AlN-based integrated devices for third harmonic generation (THG) and optical Kerr parametric oscillation.
(a) Schematic of waveguide cross section for THG. (b) The calculated effective index with respect to microring width for phase matching. Solid line represents the fundamental TE mode at pump wavelength around 1550 nm, and dotted lines represent the higher-order TM modes at THG wavelength. The crossing points represent phase-matching condition. (c) Top panel: optical image of the microring under THG operation. The scattered green color THG signal can be observed. Bottom panel: SEM image of the waveguide without cladding. (d) THG characterization setup: a tunable laser around 1550 nm is used as pump, WDMs are used to split the pump and THG signal, and an Andor Spectrograph is used to capture the scattered light above the device. (e) Captured spectrograph shows that there is signal at THG wavelength, but no signal at SHG wavelength. (a)–(e) Adapted with permission from [131] © The Optical Society. (f) SEM image of microring resonator ($R = 50$ μm) without top cladding. (g) Schematic of $\chi^{(3)}$-based OPO to generate signal and idler from pump. (h) Captured spectra from experiment for waveguide width of 3.2 μm (top) and 3.4 μm (bottom). (f)–(h) Adapted with permission from [177] © The Optical Society.

3.4 μm are illustrated in Figure 12(h) top and bottom panel, respectively. Different phase matching conditions are achieved by tailoring the AlN waveguide width. With larger waveguide width, wider OPO span can be achieved. The fine tuning of the OPO sideband has also been achieved through pump wavelength adjustment and temperature control.

3.9 Optical Kerr comb generation

Optical frequency comb has applications in different areas, including precision measurement [181], spectroscopy [182], optical frequency synthesis [40, 42], distance measurement [7, 183], microwave photonics [184–186] and many other applications [187–189]. The nanophotonic-based integrated optical frequency comb enables it to be generated from a compact device, and hence has drawn a significant attention in research and development [74, 190–193]. Integrated optical frequency combs based on Kerr nonlinear effect have also been demonstrated on AlN platform, as summarized in Table 5.

Differentiating from the conventional way of using ultrashort optical pulse with high peak field intensity, the high field intensity is achieved through the field enhancement from a high Q ring resonator. Compared with Si_3N_4,

AlN has similar nonlinear index ($n_2 = 2.3 \times 10^{-15}$ cm^2/W at 1550 nm) [74], but high thermal conductivity of 285 W/(m·K) [67], which is 2 orders of magnitude larger than Si_3N_4, and hence improves the power handling capability of the cavity due to the enhanced thermal dissipation [178]. The first report of optical frequency comb generation through cascaded four-wave mixing (FWM) within AlN-based microring cavity was in 2013 in the study by Jung et al. [178]. The optical image, cross-SEM image of the fabricated microring are illustrated in Figure 13(a) top and bottom panel, respectively. The fabricated AlN microring cavity is on Si substrate, with SiO_2 as cladding layer. The AlN waveguide height is fixed at 650 nm, and width are varied in the simulation, as shown in the dispersion calculation in Figure 13(b). The dispersion relation of fundamental TE mode under different waveguide widths are calculated, which are contributed by both material dispersion and waveguide dispersion. The mode intensity profiles are illustrated in insets. The waveguide width of 3.5 μm is chosen for near-zero dispersion, for waveguide to satisfy phase-matching condition and to support multiple transverse modes around 1550 nm. The designed microring cavity device demonstrates frequency comb spanning from 1450 to 1650 nm, as shown in Figure 13(c). The resonance spectrum of the microring cavity is also illustrated in the inset, showing a loaded cavity Q of 6×10^5 for frequency comb generation. The free spectral range (FSR) of the frequency comb is measured to be 370 GHz, which corresponds to the FSR of fundamental mode. In the following year (2014), the electrical switchable optical frequency comb has been demonstrated by applying electric field across the AlN waveguide in the study by Jung et al. [179]. The electric field is added by placing gold on top of the AlN waveguide, and the electrical modulation is achieved through Pockels effect of AlN material.

Furthermore, the optical frequency comb covering IR wavelength region, red, and green in visible wavelength region have been achieved through the simultaneous second- and third-order nonlinear effects of polycrystalline AlN in 2014 in the study by Jung et al. [99]. The working principle of the device is illustrated in Figure 13(d). The wavelength span can be divided into three regions. The first region is at the near-IR wavelength region, in which the frequency comb is generated through FWM near the pump wavelength. The second region is at the red wavelength region, in which the frequency combs are generated through the Pockels effect. The frequency lines are generated by frequency mixing of comb lines through SHG and SFG. The third region is at the green wavelength region, in which the frequency combs are generated through THG. In order to achieve efficient wavelength conversion, phase matching condition needs to be satisfied. The effective indices of the AlN waveguide at different modes have been calculated, as shown in Figure 13(e). The black solid line represents the index for fundamental TE mode around 1550 nm. The red and green lines are index of various modes in red color and green color wavelength region. The phase matching condition can be found around the cross points of these two lines with the black solid line. To measure the frequency comb spectrum in both IR and visible, the setup illustrated in Figure 13(f) is used. 0.5% output signal is coupled into OSA to monitor the IR spectrum, and 0.5% output power is coupled into power meter for fiber-to-chip alignment purpose. The remaining 99% of optical power enters a grating to be dispersed vertically, followed by a prism to further disperse the frequency comb signal horizontally. A charge-coupled device (CCD) camera is placed at the end to visualize the dispersed spectrum in 2D. The images obtained from CCD together with the extracted spectra with normalized power are illustrated in Figure 13(g). The left inset in red color shows the extracted spectrum around 774 nm generated through SHG and SFG process. While the inset on the right side in green color shows the extracted spectrum around 517 nm generated through THG and third-order SFG nonlinear process.

In a later work by Liu et al. reported in 2018 [132], a significant improvement of nonlinear IR-to-visible power conversion efficiency of more than 40 times has been achieved using single-crystalline AlN, in comparison with polycrystalline AlN. Also, the number of near-visible comb lines has been significantly increased. The generated frequency comb spectrum at IR and near-visible wavelength regime under pump power of 1000 mW are captured by OSA and illustrated in Figure 13(h) and Figure 13(i), respectively. In Figure 13(h), the broadband NIR comb, although not shown fully, contains 92 comb lines. Also, there is a 7 dB attenuation to the spectrum in order to protect OSA from the high residual pump power. For near-visible wavelength regime in Figure 13(i), there are 153 comb lines captured by OSA. Regarding Kerr comb generation, an additional note worth mentioning is that a stabilized dissipative Kerr soliton (DKS) state has been realized in single crystalline AlN microring resonator in the year of 2018 in the study by Gong et al. [180]. The long-lasting DKS has been achieved through the optimized single-sideband modulation scan and pump power ramping.

AlN, with wurtzite crystalline structure, also exhibits Raman-active phonons. The first AlN-based waveguide Raman laser has been reported in 2017 in the study by Liu et al. [101]. By using a high Q microring resonator formed by single crystalline AlN on sapphire substrate, the lasing slope efficiency of 15% for first Stokes at 1738 nm has been

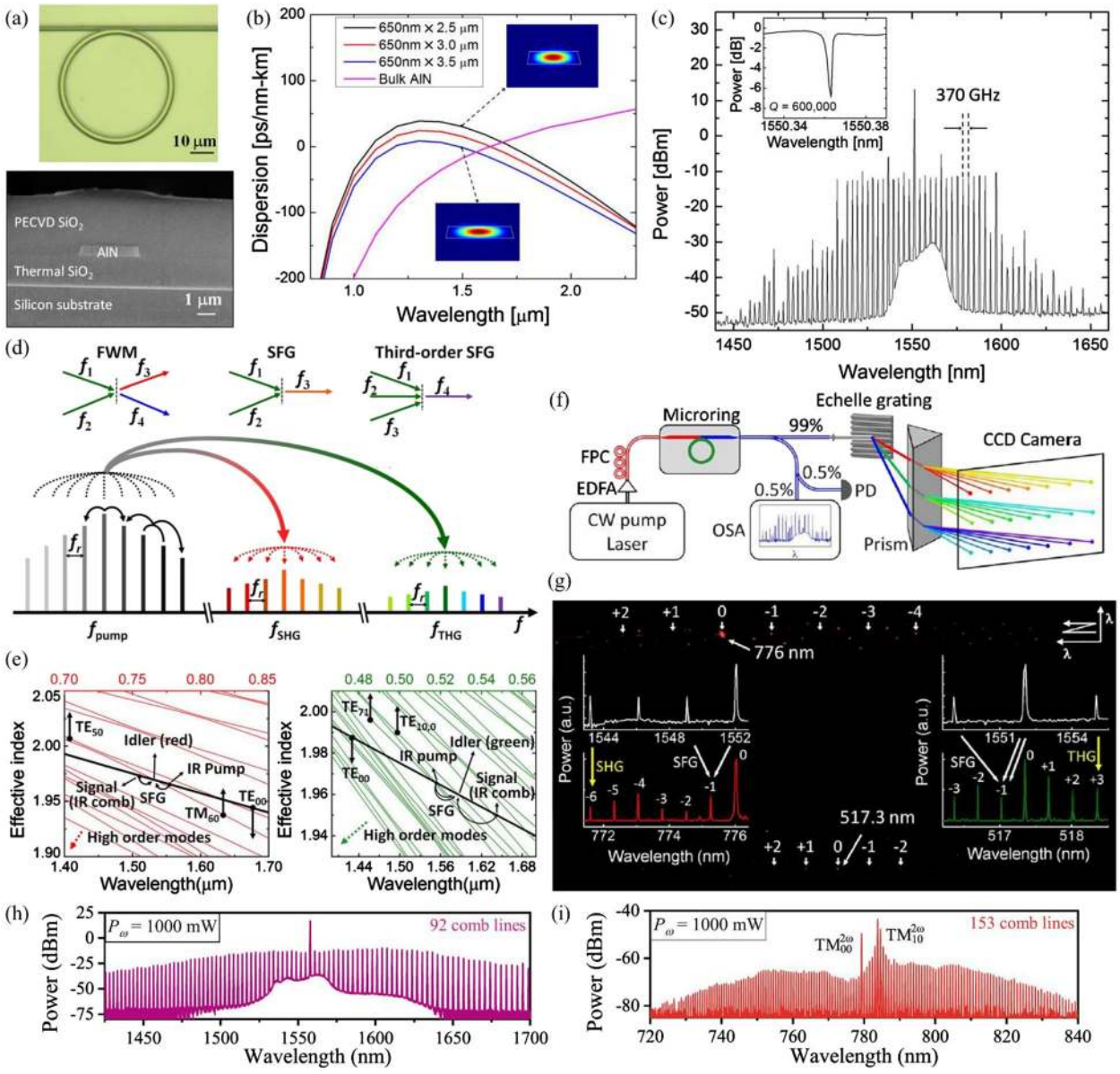

Figure 13: AlN-based integrated devices for $\chi^{(3)}$ Kerr comb generation.
(a) Top: microscopic image of microring resonator for Kerr comb generation. Bottom: cross sectional SEM image of AlN waveguide. (b) Dispersion relation of AlN waveguides fundamental TE mode under different waveguide width. Insets show the simulated mode intensity profiles at 1550 nm for waveguide width of 2.5 and 3.5 μm. (c) Optical frequency comb generated by the fabricated microring resonator, spanning from 1450 to 1650 nm. Inset shows the transmission spectrum of resonance mode, with loaded Q value of 6×10^5. (a)–(c) Adapted with permission from [178] © The Optical Society. (d) Principle of wide frequency comb generation, including the mechanisms of cascaded FWM for IR wavelength region, SHG and SFG for red color wavelength region, THG and third-order SFG for green color wavelength region. (e) Numerical simulated waveguide refractive index with respect to different wavelengths. Black solid line is for fundamental TE mode at IR around 1550 nm. Red lines (left panel) represent different modes around 770 nm. Green lines (right panel) represent different modes around 520 nm. Phase matching condition can be found at the crossing points between black line and red/green line. (f) Schematic of setup for frequency comb generation and characterization. FPC: fiber polarization controller. (g) CCD camera image and extracted spectra with normalized power, plotted in red color (left inset) and green color (right inset). (d)–(g) Adapted with permission from [99] © The Optical Society. (h) Single crystalline AlN NIR optical frequency comb spectrum, containing 92 comb lines. Note: comb is not fully shown, and there is a 7 dB attenuation to the spectrum to protect OSA from residual pump. (i) Near-visible frequency comb spectrum generated through SHG, showing 153 comb lines. (h) and (i) Adapted from [132], with the permission of AIP Publishing.

demonstrated. The schematic of the microring Raman laser with energy level diagram is shown in Figure 14(a). The calculated mode intensity profile at pump, first Stokes, second Stokes wavelengths, and the cross sectional SEM image of fabricated waveguide are also included. Figure 14(b) left panel presents the lasing spectrum of the first and second Raman Stokes under on-chip TE-polarized pump power of ~126 mW. With high on-chip optical power (~158 mW), the frequency comb lines around pump, Stokes and anti-Stokes wavelengths can be observed, which are contributed by the interplay between Raman effect and Kerr nonlinearity. The frequency comb spectrum is also captured, as illustrated in Figure 14(b) right panel.

Based on the same material platform, Raman effect has been used to assist the frequency spanning in addition to FWM, as reported in 2018 in the study by Liu et al. [70]. The single-crystalline AlN is grown on sapphire via epitaxy, with schematic shown in Figure 14(c). The microring radius is 80 μm, with transmission spectrum obtained in Figure 14(d). Two sets of TE mode can be observed, as marked in green (TE_{00} – like) and blue (TE_{10} – like). Since two neighboring modes of these two sets are very close (12.21 GHz), there are mode interaction and hybrid mode existing. Figure 14(e) shows the relative frequency of hybrid mode with respect to unperturbed TE_{00} mode. From the figure, it can be observed that there are two avoided mode crossing regimes. Under pumping at 192.2 THz, it falls into the upper branch of hybrid mode, as indicated in Figure 14(e), which is dominated by TE_{00} mode. Under the low pump power condition (P_{in} = 126 mW), the cascaded stimulated Raman scattering (SRS) can be observed, with first, second Stokes and first anti-Stokes shown in Figure 14(f) top panel (marked in red). The absence of FWM is due to the normal group velocity dispersion (GVD) at the pumping frequency. As pump power (P_{in}) increases, the frequency comb lines start to appear around the pump, Stokes and anti-Stokes lines, which are contributed by the Raman assist FWM, as shown in Figure 14(f) bottom panel. Under high pump power (P_{in} = 1000 mW), it has been found that the first Stokes line actually acts as the pump for the cascaded FWM, and the new comb formation (marked in blue) is contributed by the avoided mode crossing.

In the following year (2019), the polycrystalline AlN on Si has also been demonstrated for Raman assisted frequency comb generation, with broader Raman gain linewidth (295–351 GHz) in the study by Jung et al. [100]. The principle of broadband Raman-assisted comb generation is illustrated in Figure 14(g). With enough pump power, the spectrum broadening is contributed by the combination of Stokes Raman scattering, anti-Stokes Raman scattering, and cascaded FWM. The microring resonator comb generation device is characterized using the setup shown in Figure 14(h). A tunable laser cascaded with an EDFA is used as pump source. Fiber polarization controller (FPC) is used to selectively excite TE or TM mode within the microring cavity. The optical isolator is used to project EDFA from reflected light. Two OSAs, one in NIR wavelength range and the other in MIR wavelength range, are used to capture the generated spectrum. The captured spectrum under TE mode excitation is shown in Figure 14(i). The simulated pump intensity profile within the designed microring waveguide is also included as inset. The pumping wavelength is tuned into the resonance wavelength of the microring. The comb lines marked in blue are near the pump wavelength (1550 nm), which are generated by cascaded FWM. While the comb lines marked in black and red are generated by anti-Stokes and Stokes Raman scattering, respectively. The generated line spacing is around 1 FSR of the microring, indicating the Raman comb lines are originated from the cascaded FWM around pump wavelength. An additional note worth mentioning is that the dispersion of AlN-based microcomb resonators can be further engineered by tapering waveguide cross-section width within a ring resonator [194].

3.10 Supercontinuum generation

Supercontinuum generation (SCG) is a typical method to spectrally broaden the frequency combs to at least one octave, via $\chi^{(3)}$ nonlinearity of the material [195]. Integrated photonics circuit provides a suitable platform for SCG considering the high mode confinement and hence small effective mode area. The effective nonlinear coefficient can be expressed as

$$\gamma = \frac{2\pi n_2}{\lambda A_{\text{eff}}} \tag{2}$$

where n_2 is the Kerr refractive index, λ is the wavelength, A_{eff} is the effective mode area. SCG has been recently demonstrated on integrated photonics platforms based on different materials, including Si [22, 37], Si_3N_4 [196, 197], silica [198] and lithium niobate [199]. The compact integrated photonics platform not only has the advantage of low power threshold for SCG, but also has high scalability for mass device production.

With the advantages of coexistence of $\chi^{(2)}$ and $\chi^{(3)}$ nonlinear effects, and wide transparency window covering from UV to MIR, AlN material becomes a suitable candidate for SCG [73, 123, 133, 134]. Ultra-broadband SCG has been reported using AlN photonic waveguide in 2017, covering from 500 to 4000 nm in the study by Hickstein et al. [133]. The schematic of the device is shown in Figure 15(a). The AlN waveguide is fully embedded in SiO_2 on Si substrate. The waveguide height is 800 nm, and its width is varied

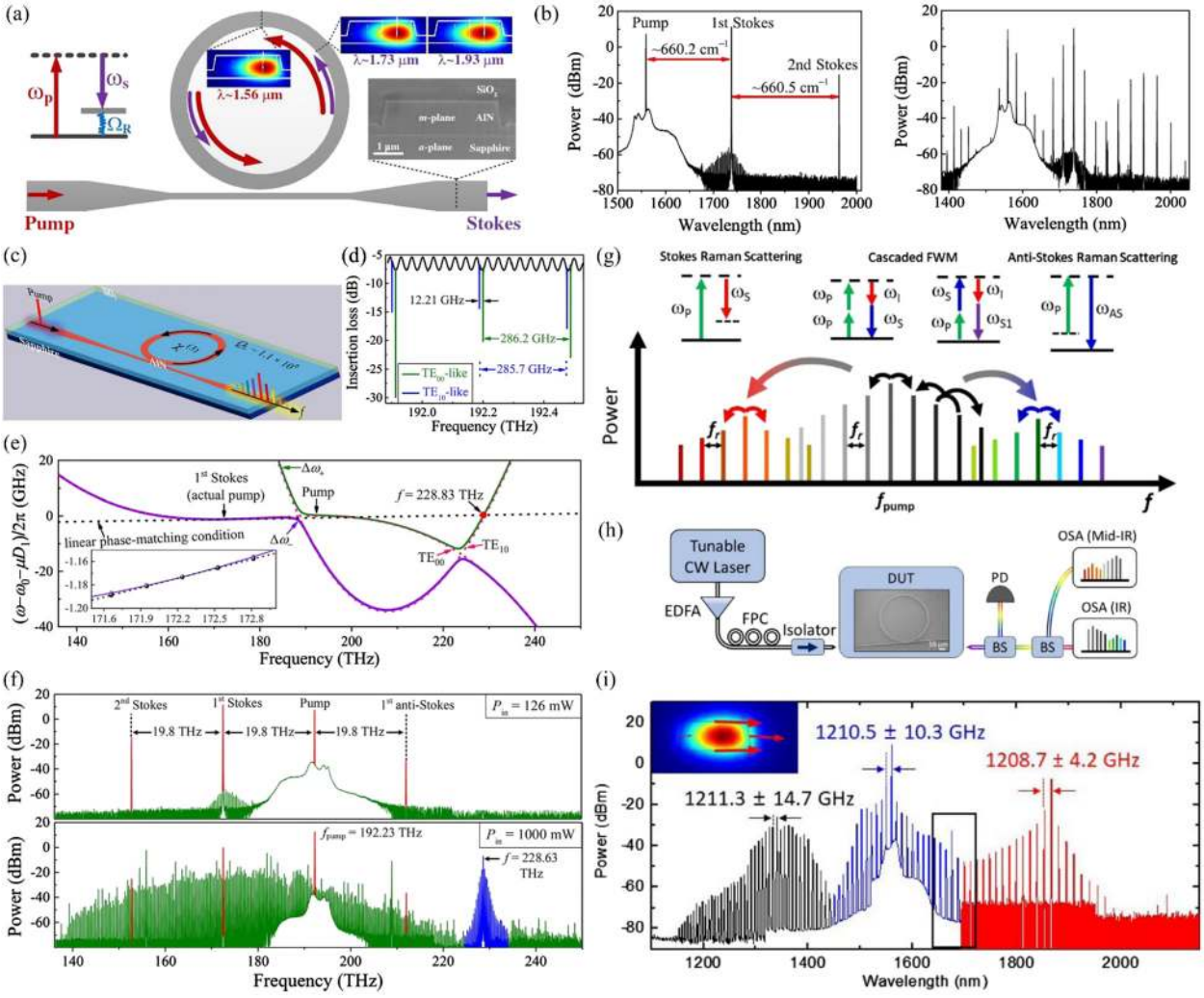

Figure 14: AlN-based integrated devices for Raman-assisted frequency comb generation.
(a) Schematic of AlN microring for Raman lasing, including energy level for SRS on the left, calculated mode intensity profiles at pump, first and second Raman Stoke, as well as the cross sectional SEM image of fabricated waveguide on the right. (b) Left panel: Raman lasing spectrum under on-chip TE-polarized pump power of ~126 mW. Right panel: frequency comb generated around pump, first and second Stokes under on-chip TE-polarized power of ~158 mW. (a)–(b) Adapted with permission from [101] © The Optical Society. (c) Schematic of single-crystalline AlN microring on sapphire substrate for Raman-assisted Kerr comb generation. (d) Transmission spectra for TE_{00}- and TE_{10}- like modes, with ring radius of 80 μm. (e) Calculated relative frequency between the hybrid mode and the unperturbed TE_{00} mode. Magenta dashed lines represent the unperturbed TE_{00} and TE_{10} modes. Black dashed line represents the linear phase-matching condition with first Stokes line as pump for FWM process. Inset shows the zoom-in view of the tangent property at first Stokes frequency. (f) Raman-assisted comb pumped at TE_{00}-like mode with low pump power P_{in} = 126 mW (top panel) and high pump power P_{in} = 1000 mW (bottom panel). Pump, Stokes and anti-Stokes are indicated by red lines. Raman-assisted comb is indicated by green lines. Comb lines generated by avoided mode crossing are indicated in blue lines. (c)–(f) Adapted with permission from [70]. Copyright (2018) American Chemical Society. (g) Principle of broadband Raman-assisted Kerr comb generation. (h) Fabricated device characterization setup. DUT: device under test. BS: beam splitter. (i) Measured spectrum of Raman-assisted broadband frequency comb, when DUT is under TE mode excitation around 1550 nm. Blue comb lines are generated through cascaded FWM. Black and red comb lines are contributed by the anti-Stokes and Stokes Raman scattering. Frequency gap between two lines is close to 1 FSR of the microring, which indicates that the Raman-assisted comb lines are originated from FWM. Inset: simulated TE mode intensity profile at 1550 nm within the designed microring waveguide. (g)–(i) Adapted with permission from [100] © The Optical Society.

from 400 to 5100 nm. The false-colored SEM image of the AlN cross section is shown in the inset of Figure 15(a). Erbium-fiber frequency comb at communication wavelength is used as pump source. The schematic of experimental setup is illustrated in Figure 15(b). At the output, two OSAs are used to capture the spectrum, one grating-based OSA covers from visible to NIR wavelength range, and the other Fourier-Transform based OSA covers

up into MIR wavelength range. The captured optical spectrum and the simulated SCG output for waveguide with width of 3200 nm are presented in Figure 15(c). The experimental spectrum is obtained from the waveguide under the TE_{00} mode pump. The broadband spectrum is contributed by the flat GVD of light within the waveguide. The simulated spectrum is obtained by solving the nonlinear Schrödinger equation (NLSE), which considers the $\chi^{(3)}$ nonlinear effect, and also wavelength dependence of the waveguide effective refractive index. AlN has significant $\chi^{(2)}$ nonlinear effect, and the AlN thin film is polycrystalline material, with c-axis normal to the film plane [91]. Hence, there is a potential to explore the AlN $\chi^{(2)}$ nonlinear effect using pump with vertically polarized direction, which is the TM mode. Figure 15(d) shows the captured output spectrum from SCG under TM_{00} mode pumping. Both waveguides with width of 1000 and 1700 nm are used for SCG. Besides SCG, the SHG, DFG and THG can also be observed in Figure 15(d). For 1000 nm width waveguide, the SHG peak is contributed by the phase matching between the higher-order mode and the fundamental mode. For 1900 nm width waveguide, the DFG in the wavelength region from 3500 to 5500 nm can be observed, which corresponds to the frequency difference between the broadened pump signal from 1400 to 1700 nm and the dispersive wave from 2000 to 2700 nm. In the meanwhile, for 1000 nm width waveguide, the wavelength of such DFG is longer and beyond measurement range since its dispersive wave moves to shorter wavelength range.

Furthermore, the SCG in near-visible wavelength range and the UV frequency comb generation through SHG have been demonstrated in 2019 on single-crystalline AlN-on-sapphire platform in the study by Liu et al. [73]. Figure 15(e) shows the schematic of SCG in near-visible (red curve) through $\chi^{(3)}$ nonlinear effect, and simultaneous conversion into the UV frequency comb (purple curve) through $\chi^{(2)}$ nonlinear effect (SHG and SFG). In order to achieve efficient SHG, the phase matching condition has to be satisfied as discussed earlier. Figure 15(f) illustrates the phase matching condition between fundamental mode (TM_{00}) and second-order mode (TM_{20}) from calculation. The calculated mode intensity profiles and the cross sectional SEM image of the fabricated waveguide are also included as insets. The figure indicates that the phase matching condition is sensitive to the waveguide width, and hence leads to narrow bandwidth of the SHG for straight waveguide. For broadband nonlinear conversion, adiabatic taper structures can be used [200]. To overcome the limitation of linear-tapered waveguide, including lithography precision, and $\chi^{(2)}$ nonlinear effects (SHG, SFG) efficiency with degraded near-visible peak power, chirp-modulated taper waveguide is implemented. The schematic drawing of the device is presented in Figure 15(g). The chirp modulated waveguides are formed by cascading eight linear-tapered segments. The SCG process within the waveguide has been simulated by solving the generalized NLSE, with the simulated result presented in Figure 15(h). The left panel shows the spectrum domain simulation result. As the wave propagates, the SCG across the near-visible spectra can be observed under the input pulse energy of 237 pJ, which is mainly contributed by the self-phase modulation (SPM). At the spectra wing, the optical wave breaking (OWB) can be observed. Meanwhile, the time domain evolution from simulation is shown in the right panel, in which the degradation of the pulse peak power along the waveguide can be observed. The experimental captured spectra generated by the chirped-tapered waveguide at near-visible and UV wavelength range are presented in Figure 15(i), under on-chip input pulse energy of 237 pJ. The near-visible spectrum from SCG has ripples in the central, which are contributed by the interplay between the SPM and OWB. This is in agreement with the simulation result discussed earlier in Figure 15(h). The UV combs obtained have a flat top, which is contributed by the chirped-tapered waveguide design discussed earlier. The combs generated cover from 360 to 425 nm, which correspond to a frequency span of 128 THz. Also, the fluorescence on a white paper induced by the UV light is included as inset.

In the earlier work discussed above, the pump wavelength is at 780 nm, and the SCG spectrum is limited up to around 900 nm. In a follow-up work in 2020, based on the same single-crystalline AlN platform, ultra-broadband SCG from UV to MIR wavelength regime has been demonstrated, under the pump wavelength at 1560 nm in the study by Lu et al. [123]. Leveraging on the coexistence of $\chi^{(2)}$ and $\chi^{(3)}$ nonlinearity for AlN waveguide, the wavelength covers from 400 to 4200 nm in Ref. [123].

4 Summary and outlook

To sum up, the recent research progress on AlN-based integrated photonics has been reviewed and presented. The related physical properties of AlN have been summarized. Compared with Si, AlN has large bandgap, wide transparency window and significant second-order nonlinear optical effect. Furthermore, contributed by its non-centrosymmetric crystal structure, AlN also exhibits

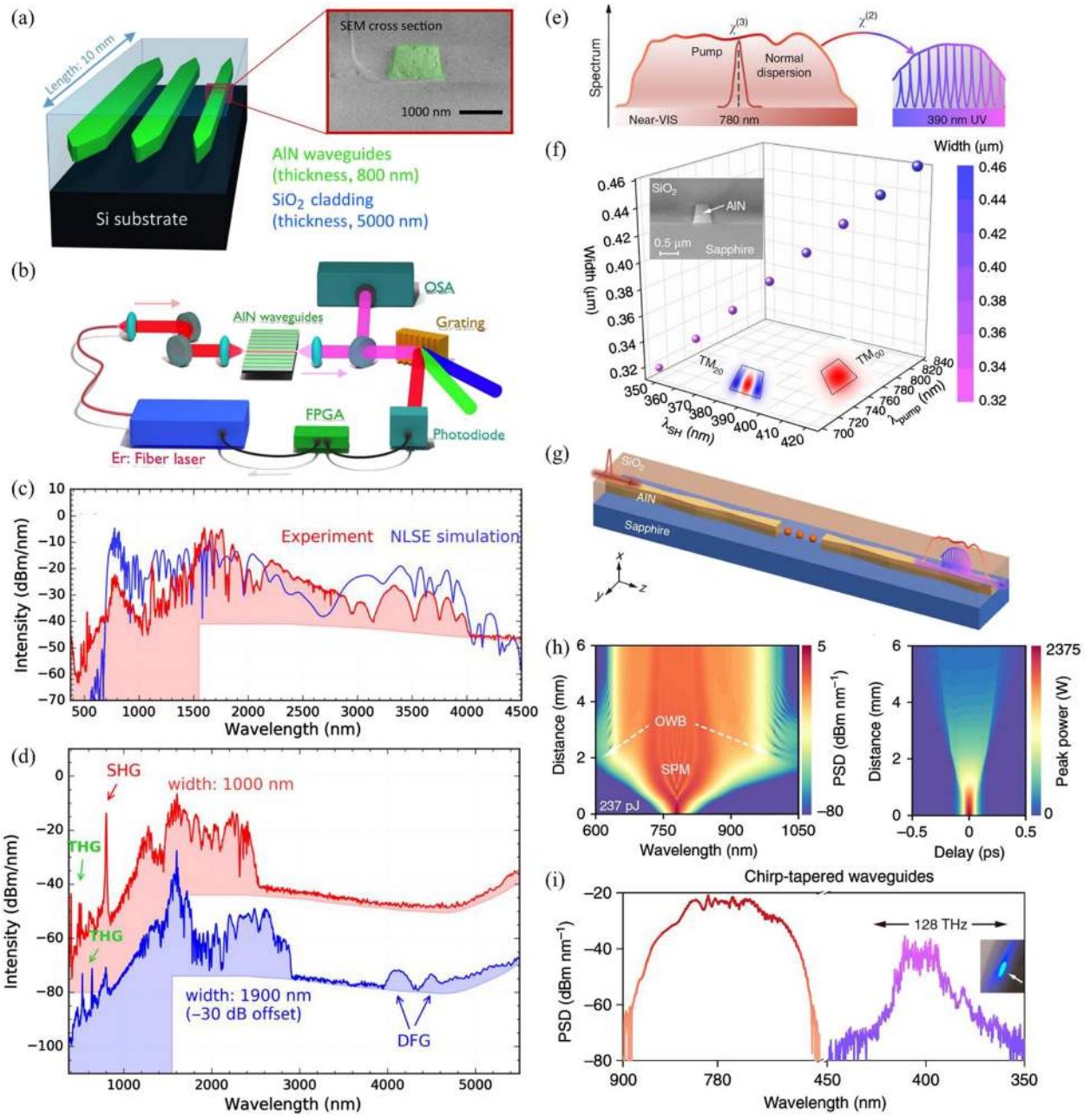

Figure 15: AlN-based integrated devices for supercontinuum generation (SCG).
(a) Schematic of AlN waveguide embedded in SiO_2 on Si substrate for SCG. Inset shows the false-colored cross sectional SEM image of the fabricated waveguide. (b) Experimental setup for SCG. Erbium-fiber frequency comb at 1560 nm is used as pump. Two OSAs are used to capture the spectrum at the output, one grating-based OSA covers from visible to NIR wavelength range, and the other Fourier-Transform based OSA covers up into MIR wavelength range. Photodiode is used to detect f_{CEO}, which is digitized by field-programmable gate array (FPGA), and feedback to the fiber laser pump source. (c) Experimental captured SCG spectrum from 3200 nm wide waveguide under pumping with TE_{00} mode, and the simulated SCG spectrum by solving the NLSE. (d) Experimental captured SCG spectrum under pumping with TM_{00} mode for waveguides with widths of 1000 and 1900 nm. SHG, DFG and THG can also be observed. (a)–(d) Adapted with permission from [133], copyright (2017) by the American Physical Society. (e) Schematic of SCG in near-visible wavelength (red curve) through $\chi^{(3)}$ nonlinear effect, and simultaneous conversion into the UV frequency comb (purple curve) through $\chi^{(2)}$ nonlinear effect. (f) Phase matching condition between near-visible TM_{00} mode and UV TM_{20} mode from calculation. Insets: mode intensity profiles and the cross sectional SEM image of the fabricated waveguide. (g) Schematic of chirp-modulated taper waveguide, formed by cascading eight linear-tapered segments. (h) Simulated SCG in spectrum domain (left panel) and time domain (right panel). (i) Captured spectra generated by the chirped-tapered waveguide at near-visible and UV wavelength range. Inset: fluorescence on a white paper induced by UV light. (e)–(i) Adapted with permission from [73]. Licensed under a Creative Commons Attribution.

piezoelectric and pyroelectric properties, which make it a suitable material for multiphysics coupling. Following the physical properties, the AlN-based functional devices demonstrated in the past decade have been summarized and presented. These functional devices are categorized as linear optical devices (coupler, waveguide, resonator, etc.), optomechanical devices, emitters, photodetectors, metasurface, and nonlinear optical devices. The selected key experimental results from these devices are also presented.

In the near future, the research and development of AlN-based integrated photonics can be directed in the following pathways. Firstly, in order to enhance the piezoelectric and pyroelectric effect of AlN, Sc has been added into AlN as dopant, as mentioned earlier. At the Sc doping concentration of 40%, the ScAlN is able to achieve a piezoelectric coefficient of about five times as the undoped AlN [108], and maintains the advantages of AlN, including CMOS-compatibility, lead free, and ease of fabrication [109]. Various piezoelectric MEMS devices have been demonstrated on ScAlN platform [201–205]. Not only the piezoelectric coefficient but also the other physical properties contributed by the noncentrosymmetric crystal structure, including pyroelectric coefficient and second-order nonlinear coefficient, are expected to be higher with Sc doping. In the meanwhile, the study of optical properties of ScAlN is limited, and can be one of the keys to explore for AlN-based photonics. So far, to the best of our knowledge, only ScAlN photonics waveguide and microring resonator have been demonstrated [206]. The waveguide propagation loss has been reported as 9 dB/cm at 1550 nm, and microring quality factor is 1.4×10^4. Both are limited by the material loss and waveguide surface roughness, which can be improved through fabrication process optimization, including etching for reduced side wall roughness, vertical side wall angle, and annealing process to reduce waveguide loss [90, 207]. Figure 2(f) discussed earlier shows a good example on how the annealing process can help to reduce the optical loss of AlN waveguide. The future work can be the fabrication process optimization for ScAlN photonics circuit on Si wafer substrate, and the exploration of nonlinear optical properties of ScAlN. Besides optical property, ScAlN also exhibits the ferroelectric property [208, 209]. Such property can be used for nonvolatile memory (NVM). In combination with its optical properties discussed earlier, ScAlN platform has the potential for the demonstration of photonics memory [210].

Secondly, AlN can be utilized as integrated light emitters or optical amplifiers by doping rare-earth elements within AlN [211]. The rare-earth ions are the source of emission under optical pumping. Compared with traditional semiconductor-based emitters, the rare-earth-doped light emitter has the advantage of monolithic integration by using CMOS-compatible fabrication process [212], and potential for narrow linewidth emission [213, 214]. The monolithically integrated rare-earth-doped lasers using Al_2O_3 as host material have been recently demonstrated on Si substrate using CMOS-compatible fabrication process [215–218]. Rare-earth elements such as Ytterbium, Erbium, Thulium, and Holmium have been used for amplification or lasing on Si at the wavelength around 1.0 μm [219, 220], 1.55 μm [221–223], 1.8 μm [224, 225], and 2.0 μm [226], respectively. Compared with Al_2O_3, AlN has wider transparency window [227], and also higher refractive index for better mode confinement. Based on rare-earth-doped AlN, the luminescence in UV, blue, green, yellow, and red have been demonstrated by doping Gadolinium [228], Cerium [229], Terbium [230], Dysprosium [231], and Europium [231], respectively. More active functional devices, including lasers and optical amplifiers, are expected to be developed and demonstrated based on rare-earth-doped AlN on CMOS-compatible platform.

Last but not the least, further explorations on AlN-based quantum devices is another direction. As discussed earlier, AlN has advantages of large bandgap and significant nonlinear optical character. These advantages enable AlN to be utilized as material for waveguide and emitter within integrated quantum systems [127, 150, 151, 232]. Also, contributed by the piezoelectric nature of AlN, the quantum state of mechanical resonator can be controlled. A typical example utilizing AlN can be found in Ref. [233]. The optomechanical devices [69, 107, 234], which can couple acoustic mode with optical mode, have the potential to be utilized as a microwave-optical transducer in quantum systems. Furthermore, AlN piezoelectric property can also be used for strain-based control to switch the quantum state in nitrogen-vacancy center [235]. In addition, more research works can be conducted by combining optomechanics with nonlinear optics to study optomechanics in quantum regime [67].

List of abbreviations

AlN	Aluminum nitride
BS	Beam splitter
CCW	Counter-clockwise
CCD	Charge-coupled device
CD	Critical dimension
CW	Clock-wise
DFG	Difference frequency generation
DKS	Dissipative Kerr soliton
DUT	Device under test
EDFA	Erbium-doped-fiber amplifier
ER	Extinction ratio

FDTD	Finite difference time domain
FPC	Fiber polarization controller
FPGA	Field-programmable gate array
FSR	Free spectral range
FWHM	Full-width-half-maximum
FWM	Four wave mixing
GVD	Velocity dispersion
IDT	Inter-digital transducer
IR	Infrared
LED	Light emitting diode
LPCVD	Low pressure chemical vapor deposition
MBE	Molecular beam epitaxy
MEMS	Microelectromechanical system
MIR	Mid infrared
MOCVD	Metal-organic chemical vapor deposition
MOVPE	Metalorganic vapor phase epitaxy
MWP	Microwave photonics
MZI	Mach–Zehnder interferometer
NA	Numerical aperture
NIR	Near infrared
NLSE	Nonlinear Schrödinger equation
NVM	Nonvolatile memory
OSA	Optical frequency analyzer
OWB	Optical wave breaking
PECVD	Plasma-enhanced chemical vapor deposition
PD	Photodetector
PhC	Photonic crystal
Q	Quality factor
RF	Radio frequency
SAW	Surface acoustic wave
ScAlN	Scandium-doped aluminum nitride
SCG	Supercontinuum generation
SEM	Scanning electron microscopy
SFG	Sum frequency generation
SHG	Second harmonic generation
SPM	Self-phase modulation
SRS	Stimulated Raman scattering
TE	Transverse electric
TEM	Transmission electron microscopy
THG	Third harmonic generation
TM	Transverse magnetic
TO	Transistor outline
TWM	Three wave mixing
UV	Ultraviolet
1D	One-dimensional
3D	Three-dimensional

Acknowledgment: The authors would like to thank Dr. Prakash Pitchappa, Dr. Li Minghua, Dr. Chen Liu and Dr. Elaine Cristina Schubert Barretto for discussions.

Author statement: All the authors have accepted responsibility for the entire content of this submitted manuscript and approved submission.

Research funding: This work is supported by Agency for Science, Technology and Research IAF-PP A19B3a0008 and IAF-PP A1789a0024.

Conflict of interest statement: The authors declare no conflicts of interest regarding this article.

References

[1] T. L. Koch and U. Koren, "Semiconductor photonic integrated circuits," *IEEE J. Quant. Electron.*, vol. 27, no. 3, pp. 641–653, 1991.

[2] R. Nagarajan, C. H. Joyner, R. P. Schneider, et al., "Large-scale photonic integrated circuits," *IEEE J. Sel. Top. Quant. Electron.*, vol. 11, no. 1, pp. 50–65, 2005.

[3] M. J. R. Heck, J. F. Bauters, M. L. Davenport, et al., "Hybrid silicon photonic integrated circuit technology," *IEEE J. Sel. Top. Quant. Electron.*, vol. 19, no. 4, p. 6100117, 2013.

[4] F. Kish, V. Lal, P. Evans, et al., "System-on-Chip photonic integrated circuits," *IEEE J. Sel. Top. Quant. Electron.*, vol. 24, no. 1, pp. 1–20, 2018.

[5] M.-G. Suh and K. J. Vahala, "Soliton microcomb range measurement," *Science*, vol. 359, no. 6378, p. 884, 2018.

[6] P. Trocha, M. Karpov, D. Ganin, et al., "Ultrafast optical ranging using microresonator soliton frequency combs," *Science*, vol. 359, no. 6378, p. 887, 2018.

[7] J. Riemensberger, A. Lukashchuk, M. Karpov, et al., "Massively parallel coherent laser ranging using a soliton microcomb," *Nature*, vol. 581, no. 7807, pp. 164–170, 2020.

[8] A. Tittl, A. Leitis, M. Liu, et al., "Imaging-based molecular barcoding with pixelated dielectric metasurfaces," *Science*, vol. 360, no. 6393, p. 1105, 2018.

[9] D. Kim, M. I. Ibrahim, C. Foy, M. E. Trusheim, R. Han, and D. R. Englund, "A CMOS-integrated quantum sensor based on nitrogen–vacancy centres," *Nat. Electron.*, vol. 2, no. 7, pp. 284–289, 2019.

[10] N. Li, H. Yuan, L. Xu, et al., "Radiation enhancement by graphene oxide on microelectromechanical system emitters for highly selective gas sensing," *ACS Sens.*, vol. 4, no. 10, pp. 2746–2753, 2019.

[11] S. Zheng, H. Cai, L. Xu, et al., "Miniaturized gas sensor based on silicon substrate-integrated hollow waveguides," in *Integrated Optics: Devices, Materials, and Technologies XXV*, vol. 11689, International Society for Optics and Photonics, 2021, p. 116890C.

[12] N. Li, Q. Chao, Z. Gu, et al., "Photonic crystal MEMS emitter for chemical gas sensing," in *MOEMS and Miniaturized Systems XX*, vol. 11697, International Society for Optics and Photonics, 2021, p. 116970M.

[13] N. C. Harris, G. R. Steinbrecher, M. Prabhu, et al., "Quantum transport simulations in a programmable nanophotonic processor," *Nat. Photonics*, vol. 11, no. 7, pp. 447–452, 2017.

[14] Y. Shen, N. C. Harris, S. Skirlo, et al., "Deep learning with coherent nanophotonic circuits," *Nat. Photonics*, vol. 11, no. 7, pp. 441–446, 2017.

[15] N. C. Harris, J. Carolan, D. Bunandar, et al., "Linear programmable nanophotonic processors," *Optica*, vol. 5, no. 12, pp. 1623–1631, 2018.

[16] B. J. Shastri, A. N. Tait, T. Ferreira de Lima, et al., "Photonics for artificial intelligence and neuromorphic computing," *Nat. Photonics*, vol. 15, no. 2, pp. 102–114, 2021.

[17] J. L. O'Brien, A. Furusawa, and J. Vučković, "Photonic quantum technologies," *Nat. Photonics*, vol. 3, no. 12, pp. 687–695, 2009.

[18] J. Wang, F. Sciarrino, A. Laing, and M. G. Thompson, "Integrated photonic quantum technologies," *Nat. Photonics*, vol. 14, no. 5, pp. 273–284, 2020.
[19] A. W. Elshaari, W. Pernice, K. Srinivasan, O. Benson, and V. Zwiller, "Hybrid integrated quantum photonic circuits," *Nat. Photonics*, vol. 14, no. 5, pp. 285–298, 2020.
[20] W. Bogaerts, P. De Heyn, T. Van Vaerenbergh, et al., "Silicon microring resonators," *Laser Photonics Rev.*, vol. 6, no. 1, pp. 47–73, 2012.
[21] J. C. Rosenberg, W. M. J. Green, S. Assefa, et al., "A 25 Gbps silicon microring modulator based on an interleaved junction," *Opt. Express*, vol. 20, no. 24, pp. 26411–26423, 2012.
[22] N. Singh, M. Xin, D. Vermeulen, et al., "Octave-spanning coherent supercontinuum generation in silicon on insulator from 1.06 μm to beyond 2.4 μm," *Light Sci. Appl.*, vol. 7, p. 17131, 2018.
[23] J. Sun, E. Timurdogan, A. Yaacobi, E. S. Hosseini, and M. R. Watts, "Large-scale nanophotonic phased array," *Nature*, vol. 493, no. 7431, pp. 195–199, 2013.
[24] Y. Huang, J. Song, X. Luo, T.-Y. Liow, and G.-Q. Lo, "CMOS compatible monolithic multi-layer Si3N4-on-SOI platform for low-loss high performance silicon photonics dense integration," *Opt. Express*, vol. 22, no. 18, pp. 21859–21865, 2014.
[25] Y. Liu, J. M. Shainline, X. Zeng, and M. A. Popović, "Ultra-low-loss CMOS-compatible waveguide crossing arrays based on multimode Bloch waves and imaginary coupling," *Opt. Lett.*, vol. 39, no. 2, pp. 335–338, 2014.
[26] M. J. R. Heck, J. F. Bauters, M. L. Davenport, D. T. Spencer, and J. E. Bowers, "Ultra-low loss waveguide platform and its integration with silicon photonics," *Laser Photonics Rev.*, vol. 8, no. 5, pp. 667–686, 2014.
[27] E. S. Magden, N. Li, M. Raval, et al., "Transmissive silicon photonic dichroic filters with spectrally selective waveguides," *Nat. Commun.*, vol. 9, no. 1, p. 3009, 2018.
[28] P. Dong, R. Shafiiha, S. Liao, et al., "Wavelength-tunable silicon microring modulator," *Opt. Express*, vol. 18, no. 11, pp. 10941–10946, 2010.
[29] N. Li, E. Timurdogan, C. V. Poulton, et al., "C-band swept wavelength erbium-doped fiber laser with a high-Q tunableinterior-ridge silicon microring cavity," *Opt. Express*, vol. 24, no. 20, pp. 22741–22748, 2016.
[30] S. Li, D. Zhang, J. Zhao, et al., "Silicon micro-ring tunable laser for coherent optical communication," *Opt. Express*, vol. 24, no. 6, pp. 6341–6349, 2016.
[31] N. Li, M. Xin, Z. Su, et al., "A silicon photonic data link with a monolithic erbium-doped laser," *Sci. Rep.*, vol. 10, no. 1, p. 1114, 2020.
[32] C. V. Poulton, M. J. Byrd, M. Raval, et al., "Large-scale silicon nitride nanophotonic phased arrays at infrared and visible wavelengths," *Opt. Lett.*, vol. 42, no. 1, pp. 21–24, 2017.
[33] D. Kwong, A. Hosseini, J. Covey, et al., "On-chip silicon optical phased array for two-dimensional beam steering," *Opt. Lett.*, vol. 39, no. 4, pp. 941–944, 2014.
[34] J. Notaros, N. Li, C. V. Poulton, et al., "CMOS-compatible optical phased array powered by a monolithically-integrated erbium laser," *J. Lightwave Technol.*, vol. 37, no. 24, pp. 5982–5987, 2019.
[35] S. A. Miller, Y.-C. Chang, C. T. Phare, et al., "Large-scale optical phased array using a low-power multi-pass silicon photonic platform," *Optica*, vol. 7, no. 1, pp. 3–6, 2020.
[36] J. Leuthold, C. Koos, and W. Freude, "Nonlinear silicon photonics," *Nat. Photonics*, vol. 4, no. 8, pp. 535–544, 2010.
[37] N. Singh, D. Vermulen, A. Ruocco, et al., "Supercontinuum generation in varying dispersion and birefringent silicon waveguide," *Opt. Express*, vol. 27, no. 22, pp. 31698–31712, 2019.
[38] H. C. Frankis, Z. Su, N. Li, et al., "Four-wave mixing in a high-Q aluminum oxide microcavity on silicon," in *Conference on Lasers and Electro-Optics*, San Jose, CA, USA, OSA Technical Digest (online) (Optical Society of America, 2018), paper STh3I.3.
[39] L. Zhang, A. M. Agarwal, L. C. Kimerling, and J. Michel, "Nonlinear Group IV photonics based on silicon and germanium: from near-infrared to mid-infrared," *Nanophotonics*, vol. 3, nos 4–5, pp. 247–268, 2014.
[40] D. T. Spencer, T. Drake, T. C. Briles, et al., "An optical-frequency synthesizer using integrated photonics," *Nature*, vol. 557, no. 7703, pp. 81–85, 2018.
[41] M. Xin, N. Li, N. Singh, et al., "Optical frequency synthesizer with an integrated erbium tunable laser," *Light Sci. Appl.*, vol. 8, no. 1, p. 122, 2019.
[42] N. Singh, M. Xin, N. Li, et al., "Silicon photonics optical frequency synthesizer," *Laser Photonics Rev.*, vol. 14, p. 1900449, 2020.
[43] H. Rong, R. Jones, A. Liu, et al., "A continuous-wave Raman silicon laser," *Nature*, vol. 433, no. 7027, pp. 725–728, 2005.
[44] Purnawirman, N. Li, E. S. Magden, et al., "Wavelength division multiplexed light source monolithically integrated on a silicon photonics platform," *Opt. Lett.*, vol. 42, no. 9, pp. 1772–1775, 2017.
[45] K. Shtyrkova, P. T. Callahan, N. Li, et al., "Integrated CMOS-compatible Q-switched mode-locked lasers at 1900nm with an on-chip artificial saturable absorber," *Opt. Express*, vol. 27, no. 3, pp. 3542–3556, 2019.
[46] J. Michel, J. Liu, and L. C. Kimerling, "High-performance Ge-on-Si photodetectors," *Nat. Photonics*, vol. 4, no. 8, pp. 527–534, 2010.
[47] R. Going, T. J. Seok, J. Loo, K. Hsu, and M. C. Wu, "Germanium wrap-around photodetectors on Silicon photonics," *Opt. Express*, vol. 23, no. 9, pp. 11975–11984, 2015.
[48] M. J. Byrd, E. Timurdogan, Z. Su, et al., "Mode-evolution-based coupler for high saturation power Ge-on-Si photodetectors," *Opt. Lett.*, vol. 42, no. 4, pp. 851–854, 2017.
[49] A. H. Atabaki, S. Moazeni, F. Pavanello, et al., "Integrating photonics with silicon nanoelectronics for the next generation of systems on a chip," *Nature*, vol. 556, no. 7701, pp. 349–354, 2018.
[50] T. Kim, P. Bhargava, C. V. Poulton, et al., "A single-chip optical phased array in a wafer-scale silicon photonics/CMOS 3D-integration platform," *IEEE J. Solid State Circ.*, vol. 54, no. 11, pp. 3061–3074, 2019.
[51] C. Kittel, *Introduction to Solid State Physics*, 8th ed. New York, John Wiley & Sons, 2004.
[52] H. Yamashita, K. Fukui, S. Misawa, and S. Yoshida, "Optical properties of AlN epitaxial thin films in the vacuum ultraviolet region," *J. Appl. Phys.*, vol. 50, no. 2, pp. 896–898, 1979.
[53] M. Soltani, R. Soref, T. Palacios, and D. Englund, "AlGaN/AlN integrated photonics platform for the ultraviolet and visible spectral range," *Opt. Express*, vol. 24, no. 22, pp. 25415–25423, 2016.

[54] W. H. P. Pernice, C. Xiong, C. Schuck, and H. X. Tang, "Second harmonic generation in phase matched aluminum nitride waveguides and micro-ring resonators," *Appl. Phys. Lett.*, vol. 100, no. 22, p. 223501, 2012.
[55] N. Sinha, G. E. Wabiszewski, R. Mahameed, et al., "Piezoelectric aluminum nitride nanoelectromechanical actuators," *Appl. Phys. Lett.*, vol. 95, no. 5, p. 053106, 2009.
[56] R. B. Karabalin, M. H. Matheny, X. L. Feng, et al., "Piezoelectric nanoelectromechanical resonators based on aluminum nitride thin films," *Appl. Phys. Lett.*, vol. 95, no. 10, p. 103111, 2009.
[57] C. Fei, X. Liu, B. Zhu, et al., "AlN piezoelectric thin films for energy harvesting and acoustic devices," *Nanomater. Energy*, vol. 51, pp. 146–161, 2018.
[58] Y. Zhu, N. Wang, C. Sun, S. Merugu, N. Singh, and Y. Gu, "A high coupling coefficient 2.3-GHz AlN resonator for high band LTE filtering application," *IEEE Electron. Dev. Lett.*, vol. 37, no. 10, pp. 1344–1346, 2016.
[59] G. Wu, Y. Zhu, S. Merugu, N. Wang, C. Sun, and Y. Gu, "GHz spurious mode free AlN lamb wave resonator with high figure of merit using one dimensional phononic crystal tethers," *Appl. Phys. Lett.*, vol. 109, no. 1, p. 013506, 2016.
[60] C. Sun, B. W. Soon, Y. Zhu, et al., "Methods for improving electromechanical coupling coefficient in two dimensional electric field excited AlN Lamb wave resonators," *Appl. Phys. Lett.*, vol. 106, no. 25, p. 253502, 2015.
[61] J. Bochmann, A. Vainsencher, D. D. Awschalom, and A. N. Cleland, "Nanomechanical coupling between microwave and optical photons," *Nat. Phys.*, vol. 9, no. 11, pp. 712–716, 2013.
[62] D. B. Sohn, S. Kim, and G. Bahl, "Time-reversal symmetry breaking with acoustic pumping of nanophotonic circuits," *Nat. Photonics*, vol. 12, no. 2, pp. 91–97, 2018.
[63] E. A. Kittlaus, W. M. Jones, P. T. Rakich, N. T. Otterstrom, R. E. Muller, and M. Rais-Zadeh, "Electrically driven acousto-optics and broadband non-reciprocity in silicon photonics," *Nat. Photonics*, vol. 15, pp. 43–52, 2021.
[64] C. Ranacher, C. Consani, A. Tortschanoff, et al., "A CMOS compatible pyroelectric mid-infrared detector based on aluminium nitride," *Sensors*, vol. 19, no. 11, 2019, https://doi.org/10.3390/s19112513.
[65] J. W. Stewart, J. H. Vella, W. Li, S. Fan, and M. H. Mikkelsen, "Ultrafast pyroelectric photodetection with on-chip spectral filters," *Nat. Mater.*, vol. 19, no. 2, pp. 158–162, 2020.
[66] D. K. T. Ng, T. Zhang, L. Y. Siow, et al., "A functional CMOS compatible MEMS pyroelectric detector using 12%-doped scandium aluminum nitride," *Appl. Phys. Lett.*, vol. 117, no. 18, p. 183506, 2020.
[67] C. Xiong, W. H. P. Pernice, X. Sun, C. Schuck, K. Y. Fong, and H. X. Tang, "Aluminum nitride as a new material for chip-scale optomechanics and nonlinear optics," *New J. Phys.*, vol. 14, no. 9, p. 095014, 2012.
[68] H. Jung and H. X. Tang, "Aluminum nitride as nonlinear optical material for on-chip frequency comb generation and frequency conversion," *Nanophotonics*, vol. 5, no. 2, pp. 263–271, 2016.
[69] S. A. Tadesse and M. Li, "Sub-optical wavelength acoustic wave modulation of integrated photonic resonators at microwave frequencies," *Nat. Commun.*, vol. 5, no. 1, p. 5402, 2014.
[70] X. Liu, C. Sun, B. Xiong, et al., "Integrated high-Q crystalline AlN microresonators for broadband Kerr and Raman frequency combs," *ACS Photonics*, vol. 5, no. 5, pp. 1943–1950, 2018.
[71] K. Yamamoto, F. Goericke, A. Guedes, et al., "Pyroelectric aluminum nitride micro electromechanical systems infrared sensor with wavelength-selective infrared absorber," *Appl. Phys. Lett.*, vol. 104, no. 11, p. 111111, 2014.
[72] S. G. Bishop, J. P. Hadden, F. D. Alzahrani, et al., "Room-temperature quantum emitter in aluminum nitride," *ACS Photonics*, vol. 7, no. 7, pp. 1636–1641, 2020.
[73] X. Liu, A. W. Bruch, J. Lu, et al., "Beyond 100 THz-spanning ultraviolet frequency combs in a non-centrosymmetric crystalline waveguide," *Nat. Commun.*, vol. 10, no. 1, p. 2971, 2019.
[74] A. L. Gaeta, M. Lipson, and T. J. Kippenberg, "Photonic-chip-based frequency combs," *Nat. Photonics*, vol. 13, no. 3, pp. 158–169, 2019.
[75] S. Zhu, Q. Zhong, T. Hu, et al., "Aluminum nitride ultralow loss waveguides and push-pull electro-optic modulators for near infrared and visible integrated photonics," in *Optical Fiber Communication Conference (OFC) 2019, OSA Technical Digest*, San Diego, CA, USA, Optical Society of America, 2019, p. W2A.11.
[76] P. Gräupner, J. C. Pommier, A. Cachard, and J. L. Coutaz, "Electro-optical effect in aluminum nitride waveguides," *J. Appl. Phys.*, vol. 71, no. 9, pp. 4136–4139, 1992.
[77] K. Tsubouchi and N. Mikoshiba, "Zero-temperature-coefficient SAW devices on AlN epitaxial films," *IEEE Trans. Son. Ultrason.*, vol. 32, no. 5, pp. 634–644, 1985.
[78] N. Watanabe, T. Kimoto, and J. Suda, "The temperature dependence of the refractive indices of GaN and AlN from room temperature up to 515 °C," *J. Appl. Phys.*, vol. 104, no. 10, p. 106101, 2008.
[79] S. Yu. Davydov, "Evaluation of physical parameters for the group III nitrates: BN, AlN, GaN, and InN," *Semiconductors*, vol. 36, no. 1, pp. 41–44, 2002.
[80] E. Crisman, A. Drehman, R. Miller, A. Osinsky, D. Volovik, and V. Vasilyev, "Enhanced AlN nanostructures for pyroelectric sensors," *Phys. Status Solidi C*, vol. 11, nos 3-4, pp. 517–520, 2014.
[81] A. Iqbal and F. Mohd-Yasin, "Reactive sputtering of aluminum nitride (002) thin films for piezoelectric applications: A review," *Sensors*, vol. 18, no. 6, 2018, https://doi.org/10.3390/s18061797.
[82] W. H. Pernice, C. Xiong, and H. X. Tang, "High Q micro-ring resonators fabricated from polycrystalline aluminum nitride films for near infrared and visible photonics," *Opt. Express*, vol. 20, no. 11, pp. 12261–12269, 2012.
[83] A. Majkić, U. Puc, A. Franke, et al., "Optical properties of aluminum nitride single crystals in the THz region," *Opt. Mater. Express*, vol. 5, no. 10, pp. 2106–2111, 2015.
[84] X. Liu, A. W. Bruch, Z. Gong, et al., "Ultra-high-Q UV microring resonators based on a single-crystalline AlN platform," *Optica*, vol. 5, no. 10, pp. 1279–1282, 2018.
[85] T. A. Growden, W. Zhang, E. R. Brown, D. F. Storm, D. J. Meyer, and P. R. Berger, "Near-UV electroluminescence in unipolar-doped, bipolar-tunneling GaN/AlN heterostructures," *Light Sci. Appl.*, vol. 7, no. 2, p. 17150, 2018.
[86] C. R. Haughn, G. Rupper, T. Wunderer, et al., "Highly radiative nature of ultra-thin c-plane Al-rich AlGaN/AlN quantum wells for deep ultraviolet emitters," *Appl. Phys. Lett.*, vol. 114, no. 10, p. 102101, 2019.
[87] H. Kobayashi, S. Ichikawa, M. Funato, and Y. Kawakami, "Self-limiting growth of ultrathin GaN/AlN quantum wells for highly

efficient deep ultraviolet emitters," *Adv. Opt. Mater.*, vol. 7, no. 21, p. 1900860, 2019.
[88] Z. Hu, L. Long, R. Wan, et al., "Ultrawide bandgap AlN metasurfaces for ultraviolet focusing and routing," *Opt. Lett.*, vol. 45, no. 13, pp. 3466–3469, 2020.
[89] P. T. Lin, H. Jung, L. C. Kimerling, A. Agarwal, and H. X. Tang, "Low-loss aluminium nitride thin film for mid-infrared microphotonics," *Laser Photonics Rev.*, vol. 8, no. 2, pp. L23–L28, 2014.
[90] B. Dong, X. Luo, S. Zhu, et al., "Thermal annealing study of the mid-infrared aluminum nitride on insulator (AlNOI) photonics platform," *Opt. Express*, vol. 27, no. 14, pp. 19815–19826, 2019.
[91] C. Xiong, W. H. P. Pernice, and H. X. Tang, "Low-loss, silicon integrated, aluminum nitride photonic circuits and their use for electro-optic signal processing," *Nano Lett.*, vol. 12, no. 7, pp. 3562–3568, 2012.
[92] S. Zhu and G.-Q. Lo, "Aluminum nitride electro-optic phase shifter for backend integration on silicon," *Opt. Express*, vol. 24, no. 12, pp. 12501–12506, 2016.
[93] T. Troha, M. Rigler, D. Alden, et al., "UV second harmonic generation in AlN waveguides with modal phase matching," *Opt. Mater. Express*, vol. 6, no. 6, pp. 2014–2023, 2016.
[94] X. Guo, C.-L. Zou, and H. X. Tang, "Second-harmonic generation in aluminum nitride microrings with 2500%/W conversion efficiency," *Optica*, vol. 3, no. 10, pp. 1126–1131, 2016.
[95] J. B. Surya, X. Guo, C.-L. Zou, and H. X. Tang, "Control of second-harmonic generation in doubly resonant aluminum nitride microrings to address a rubidium two-photon clock transition," *Opt. Lett.*, vol. 43, no. 11, pp. 2696–2699, 2018.
[96] A. W. Bruch, X. Liu, X. Guo, et al., "17 000%/W second-harmonic conversion efficiency in single-crystalline aluminum nitride microresonators," *Appl. Phys. Lett.*, vol. 113, no. 13, p. 131102, 2018.
[97] H. Jung, X. Guo, N. Zhu, S. B. Papp, S. A. Diddams, and H. X. Tang, "Phase-dependent interference between frequency doubled comb lines in a $\chi^{(2)}$ phase-matched aluminum nitride microring," *Opt. Lett.*, vol. 41, no. 16, pp. 3747–3750, 2016.
[98] X. Guo, C. Zou, C. Schuck, H. Jung, R. Cheng, and H. X. Tang, "Parametric down-conversion photon-pair source on a nanophotonic chip," *Light Sci. Appl.*, vol. 6, no. 5, p. e16249, 2017.
[99] H. Jung, R. Stoll, X. Guo, D. Fischer, and H. X. Tang, "Green, red, and IR frequency comb line generation from single IR pump in AlN microring resonator," *Optica*, vol. 1, no. 6, pp. 396–399, 2014.
[100] H. Jung, Z. Gong, X. Liu, X. Guo, C. Zou, and H. X. Tang, "Stokes and anti-Stokes Raman scatterings from frequency comb lines in poly-crystalline aluminum nitride microring resonators," *Opt. Express*, vol. 27, no. 16, pp. 22246–22253, 2019.
[101] X. Liu, C. Sun, B. Xiong, et al., "Integrated continuous-wave aluminum nitride Raman laser," *Optica*, vol. 4, no. 8, pp. 893–896, 2017.
[102] A. Sanz-Hervás, M. Clement, E. Iborra, L. Vergara, J. Olivares, and J. Sangrador, "Degradation of the piezoelectric response of sputtered c-axis AlN thin films with traces of non-(0002) x-ray diffraction peaks," *Appl. Phys. Lett.*, vol. 88, no. 16, p. 161915, 2006.
[103] C. Xiong, X. Sun, K. Y. Fong, and H. X. Tang, "Integrated high frequency aluminum nitride optomechanical resonators," *Appl. Phys. Lett.*, vol. 100, no. 17, p. 171111, 2012.
[104] L. Fan, X. Sun, C. Xiong, C. Schuck, and H. X. Tang, "Aluminum nitride piezo-acousto-photonic crystal nanocavity with high quality factors," *Appl. Phys. Lett.*, vol. 102, no. 15, p. 153507, 2013.
[105] C.-L. Zou, X. Han, L. Jiang, and H. X. Tang, "Cavity piezomechanical strong coupling and frequency conversion on an aluminum nitride chip," *Phys. Rev. A*, vol. 94, no. 1, p. 013812, 2016.
[106] S. Ghosh and G. Piazza, "Laterally vibrating resonator based elasto-optic modulation in aluminum nitride," *APL Photonics*, vol. 1, no. 3, p. 036101, 2016.
[107] H. Li, S. A. Tadesse, Q. Liu, and M. Li, "Nanophotonic cavity optomechanics with propagating acoustic waves at frequencies up to 12 GHz," *Optica*, vol. 2, no. 9, pp. 826–831, 2015.
[108] M. Akiyama, K. Kano, and A. Teshigahara, "Influence of growth temperature and scandium concentration on piezoelectric response of scandium aluminum nitride alloy thin films," *Appl. Phys. Lett.*, vol. 95, no. 16, p. 162107, 2009.
[109] Y. Kusano, I. Ishii, T. Kamiya, A. Teshigahara, G. -L. Luo, and D. A. Horsley, "High-SPL air-coupled piezoelectric micromachined ultrasonic transducers based on 36% ScAlN thin-film," *IEEE Trans. Ultrason. Ferroelectrics Freq. Contr.*, vol. 66, no. 9, pp. 1488–1496, 2019.
[110] J. A. Carruthers, T. H. Geballe, H. M. Rosenberg, J. M. Ziman, and K. A. G. Mendelssohn, "The thermal conductivity of germanium and silicon between 2 an d 300° K," *Proc. Roy. Soc. Lond. Math. Phys. Sci.*, vol. 238, no. 1215, pp. 502–514, 1957.
[111] S. P. Gaur, K. Rangra, and D. Kumar, "MEMS AlN pyroelectric infrared sensor with medium to long wave IR absorber," *Sensor Actuator Phys.*, vol. 300, p. 111660, 2019.
[112] D. K. T. Ng, G. Wu, T.-T. Zhang, et al., "Considerations for an 8-inch wafer-level CMOS compatible AlN pyroelectric 5–14 μm wavelength IR detector towards miniature integrated photonics gas sensors," *J Microelectromech. Syst.*, vol. 29, no. 5, pp. 1199–1207, 2020.
[113] M.-A. Dubois and P. Muralt, "Properties of aluminum nitride thin films for piezoelectric transducers and microwave filter applications," *Appl. Phys. Lett.*, vol. 74, no. 20, pp. 3032–3034, 1999.
[114] Y. Taniyasu, M. Kasu, and T. Makimoto, "An aluminium nitride light-emitting diode with a wavelength of 210 nanometres," *Nature*, vol. 441, no. 7091, pp. 325–328, 2006.
[115] T.-J. Lu, M. Fanto, H. Choi, et al., "Aluminum nitride integrated photonics platform for the ultraviolet to visible spectrum," *Opt. Express*, vol. 26, no. 9, pp. 11147–11160, 2018.
[116] D. Sam-Giao, D. Néel, S. Sergent, et al., "High quality factor AlN nanocavities embedded in a photonic crystal waveguide," *Appl. Phys. Lett.*, vol. 100, no. 19, p. 191104, 2012.
[117] S. Sergent, M. Arita, S. Kako, K. Tanabe, S. Iwamoto, and Y. Arakawa, "High-Q AlN photonic crystal nanobeam cavities fabricated by layer transfer," *Appl. Phys. Lett.*, vol. 101, no. 10, p. 101106, 2012.
[118] S. Zhao, A. T. Connie, M. H. T. Dastjerdi, et al., "Aluminum nitride nanowire light emitting diodes: breaking the fundamental bottleneck of deep ultraviolet light sources," *Sci. Rep.*, vol. 5, no. 1, p. 8332, 2015.
[119] W. Zheng, F. Huang, R. Zheng, and H. Wu, "Low-dimensional structure vacuum-ultraviolet-sensitive (λ < 200 nm) photodetector with fast-response speed based on high-quality

AlN micro/nanowire," *Adv. Mater.*, vol. 27, no. 26, pp. 3921–3927, 2015.
[120] M. Spies, M. I. den Hertog, P. Hille, et al., "Bias-controlled spectral response in GaN/AlN single-nanowire ultraviolet photodetectors," *Nano Lett.*, vol. 17, no. 7, pp. 4231–4239, 2017.
[121] D. You, C. Xu, J. Zhao, et al., "Single-crystal ZnO/AlN core/shell nanowires for ultraviolet emission and dual-color ultraviolet photodetection," *Adv. Opt. Mater.*, vol. 7, no. 6, p. 1801522, 2019.
[122] S. Kaushik, T. R. Naik, A. Alka, et al., "Surface modification of AlN using organic molecular layer for improved deep UV photodetector performance," *ACS Appl. Electron. Mater.*, vol. 2, no. 3, pp. 739–746, 2020.
[123] J. Lu, X. Liu, A. W. Bruch, et al., "Ultraviolet to mid-infrared supercontinuum generation in single-crystalline aluminum nitride waveguides," *Opt. Lett.*, vol. 45, no. 16, pp. 4499–4502, 2020.
[124] M. Zhao, W. Kusolthossakul, and K. Fang, "High-efficiency fiber-to-chip interface for aluminum nitride quantum photonics," *OSA Continuum*, vol. 3, no. 4, pp. 952–960, 2020.
[125] A. Soltani, A. Stolz, J. Charrier, et al., "Dispersion properties and low infrared optical losses in epitaxial AlN on sapphire substrate in the visible and infrared range," *J. Appl. Phys.*, vol. 115, no. 16, p. 163515, 2014.
[126] Y. Xue, H. Wang, N. Xie, et al., "Single-photon emission from point defects in aluminum nitride films," *J. Phys. Chem. Lett.*, vol. 11, no. 7, pp. 2689–2694, 2020.
[127] T.-J. Lu, B. Lienhard, K.-Y. Jeong, et al., "Bright high-purity quantum emitters in aluminum nitride integrated photonics," *ACS Photonics*, vol. 7, no. 10, pp. 2650–2657, 2020.
[128] X. Guo, C.-L. Zou, H. Jung, and H. X. Tang, "On-chip strong coupling and efficient frequency conversion between telecom and visible optical modes," *Phys. Rev. Lett.*, vol. 117, no. 12, p. 123902, 2016.
[129] A. W. Bruch, X. Liu, J. B. Surya, C.-L. Zou, and H. X. Tang, "On-chip $\chi^{(2)}$ microring optical parametric oscillator," *Optica*, vol. 6, no. 10, p. 1361–1366, 2019.
[130] A. W. Bruch, X. Liu, Z. Gong, et al., "Pockels soliton microcomb," *Nat. Photonics*, vol. 15, pp. 21–27, 2021.
[131] J. B. Surya, X. Guo, C.-L. Zou, and H. X. Tang, "Efficient third-harmonic generation in composite aluminum nitride/silicon nitride microrings," *Optica*, vol. 5, no. 2, pp. 103–108, 2018.
[132] X. Liu, C. Sun, B. Xiong, et al., "Generation of multiple near-visible comb lines in an AlN microring via $\chi^{(2)}$ and $\chi^{(3)}$ optical nonlinearities," *Appl. Phys. Lett.*, vol. 113, no. 17, p. 171106, 2018.
[133] D. D. Hickstein, H. Jung, D. R. Carlson, et al., "Ultrabroadband supercontinuum generation and frequency-comb stabilization using on-chip waveguides with both cubic and quadratic nonlinearities," *Phys. Rev. Appl.*, vol. 8, no. 1, p. 014025, 2017.
[134] H. Chen, J. Zhou, D. Li, et al., "On-chip directional octave-spanning supercontinuum generation from high order mode in near ultraviolet to infrared spectrum using AlN waveguides," arXiv preprint arXiv:1908.04719 (2019).
[135] S. Ghosh, C. R. Doerr, and G. Piazza, "Aluminum nitride grating couplers," *Appl. Opt.*, vol. 51, no. 17, pp. 3763–3767, 2012.
[136] T. Jin, H.-Y. G. Lin, and P. T. Lin, "Monolithically integrated Si-on-AlN mid-infrared photonic chips for real-time and label-free chemical sensing," *ACS Appl. Mater. Interfaces*, vol. 9, no. 49, pp. 42905–42911, 2017.
[137] X. Liu, C. Sun, B. Xiong, et al., "Aluminum nitride-on-sapphire platform for integrated high-Q microresonators," *Opt. Express*, vol. 25, no. 2, pp. 587–594, 2017.
[138] X. Liu, C. Sun, B. Xiong, et al., "Broadband tunable microwave photonic phase shifter with low RF power variation in a high-Q AlN microring," *Opt. Lett.*, vol. 41, no. 15, pp. 3599–3602, 2016.
[139] W. H. P. Pernice, C. Xiong, C. Schuck, and H. X. Tang, "High-Q aluminum nitride photonic crystal nanobeam cavities," *Appl. Phys. Lett.*, vol. 100, no. 9, p. 091105, 2012.
[140] B. Dong, X. Luo, S. Zhu, et al., "Aluminum nitride on insulator (AlNOI) platform for mid-infrared photonics," *Opt. Lett.*, vol. 44, no. 1, pp. 73–76, 2019.
[141] T. Hu, B. Dong, X. Luo, et al., "Silicon photonic platforms for mid-infrared applications [Invited]," *Photonics Res.*, vol. 5, no. 5, pp. 417–430, 2017.
[142] Y. Shoji, Y. Shirato, and T. Mizumoto, "Silicon Mach–Zehnder interferometer optical isolator having 8 nm bandwidth for over 20 dB isolation," *Jpn. J. Appl. Phys.*, vol. 53, no. 2, p. 022202, 2014.
[143] Y. Zhang, Q. Du, C. Wang, et al., "Monolithic integration of broadband optical isolators for polarization-diverse silicon photonics," *Optica*, vol. 6, no. 4, pp. 473–478, 2019.
[144] A. Mock, D. Sounas, and A. Alù, "Magnet-free circulator based on spatiotemporal modulation of photonic crystal defect cavities," *ACS Photonics*, vol. 6, no. 8, pp. 2056–2066, 2019.
[145] M. Wu, E. Zeuthen, K. C. Balram, and K. Srinivasan, "Microwave-to-Optical transduction using a mechanical supermode for coupling piezoelectric and optomechanical resonators," *Phys. Rev. Appl.*, vol. 13, no. 1, p. 014027, 2020.
[146] A. Pitanti, T. Makkonen, M. F. Colombano, et al., "High-frequency mechanical excitation of a silicon nanostring with piezoelectric aluminum nitride layers," *Phys. Rev. Appl.*, vol. 14, no. 1, p. 014054, 2020.
[147] M. Mirhosseini, A. Sipahigil, M. Kalaee, and O. Painter, "Superconducting qubit to optical photon transduction," *Nature*, vol. 588, no. 7839, pp. 599–603, 2020.
[148] M. Mexis, S. Sergent, T. Guillet, et al., "High quality factor nitride-based optical cavities: microdisks with embedded GaN/Al (Ga) N quantum dots," *Opt. Lett.*, vol. 36, no. 12, pp. 2203–2205, 2011.
[149] J. Lähnemann, A. Ajay, M. I. Den Hertog, and E. Monroy, "Near-infrared intersubband photodetection in GaN/AlN nanowires," *Nano Lett.*, vol. 17, no. 11, pp. 6954–6960, 2017.
[150] S. Kim, N. M. H. Duong, M. Nguyen, et al., "Integrated on chip platform with quantum emitters in layered materials," *Adv. Opt. Mater.*, vol. 7, no. 23, p. 1901132, 2019.
[151] N. H. Wan, T.-J. Lu, K. C. Chen, et al., "Large-scale integration of artificial atoms in hybrid photonic circuits," *Nature*, vol. 583, no. 7815, pp. 226–231, 2020.
[152] N. Kurz, Y. Lu, L. Kirste, et al., "Temperature dependence of the pyroelectric coefficient of AlScN thin films," *Phys. Status Solidi*, vol. 215, no. 13, p. 1700831, 2018.
[153] M. Khorasaninejad, W. T. Chen, R. C. Devlin, J. Oh, A. Y. Zhu, and F. Capasso, "Metalenses at visible wavelengths: diffraction-limited focusing and subwavelength resolution imaging," *Science*, vol. 352, no. 6290, p. 1190, 2016.
[154] W. T. Chen, A. Y. Zhu, V. Sanjeev, et al., "A broadband achromatic metalens for focusing and imaging in the visible," *Nat. Nanotechnol.*, vol. 13, no. 3, pp. 220–226, 2018.

[155] T. Hu, Q. Zhong, N. Li, et al., "CMOS-compatible a-Si metalenses on a 12-inch glass wafer for fingerprint imaging," *Nanophotonics*, vol. 9, no. 4, 2020, https://doi.org/10.1515/nanoph-2019-0470.
[156] C.-S. Park, V. R. Shrestha, W. Yue, et al., "Structural color filters enabled by a dielectric metasurface incorporating hydrogenated amorphous silicon nanodisks," *Sci. Rep.*, vol. 7, no. 1, p. 2556, 2017.
[157] W. Yue, S. Gao, S.-S. Lee, E.-S. Kim, and D.-Y. Choi, "Highly reflective subtractive color filters capitalizing on a silicon metasurface integrated with nanostructured aluminum mirrors," *Laser Photonics Rev.*, vol. 11, no. 3, p. 1600285, 2017.
[158] Z. Xu, N. Li, Y. Dong, et al., "Metasurface-based subtractive color filter fabricated on a 12-inch glass wafer using CMOS platform," *Photonics Res.*, vol. 9, no. 1, pp. 13–20, 2020.
[159] S. Kita, K. Takata, M. Ono, et al., "Coherent control of high efficiency metasurface beam deflectors with a back partial reflector," *APL Photonics*, vol. 2, no. 4, p. 046104, 2017.
[160] N. Li, H. Y. Fu, Y. Dong, et al., "Large-area pixelated metasurface beam deflector on a 12-inch glass wafer for random point generation," *Nanophotonics*, vol. 8, no. 10, p. 1855, 2019.
[161] Y. F. Yu, A. Y. Zhu, R. Paniagua-Domínguez, Y. H. Fu, B. Luk'yanchuk, and A. I. Kuznetsov, "High-transmission dielectric metasurface with 2π phase control at visible wavelengths," *Laser Photonics Rev.*, vol. 9, no. 4, pp. 412–418, 2015.
[162] Z. H. Jiang, L. Lin, D. Ma, et al., "Broadband and wide field-of-view plasmonic metasurface-enabled waveplates," *Sci. Rep.*, vol. 4, p. 7511, 2014.
[163] F. Ding, Z. Wang, S. He, V. M. Shalaev, and A. V. Kildishev, "Broadband high-efficiency half-wave plate: A supercell-based plasmonic metasurface approach," *ACS Nano*, vol. 9, no. 4, pp. 4111–4119, 2015.
[164] Y. Dong, Z. Xu, N. Li, et al., "Si metasurface half-wave plates demonstrated on a 12-inch CMOS platform," *Nanophotonics*, vol. 9, no. 1, pp. 149–157, 2019.
[165] G. Zheng, H. Mühlenbernd, M. Kenney, G. Li, T. Zentgraf, and S. Zhang, "Metasurface holograms reaching 80% efficiency," *Nat. Nanotechnol.*, vol. 10, p. 308, 2015.
[166] X. Ni, A. V. Kildishev, and V. M. Shalaev, "Metasurface holograms for visible light," *Nat. Commun.*, vol. 4, p. 2807, 2013.
[167] L. Huang, S. Zhang, and T. Zentgraf, "Metasurface holography: from fundamentals to applications," *Nanophotonics*, vol. 7, no. 6, pp. 1169–1190, 2018.
[168] N. Li, Z. Xu, Y. Dong, et al., "Large-area metasurface on CMOS-compatible fabrication platform: driving flat optics from lab to fab," *Nanophotonics*, vol. 9, no. 10, pp. 3071–3087, 2020.
[169] Z. Xu, Y. Dong, C.-K. Tseng, et al., "CMOS-compatible all-Si metasurface polarizing bandpass filters on 12-inch wafers," *Opt. Express*, vol. 27, no. 18, pp. 26060–26069, 2019.
[170] Q. Zhong, Y. Dong, D. Li, et al., "Large-area metalens directly patterned on a 12-inch glass wafer using immersion lithography for mass production," in *Optical Fiber Communication Conference (OFC) 2020*, Optical Society of America, 2020. San Diego, CA, USA, OSA Technical Digest, p. Th2A.8.
[171] X. Gao, R. Wan, J. Yan, et al., "Design of AlN ultraviolet metasurface for single-/multi-plane holography," *Appl. Opt.*, vol. 59, no. 14, pp. 4398–4403, 2020.
[172] L. Guo, Z. Hu, R. Wan, et al., "Design of aluminum nitride metalens for broadband ultraviolet incidence routing," *Nanophotonics*, vol. 8, no. 1, pp. 171–180, 2019.
[173] S. Liu, K. Xu, Q. Song, Z. Cheng, and H. K. Tsang, "Design of mid-infrared electro-optic modulators based on aluminum nitride waveguides," *J. Lightwave Technol.*, vol. 34, no. 16, pp. 3837–3842, 2016.
[174] W. P. Lin, P. M. Lundquist, G. K. Wong, E. D. Rippert, and J. B. Ketterson, "Second order optical nonlinearities of radio frequency sputter-deposited AlN thin films," *Appl. Phys. Lett.*, vol. 63, no. 21, pp. 2875–2877, 1993.
[175] P. M. Lundquist, W. P. Lin, Z. Y. Xu, et al., "Ultraviolet second harmonic generation in radio-frequency sputter-deposited aluminum nitride thin films," *Appl. Phys. Lett.*, vol. 65, no. 9, pp. 1085–1087, 1994.
[176] M. C. Larciprete, A. Bosco, A. Belardini, et al., "Blue second harmonic generation from aluminum nitride films deposited onto silicon by sputtering technique," *J. Appl. Phys.*, vol. 100, no. 2, p. 023507, 2006.
[177] Y. Tang, Z. Gong, X. Liu, and H. X. Tang, "Widely separated optical Kerr parametric oscillation in AlN microrings," *Opt. Lett.*, vol. 45, no. 5, pp. 1124–1127, 2020.
[178] H. Jung, C. Xiong, K. Y. Fong, X. Zhang, and H. X. Tang, "Optical frequency comb generation from aluminum nitride microring resonator," *Opt. Lett.*, vol. 38, no. 15, pp. 2810–2813, 2013.
[179] H. Jung, K. Y. Fong, C. Xiong, and H. X. Tang, "Electrical tuning and switching of an optical frequency comb generated in aluminum nitride microring resonators," *Opt. Lett.*, vol. 39, no. 1, pp. 84–87, 2014.
[180] Z. Gong, A. Bruch, M. Shen, et al., "High-fidelity cavity soliton generation in crystalline AlN micro-ring resonators," *Opt. Lett.*, vol. 43, no. 18, pp. 4366–4369, 2018.
[181] Th. Udem, R. Holzwarth, and T. W. Hänsch, "Optical frequency metrology," *Nature*, vol. 416, no. 6877, pp. 233–237, 2002.
[182] A. Schliesser, N. Picqué, and T. W. Hänsch, "Mid-infrared frequency combs," *Nat. Photonics*, vol. 6, no. 7, pp. 440–449, 2012.
[183] Y. Na, C.-G. Jeon, C. Ahn, et al., "Ultrafast, sub-nanometre-precision and multifunctional time-of-flight detection," *Nat. Photonics*, vol. 14, no. 6, pp. 355–360, 2020.
[184] E. Lucas, P. Brochard, R. Bouchand, S. Schilt, T. Südmeyer, and T. J. Kippenberg, "Ultralow-noise photonic microwave synthesis using a soliton microcomb-based transfer oscillator," *Nat. Commun.*, vol. 11, no. 1, p. 374, 2020.
[185] J. Liu, E. Lucas, A. S. Raja, et al., "Photonic microwave generation in the X- and K-band using integrated soliton microcombs," *Nat. Photonics*, vol. 14, no. 8, pp. 486–491, 2020.
[186] J. H. Wong, H. Q. Lam, S. Aditya, et al., "Photonic generation of frequency-tunable microwave signals using an array of uniformly spaced optical combs," *J. Lightwave Technol.*, vol. 30, no. 19, pp. 3164–3172, 2012.
[187] S. A. Diddams, "The evolving optical frequency comb [Invited]," *J. Opt. Soc. Am. B*, vol. 27, no. 11, pp. B51–B62, 2010.
[188] T. Fortier and E. Baumann, "20 years of developments in optical frequency comb technology and applications," *Commun. Phys.*, vol. 2, no. 1, p. 153, 2019.
[189] S. A. Diddams, K. Vahala, and T. Udem, "Optical frequency combs: coherently uniting the electromagnetic spectrum," *Science*, vol. 369, no. 6501, p. eaay3676, 2020.

[190] E. Obrzud, M. Rainer, A. Harutyunyan, et al., "A microphotonic astrocomb," *Nat. Photonics*, vol. 13, no. 1, pp. 31–35, 2019.
[191] M. Kues, C. Reimer, J. M. Lukens, et al., "Quantum optical microcombs," *Nat. Photonics*, vol. 13, no. 3, pp. 170–179, 2019.
[192] T. Herr, K. Hartinger, J. Riemensberger, et al., "Universal formation dynamics and noise of Kerr-frequency combs in microresonators," *Nat. Photonics*, vol. 6, no. 7, pp. 480–487, 2012.
[193] P. Del'Haye, A. Schliesser, O. Arcizet, T. Wilken, R. Holzwarth, and T. J. Kippenberg, "Optical frequency comb generation from a monolithic microresonator," *Nature*, vol. 450, no. 7173, pp. 1214–1217, 2007.
[194] H. Jung, M. Poot, and H. X. Tang, "In-resonator variation of waveguide cross-sections for dispersion control of aluminum nitride micro-rings," *Opt. Express*, vol. 23, no. 24, pp. 30634–30640, 2015.
[195] J. M. Dudley, G. Genty, and S. Coen, "Supercontinuum generation in photonic crystal fiber," *Rev. Mod. Phys.*, vol. 78, no. 4, pp. 1135–1184, 2006.
[196] H. Guo, C. Herkommer, A. Billat, et al., "Mid-infrared frequency comb via coherent dispersive wave generation in silicon nitride nanophotonic waveguides," *Nat. Photonics*, vol. 12, no. 6, pp. 330–335, 2018.
[197] C. Lafforgue, S. Guerber, J. M. Ramirez, et al., "Broadband supercontinuum generation in nitrogen-rich silicon nitride waveguides using a 300 mm industrial platform," *Photonics Res.*, vol. 8, no. 3, pp. 352–358, 2020.
[198] D. Yoon Oh, K. Y. Yang, C. Fredrick, G. Ycas, S. A. Diddams, and K. J. Vahala, "Coherent ultra-violet to near-infrared generation in silica ridge waveguides," *Nat. Commun.*, vol. 8, no. 1, p. 13922, 2017.
[199] M. Jankowski, C. Langrock, B. Desiatov, et al., "Ultrabroadband nonlinear optics in nanophotonic periodically poled lithium niobate waveguides," *Optica*, vol. 7, no. 1, pp. 40–46, 2020.
[200] X. Xiong, C.-L. Zou, X. Guo, H. X. Tang, X.-F. Ren, and G.-C. Guo, "Broadband frequency conversion and "area law" in tapered waveguides," *OSA Continuum*, vol. 1, no. 4, pp. 1349–1359, 2018.
[201] Q. Wang, Y. Lu, S. Mishin, Y. Oshmyansky, and D. A. Horsley, "Design, fabrication, and characterization of scandium aluminum nitride-based piezoelectric micromachined ultrasonic transducers," *J Microelectromech. Syst.*, vol. 26, no. 5, pp. 1132–1139, 2017.
[202] M. Ghatge, V. Felmetsger, and R. Tabrizian, "High kt^{2Q} waveguide-based ScAlN-on-Si UHF and SHF resonators," in *2018 IEEE International Frequency Control Symposium (IFCS)*, Olympic Valley, CA, USA, IEEE, 2018, pp. 1–4.
[203] M. Schneider, M. DeMiguel-Ramos, A. J. Flewitt, E. Iborra, and U. Schmid, "Scandium aluminium nitride-based film bulk acoustic resonators," *Proceedings*, vol. 1, no. 4, 2017.
[204] Y. Zhu, N. Wang, G. Chua, C. Sun, N. Singh, and Y. Gu, "ScAlN-based LCAT mode resonators above 2 GHz with high FOM and reduced fabrication complexity," *IEEE Electron. Device Lett.*, vol. 38, no. 10, pp. 1481–1484, 2017.
[205] N. Wang, Y. Zhu, B. Chen, and Y. Zhang, "Over 12% of coupling coefficient demonstrated by 3GHz Sc0.12Al0.88N based laterally coupled alternating thickness (LCAT) mode resonators," in *2019 IEEE International Ultrasonics Symposium (IUS)*, Glasgow, UK, IEEE, 2019, pp. 1971–1973.
[206] S. Zhu, Q. Zhong, N. Li, et al., "Integrated ScAlN photonic circuits on silicon substrate," in *Conference on Lasers and Electro-Optics*, Optical Society of America, 2020. OSA Technical Digest, p. STu3P.5.
[207] X. Wu, J. Feng, X. Liu, and H. Zeng, "Effects of rapid thermal annealing on aluminum nitride waveguides," *Opt. Mater. Express*, vol. 10, no. 12, pp. 3073–3080, 2020.
[208] J. Wang, M. Park, S. Mertin, T. Pensala, F. Ayazi, and A. Ansari, "A film bulk acoustic resonator based on ferroelectric aluminum scandium nitride films," *J Microelectromech. Syst.*, vol. 29, no. 5, pp. 741–747, 2020.
[209] J. Wang, M. Park, S. Mertin, T. Pensala, F. Ayazi, and A. Ansari, "A high-kt^2 switchable ferroelectric Al0.7Sc0.3N film bulk acoustic resonator," in *2020 Joint Conference of the IEEE International Frequency Control Symposium and International Symposium on Applications of Ferroelectrics (IFCS-ISAF)*, Keystone, CO, USA, IEEE, 2020, pp. 1–3.
[210] P. Stark, J. G. Kremer, F. Eltes, et al., "Non-volatile photonic weights and their impact on photonic reservoir computing systems," in *2019 Conference on Lasers and Electro-Optics Europe & European Quantum Electronics Conference (CLEO/Europe-EQEC)*, Munich. Germany, IEEE, 2019, p. 11.
[211] A. E. Giba, *Rare Earth-doped Aluminum Nitride Thin Films for Optical Applications*, Université de Lorraine; Universität des Saarlandes, 2018.
[212] N. Li, D. Vermeulen, Z. Su, et al., "Monolithically integrated erbium-doped tunable laser on a CMOS-compatible silicon photonics platform," *Opt. Express*, vol. 26, no. 13, pp. 16200–16211, 2018.
[213] Purnawirman, N. Li, E. S. Magden, et al., "Ultra-narrow-linewidth Al2O3:Er3+ lasers with a wavelength-insensitive waveguide design on a wafer-scale silicon nitride platform," *Opt. Express*, vol. 25, no. 12, pp. 13705–13713, 2017.
[214] E. H. Bernhardi, H. A. G. M. van Wolferen, L. Agazzi, et al., "Ultra-narrow-linewidth, single-frequency distributed feedback waveguide laser in Al2O3:Er3+ on silicon," *Opt. Lett.*, vol. 35, no. 14, pp. 2394–2396, 2010.
[215] F. X. Kärtner, P. T. Callahan, K. Shtyrkova, et al., "Integrated rare-Earth doped mode-locked lasers on a CMOS platform," in *Proc. SPIE 10686, Silicon Photonics: From Fundamental Research to Manufacturing, 106860F*, Strasbourg, France, SPIE, 2018.
[216] Purnawirman, N. Li, G. Singh, et al., "Reliable integrated photonic light sources using curved Al2O3:Er3+ distributed feedback lasers," *IEEE Photonics J.*, vol. 9, no. 4, pp. 1–9, 2017.
[217] N. Li, Z. Su, Purnawirman, et al., "Athermal synchronization of laser source with WDM filter in a silicon photonics platform," *Appl. Phys. Lett.*, vol. 110, no. 21, p. 211105, 2017.
[218] E. S. Magden, N. Li, Purnawirman, et al., "Monolithically-integrated distributed feedback laser compatible with CMOS processing," *Opt. Express*, vol. 25, no. 15, pp. 18058–18065, 2017.
[219] Z. Su, J. D. B. Bradley, N. Li, et al., "Ultra-compact CMOS-compatible Ytterbium microlaser," in *Advanced Photonics 2016 (IPR, NOMA, Sensors, Networks, SPPCom, SOF)*, Vancouver, Canada, Optical Society of America, 2016, p. IW1A.3. OSA Technical Digest (Online).
[220] E. H. Bernhardi, K. Wörhoff, R. M. de Ridder, and M. Pollnau, "Highly efficient distributed feedback waveguide laser in Al2O3:Yb3+ on silicon," in *Advances in Optical Materials*, Istanbul, Turkey, Optical Society of America, 2011, p. ATuD7. OSA Technical Digest (CD).

[221] G. Singh, Purnawirman, J. D. B. Bradley, et al., "Resonant pumped erbium-doped waveguide lasers using distributed Bragg reflector cavities," *Opt. Lett.*, vol. 41, no. 6, pp. 1189–1192, 2016.
[222] L. Agazzi, J. D. B. Bradley, M. Dijkstra, et al., "Monolithic integration of erbium-doped amplifiers with silicon-on-insulator waveguides," *Opt. Express*, vol. 18, no. 26, pp. 27703–27711, 2010.
[223] M. Belt and D. J. Blumenthal, "Erbium-doped waveguide DBR and DFB laser arrays integrated within an ultra-low-loss Si3N4 platform," *Opt. Express*, vol. 22, no. 9, pp. 10655–10660, 2014.
[224] N. Li, P. Purnawirman, Z. Su, et al., "High-power thulium lasers on a silicon photonics platform," *Opt. Lett.*, vol. 42, no. 6, pp. 1181–1184, 2017.
[225] J. D. Bradley, Z. Su, E. S. Magden, et al., "1.8-μm thulium microlasers integrated on silicon," in *Optical Components and Materials XIII*, vol. 9744, San Francisco, CA, USA, International Society for Optics and Photonics, 2016, p. 97440U.
[226] N. Li, E. S. Magden, Z. Su, et al., "Broadband 2-μm emission on silicon chips: monolithically integrated Holmium lasers," *Opt. Express*, vol. 26, no. 3, pp. 2220–2230, 2018.
[227] D. J. Blumenthal, "Photonic integration for UV to IR applications," *APL Photonics*, vol. 5, no. 2, p. 020903, 2020.
[228] T. Kita, Y. Ishizu, K. Tsuji, et al., "Thermal annealing effects on ultra-violet luminescence properties of Gd doped AlN," *J. Appl. Phys.*, vol. 117, no. 16, p. 163105, 2015.
[229] T.-C. Liu, H. Kominami, H. F. Greer, W. Zhou, Y. Nakanishi, and R.-S. Liu, "Blue emission by interstitial site occupation of Ce3+ in AlN," *Chem. Mater.*, vol. 24, no. 17, pp. 3486–3492, 2012.
[230] W. Wang, P. Zhang, X. Wang, X. Lei, H. Ding, and H. Yang, "Bifunctional AlN:Tb semiconductor with luminescence and photocatalytic properties," *RSC Adv.*, vol. 5, no. 110, pp. 90698–90704, 2015.
[231] R. Weingärtner, O. Erlenbach, A. Winnacker, et al., "Thermal activation, cathodo- and photoluminescence measurements of rare earth doped (Tm,Tb,Dy,Eu,Sm,Yb) amorphous/nanocrystalline AlN thin films prepared by reactive rf-sputtering," *Opt. Mater.*, vol. 28, no. 6, pp. 790–793, 2006.
[232] M. Fanto, T. Lu, H. Choi, et al., "Wide-bandgap integrated photonic circuits for nonlinear interactions and interfacing with quantum memories," in *2018 IEEE Photonics Society Summer Topical Meeting Series (SUM)*, Waikoloa, HI, USA, IEEE, 2018, pp. 257–258.
[233] A. D. O'Connell, M. Hofheinz, M. Ansmann, et al., "Quantum ground state and single-phonon control of a mechanical resonator," *Nature*, vol. 464, no. 7289, pp. 697–703, 2010.
[234] X. Han, W. Fu, C. Zhong, et al., "Cavity piezo-mechanics for superconducting-nanophotonic quantum interface," *Nat. Commun.*, vol. 11, no. 1, p. 3237, 2020.
[235] S. Maity, L. Shao, S. Bogdanović, et al., "Coherent acoustic control of a single silicon vacancy spin in diamond," *Nat. Commun.*, vol. 11, no. 1, p. 193, 2020.